Geosciences and engineering : a publication of the University of Miskolc

2. évf. 4. sz. / 2013

Horváth Attila - Kristály Ferenc - Less György Xenoliths and enclaves from the Miocene volcanic rocks of Tokaj Mts.	7-26
Szabó Norbert Péter - Kalmár Csilla Nonlinear regression model for permeability estimation based on acoustic well-logging measurements	27-46
Somogyiné Molnár Judit - Kiss Anett Modelling the pressure dependence of P wave velocity and porosity on sandstones	47-58
Kóródi Tibor - Molnár Judit Comparative study of a suburban and a rural town’s quality of life	59-65
Vágó János - Hegedűs András - Dobos Endre Analysis of drought conditions in the Carpathians using standardized precipitation index (SPI) 1951–2050	66-80
Pethő Gábor Differential equations and comparison of FEM TE and TM mode with conductivity anisotropy	81-92
Vásárhelyi Balázs - Kovács László - Kovács Boglárka Determining the failure envelope of the intact granitic rocks from Bátaapáti	93-101
Szegedi Hajnalka Generating Hilbert-transform with the use of inversion-based robust Fourier-transform	102-115

Geosciences and Engineering, Vol. 2, No. 4 (2013), pp 7–26.

XENOLITHS AND ENCLAVES FROM THE MIOCENE VOLCANIC ROCKS OF TOKAJ MTS.

ATTILA HORVÁTH–FERENC KRISTÁLY–GYÖRGY LESS

University of Miskolc, Institute of Mineralogy and Geology,
H-3515 Miskolc-Egyetemváros
attila0514@gmail.com; askkf@uni-miskolc.hu; foldlgy@uni-miskolc.hu

1. Abstract

Little information is available about the petrology and mineralogy of pre-Tertiary basement of the Tokaj Mts. In the NE area of the mountains the basement is in uplifted position and data from boreholes are also available. But in the western part of the mountains no boreholes have reached the footwall of the Neogene volcanic succession. The aim of this study is to get more detailed information about the basement. Earlier publications about drill cores and xenoliths were reviewed, and new xenoliths collected by the authors were investigated by petrologic-mineralogic methods.

Xenoliths provide a useful tool to evaluate the composition and nature of the basement in less accessible areas. Based on the xenoliths occurring on the surface or in drill cores, the Tokaj Mts. can be divided into several segments. Limestone xenoliths appear in the East (around Sárospatak), while at the other locations of the Eastern part metamorphic and molasse type xenoliths can be found. The Western area of the mountains is underlain by Szendrő type (Bükkium) rocks based on slate xenoliths. Metamorphic, mainly gneiss xenoliths suggest Veporic type basement in the Northeastern part.

We found that enclaves formerly described as biotite gneiss are in fact opaque mineral and biotite containing enclaves. Opaque minerals are probably the high-temperature alteration products of pelitic rocks ripped up by the ascending magma. Further typical high-temperature mineral assemblages occur in other xenoliths such as sanidine in metaclaystone transformed from a clayey (illite) protolith and cordierite+labradorite+hercynite+corundum in cordierite hornfels.

Keywords:
xenolith, enclave, Bükkium, Veporicum, Zemplinicum, hercynite, symplectite, cordierite hornfels, sanidinite

2. Geological outline of the Tokaj Mountains

The Tokaj Mts. in NW Hungary is the Hungarian part of Eperjes (Prešov)-Tokaj Mts. It is bordered by the Hernád Fault from W, by the Szamos Fault from E and by the Bodrog Fault from S. Other important structural line is the fracture system parallel to the Radvány Stream, along which large-scale subsidence occurred similarly to the faults bordering the mountains. These and other larger faults played a crucial role by determining the place of effusive centres, linear volcanic and postvolcanic activity (GYARMATI 1977).

The igneous rocks of the Tokaj Mts. fill a NE-SW striking volcano-tectonic graben. Orographically the mountains can be divided into the area of the central volcanic range, the Vilyvitány Block and the Szerencs Hills (GYARMATI 1977).

Large-scale tectonic movements took place along the Mid-Hungarian Line in the Miocene that caused local transtensional environment at this area. This extension opened the pull-apart basin which contains the Miocene igneous rocks (HORVÁTH 1993). The magmatic rocks formed during two volcanic cycles. Eight effusive centres and two large

linear volcanic zones can be identified in the region (GYARMATI 1977). Sedimentary formations in the Tokaj Mts. are rare and sporadic, mainly of marine origin. In the Badenian mostly rhyodacite tuff and dacite formed cropping out on the NE part of the mountains. After a short pause a rhyolite, rhyodacite, dacite, pyroxene andesite sequence formed in the Sarmatian (GYARMATI 1977).

Igneous rocks exhibit calc-alkaline character and contain relatively high amounts of SiO_2, Fe and Al (GYARMATI 1977). Accordingly, the geochemical character of the volcanism of Tokaj Mts. represents a transition between island arc and active continental margin (SZABÓ et al. 1992).

3. The basement of the Tokaj Mountains

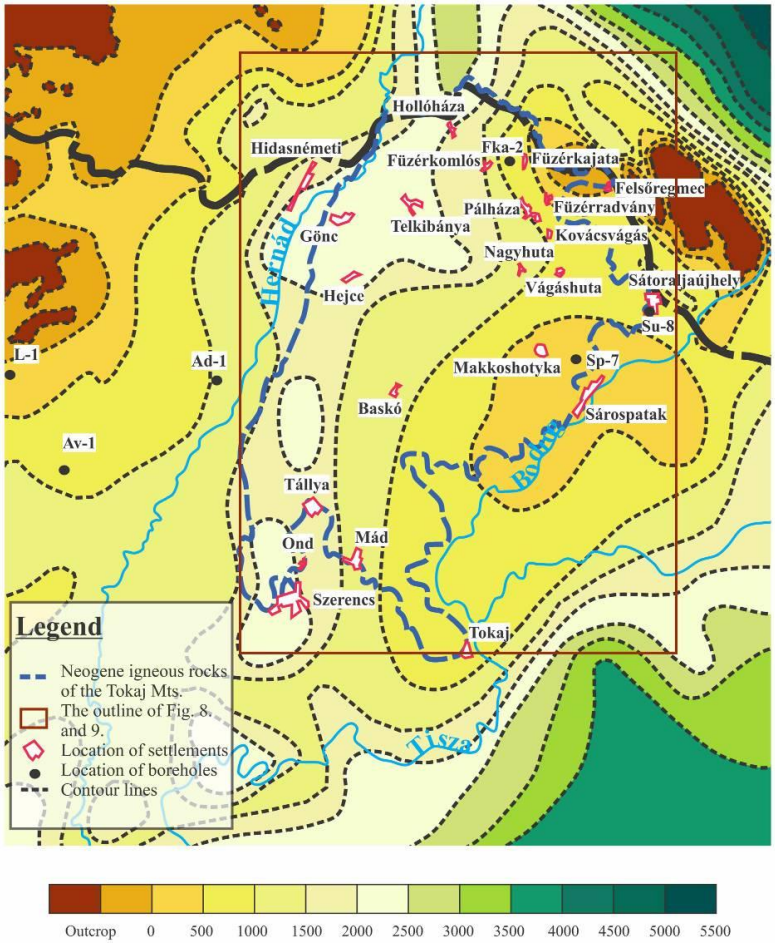

Figure 1. Depth of the basement units (in m; 0 m = sea level) in the area of the Tokaj Mountains. Modified after ZALAI (1991). Abbreviations: Ad-1: Abaújdevecser-1., Av-1: Alsóvadász-1., Fka-2: Füzérkajata-2., L-1: Lak-1., Sp-7: Sárospatak-7., Su-8: Sátoraljaújhely-8.

Neogene igneous rocks fill a 15–20 km wide, 100 km long tectonic graben. The depth of the graben may reach 1.5–2 km at the Western side of the mountains (Fig. 1). Here, no drillhole has reached the basement, which becomes shallower moving eastward until it crops out at the Vilyvitány Block

In the area bordered by Pálháza, Nagyhuta, Makkoshotyka, Sárospatak and Sátoraljaújhely (Fig. 1) the basement is in an uplifted position (less than 1000 m depth) which is indicated by the gravity maximum (ZALAI 1991) and also by the abundance of xenoliths here.

3.1. Zemplinicum. Most information from the basement comes from Zemplinicum, because it is in uplifted position and it crops out at the NE part of the mountains and in a large area in Slovakia, too (Fig.1) (Zemplin Mts. s.s.). The Zemplinicum is part of the Central Western Carpathians along with Tatricum, Veporicum and Hronicum; and thought to be the continuation of the Veporicum (VOZÁR et al. 2010, VOZÁROVÁ & VOZÁR 1988).

The Zemplinicum consists of two main parts: the Proterozoic and Early Palaeozoic metamorphic complex and the unconformably overlying Carboniferous, Permian and Mesozoic succession. Part of these sequences crops out at Vilyvitány, which is often called the Vilyvitány Block (BÓCZÁN et al. 1966, PENTELÉNYI 1972a).

The metamorphic part is dominantly made up by orto- and paragneisses and mica schists. The unmetamorphosed molasse-type Carboniferous and Permian sediments (continental sandstone, conglomerate and shale) are the erosion products of former surface formations and are present in boreholes Felsőregmec-1., Füzérkajata-2., Sátoraljaújhely-8. Siliciclastic sedimentation continued in the Early Triassic, too. Middle Triassic carbonate rocks (Lúžňa Fm, Ladmovce Fm) from Hungary are only known from borehole Sátoraljaújhely-8 (PENTELÉNYI et al. 2003).

3.2. Bükkium. The Bükkium (Szendrő Unit) consists of Palaeozoic (Silurian to Carboniferous) black shale, platform carbonate to pelagic limestone and shale sequences. These rocks were epimetamorphosed during Alpine orogenesis. They occur in several drillholes outside of the Tokaj Mts. (Alsóvadász-1., Felsőgagy-1., Lak-1., Hidasnémeti-1. and Abaújdevecser-1. – Fig. 1), but from the area of the mountains only slate xenoliths are known (Fig. 8–9.).

3.3. Veporicum. Veporicum is made up by various rock types. Metamorphic rocks (mica schists, gneisses) form the basal parts of the succession. At the upper sections various Mesosoic shallow and deep water sediments and terrigeneous rocks dominate, which do not occur in the basement of the mountains. According to PENTELÉNYI (1972a), boreholes Füzérkajata-2. and Felsőregmec-1. expose Veporic-type metavolcanic rocks and phyllites (greenschist facies) beside Zemplinicum-type succession.

3.4. Silicicum. In the area of Sárospatak boreholes Sárospatak-5., Sárospatak-7., Végardó-2., Végardó-4. and Karos-2. expose Upper Triassic Wetterstein- and Dachstein-type limestones which do not show genetic relation with any of the former units (PENTELÉNYI et al. 2003). Xenoliths from these formations occur at Megyer Hill, Sárospatak, in the area of Rudabányácska and in borehole Rudabányácska-1. This limestone sequence is assumed to represent Silicicum-type (s.l.) basement (Fig. 8–9.)

4. Enclaves – previous studies

Enclaves are divided into two main groups: the 'cognate enclaves' and the 'xenoliths'. The term 'cognate enclave' is used for enclaves which have the same parental magma as their host rock (SOLLAS 1894). On the other hand, xenoliths do not show any genetic relation with the host rock.

Former researchers (BÓCZÁN et al. 1966, GYARMATI 1977, GYARMATI & ZELENKA 1968, PENTELÉNYI 1968, 1972a, b) mentioned numerous enclaves and xenoliths but no special research was focussed on them.

Cognate enclaves occur in dacites and andesites in the whole area of the mountains. They are mainly holocrystalline. Their colour is lighter than the host rock because of the high plagioclase content. The main constituents are plagioclase, pyroxene and volcanic glass (GYARMATI 1977), magnetite and apatite are accessorial. Three cognate enclave types are separated. Volcanic glass is present between phenocrysts in the glomeroporphyric cognate enclaves, crystals reaching into the host rock. The microdiorite and porphyric texture cognate enclave subtypes are entirely holocrystalline. Plagioclase phenocrysts are not zoned and form columnar crystals in contrast to the plagioclase of the host rock. Based on microprobe analyses, the chemical composition of the plagioclase crystals is the same in the enclaves and in the host rock.

The xenoliths of Miocene age are sediments formed during the volcanic cycles in bays of the Pannonian Sea or in subaerial environment: claystone, siltstone, sandstone, marl, tuffite or earlier Miocene igneous rocks.

Pre-Tertiary xenoliths show various types of lithology at the different parts of the mountains. Most xenoliths can be found in the area bordered by Pálháza, Nagyhuta, Makkoshotyka and Sárospatak, which coincides with the surface extension of Badenian igneous rocks. Here, the basement is close to the surface (Fig. 1). Gneiss (biotite, cordierite or muscovite gneiss subtypes), sandstone, slate, siltstone, limestone, mica schist and quartzite schist were described from this area (GYARMATI 1977 112, PENTELÉNYI 1972b). Most frequently biotite gneiss is mentioned (BÓCZÁN et al. 1966, GYARMATI 1977, GYARMATI & ZELENKA 1968, PENTELÉNYI 1968, 1972a, b).

Sandstone, slate and quartzite xenoliths occur in the area of Füzérkomlós (Fig. 8). PENTELÉNYI (1972a) found slate and quartzite xenoliths at Kánya Hill, Telkibánya. GYARMATI (1977) reported slate xenoliths from the Baskó-3 drillhole. Limestone fragments are abundant on Megyer Hill, Sárospatak. Amphibolite xenolith occurs on Mandulás Hill, Sárospatak. In the area of Szerencs sandstone, granite and quartzite schist lithotypes were observed by GYARMATI & ZELENKA (1968). The rhyolite tuff at Meredek Hill, Abaújszántó hosts sericitic dark grey slate xenoliths (PENTELÉNYI 1968). Sandstone, slate and quartzite xenoliths are frequent in the area of Bodrogkeresztúr and Tokaj (PENTELÉNYI 1972a).

5. Enclaves investigated in the present study

5.1. Classification of enclaves. We divided enclaves into four groups: (i) the cognate enclaves, (ii) the opaque mineral and biotite bearing xenoliths, (iii) the Miocene xenoliths and (iv) the xenoliths from the Tokaj Mts. basement. Cognate enclaves consist of early crystallized minerals in the magma chamber. Opaque mineral and biotite bearing xenoliths have parts that may have crystallized from the magma and parts of supposed extraneous origin. We separated further two groups of xenoliths: the Miocene sediments and the

Pre-Tertiary basement xenoliths. The latter group comprises of metamorphic and carbonate or clastic sedimentary rocks.

In the spring of 2013 numerous enclaves and xenoliths (~100 pieces) were collected during several field trips which covered the whole area of the mountains. More than half of the collected samples were found to be cognate enclaves; xenoliths are most abundant in felsic tuffs.

The enclaves of the (i) group were found exclusively in andesite and dacite (Fig. 2 A–B). Their border with the host rock is sharp, alteration traces (except for surface alteration) or reaction coronas were not observed. We classified a diorite enclave also as cognate from Hársas Hill, Gönc, although there are uncertainties regarding its origin (Fig. 2 B).

The enclaves of (ii) group consist of plagioclase and significant amount of biotite and opaque minerals. These enclaves contain dark patches. They resemble intact or partly melted biotite gneiss examined by the naked eye (Fig. 2 C–D).

The (iii) group is composed mainly of Miocene xenoliths which are generally unconsolidated sediments thermally altered by the hot magma. We found mostly light-coloured clay fragments as in the white rhyolite tuff at Fehér-kő, Füzérkomlós (Fig. 2 E). As an exception a completely altered andesite xenolith was found in zeolitized rhyolite tuff near Rátka.

Most of the (iv) group xenoliths were found where Badenian rocks are cropping out (NE part, Fig. 8). Mica schist, siltstone and sandstone were identified at Felsőregmec, next to the Vilyvitány Block. Here, light grey coloured, garnet-bearing (Fig. 2 F) and grey more coarse-grained mica schist (Fig. 3 A) subtypes can be separated. Siltstone xenoliths are hard and grey-coloured. Siltstone, mica schist and siliceous xenoliths occur close to Vágáshuta (NE part of the mountains). The xenolith shown on Fig. 3 C is very hard, homogeneous and has conchoidal fracture resembling a siliceous rock by the naked eye. The mica schist xenolith reaching 5 centimetres from Cseresznyés, Vágáshuta is green-coloured and shows good schistosity (Fig. 3 B). A small xenolith of granitic composition was found at the same place. These data are mainly well in agreement with the former findings (GYARMATI 1977: 112, PENTELÉNYI 1972b). At Megyer Hill, Sárospatak numerous grey siltstone xenoliths occur (Fig. 3 D) but we have not observed limestone xenoliths. At the NW part of the mountains, on the Hársas Hill near Gönc – not mentioned by former researchers – gneiss xenoliths are abundant (SZAKÁLL, oral communication, 2013, Fig. 3 E). Their fabric is oriented; they can reach 5 centimetres. We found organic matter bearing dark grey slate xenoliths on Fekete and Kassa Hills near Ond (Fig. 3 F–G). This is in accordance with former observations from the environment of Mád, Baskó, Abaújszántó (GYARMATI & ZELENKA 1968).

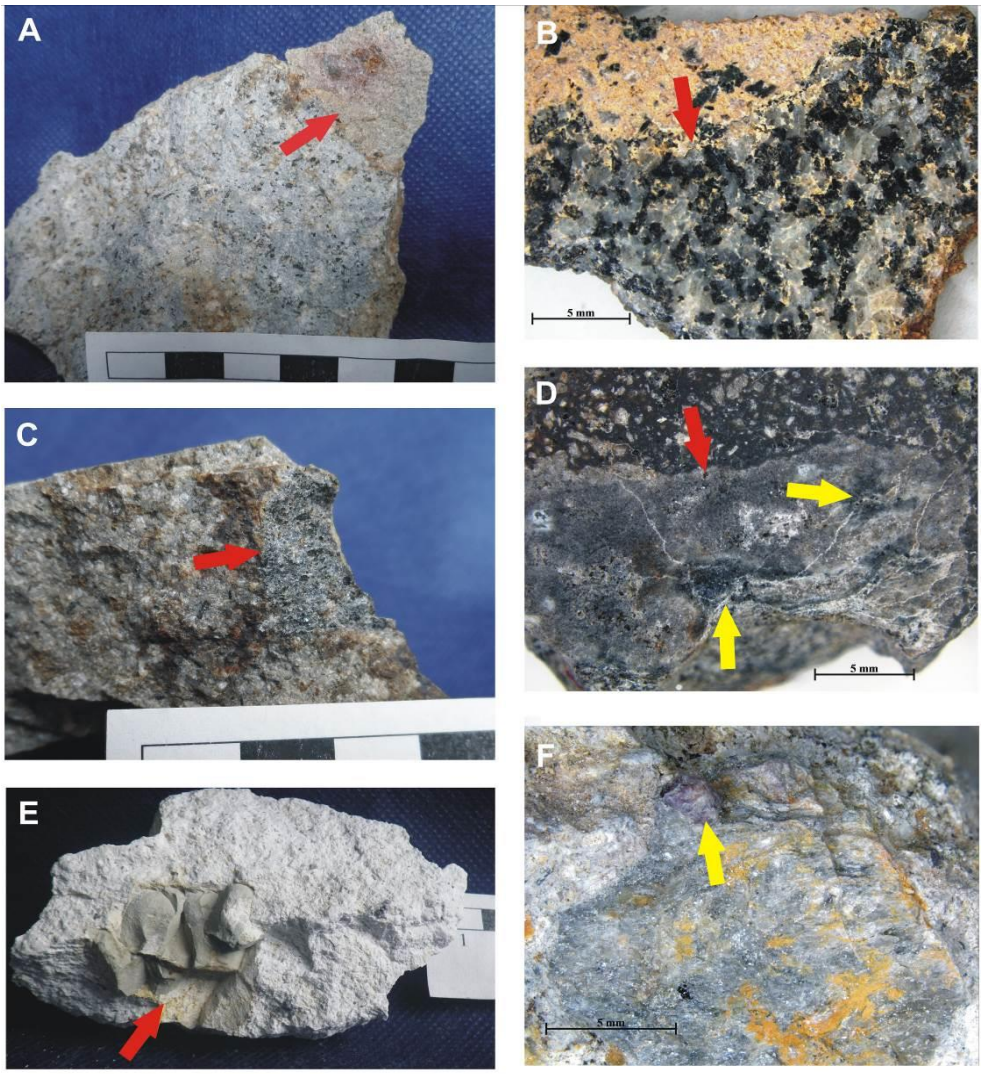

Figure 2. A) Cognate enclave from Fekete Hill, Vágáshuta, microdiorite subtype. B) Diorite (cognate?) from Hársas Hill, Gönc. Polished surface. C) Opaque mineral and biotite bearing xenolith from Cseresznyés, Vágáshuta. D) Opaque mineral and biotite bearing xenolith from Bohár-tető, Kovácsvágás. Polished surface. Yellow arrows point to opaque mineral aggregates. E) Miocene clay xenolith from Füzérkomlós. F) Mica schist xenolith from Felsőregmec. Yellow arrow indicates garnet. Notes: Red arrows point to the enclaves.

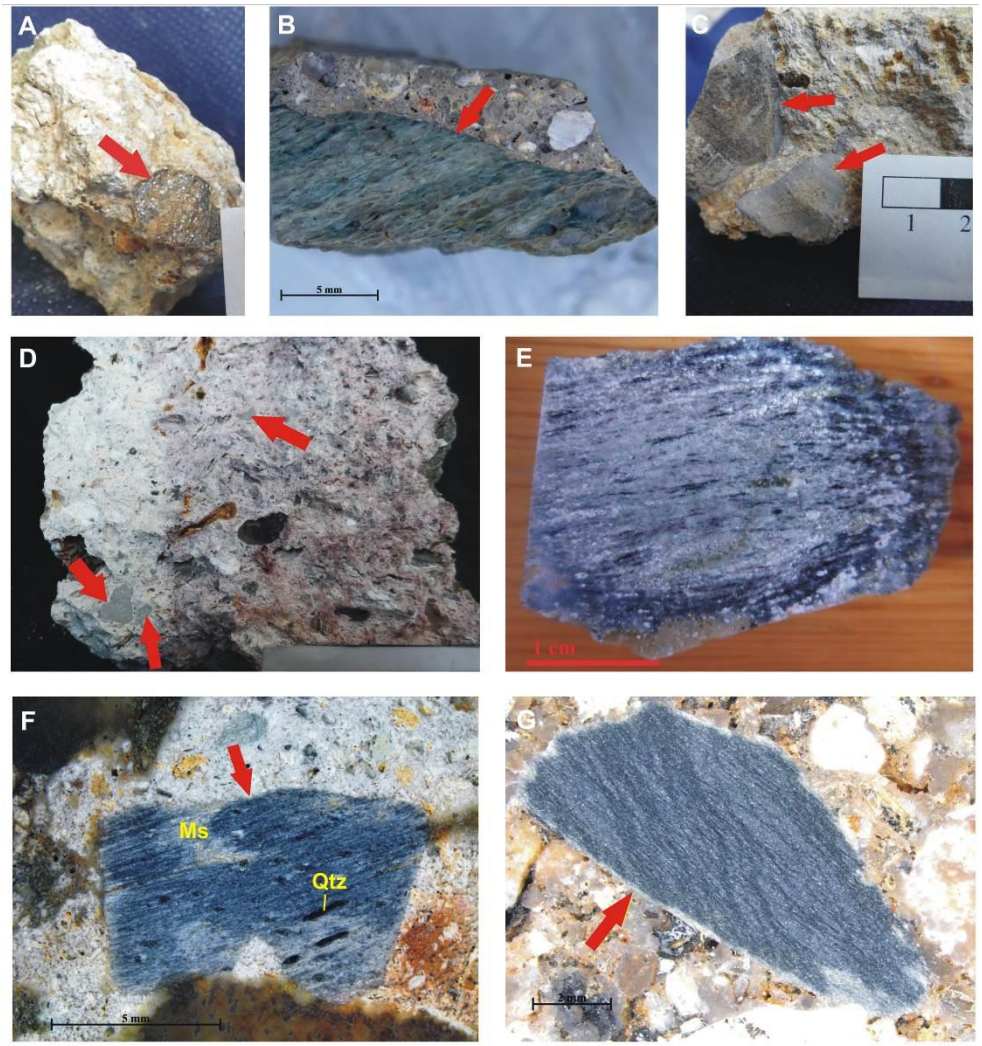

Figure 3. A) Mica schist from Felsőregmec. B) Muscovite schist from Cseresznyés, Vágáshuta. Polished surface. C) "Siliceous" xenoliths from Cseresznyés, Vágáshuta. D) Siltstone xenoliths from Megyer Hill, Sárospatak. E) Gneiss xenolith from Hársas Hill, Gönc. Polished surface. F) Slate xenolith from Kassa Hill, Ond. Ms: Muscovite, Qtz: quartz, Polished surface. G) Slate xenolith from Fekete Hill, Ond. Polished surface. Notes: Red arrows point to xenoliths.

6. Petrographic and mineralogical results

6.1. Applied analytical methods. After macroscopic grouping, the enclaves were subjected to petrographic and mineralogical investigations. The fabric-structural characteristics were investigated by polarization microscopy (PM) in transmitted light (Zeiss AX10 Imager A2m). The chemical analysis of individual grains in the samples was carried out with scanning electron microscopy (SEM) and energy dispersive spectrometry (EDX) (JEOL JXA-8600 Superprobe microprobe with RemX driving control, 15 kV, 20 nA). X-ray diffraction (XRD) analyses were performed on some enclaves with Bruker AXS D8 Advance diffractometer (Cu Kα, 33 kV, 50 mA), 2–70°(2θ) range, Bragg-Brentano geometry, Vantec-1 detector with 2° window, 0.007°(2θ)/155 sec).

6.2. Cognate enclaves. The most typical compound of the cognate enclaves is plagioclase, but pyroxene crystals and their alteration products also occur. According to SEM+EDX analyses the chemical composition of plagioclase and pyroxene is identical to the phenochrysts of the host rock.

Some cognate enclaves exhibit glomeroporphiric texture. Such enclave was collected from the subvolcanic laccolith of Kopasz Hill, Tállya, but similar enclaves are present at Bába Hill, Füzérkajata and at Préda Hill, Vágáshuta. The main mineral phase is plagioclase (about 50-75%) (Fig. 4 A–B), its size is between 80-700 μm. The amount of volcanic glass as groundmass is about 20-25%. Volcanic glass occurs in the pylotaxitic groundmass of the host rock, too. In the enclave from Kopasz Hill the space between columnar plagioclase and augite porphyric crystals is filled up by brown volcanic glass (ca. 30%). Here, volcanic glass is replaced by radial-fibrous siderite both in the enclave and in the host andesite as a result of carbonatization.

Holocrystalline enclaves are mainly microdiorites. Their fabric is equigranular; the size of the main constituent plagioclase (~70%) is ~0.5 millimetres on the average (Fig. 4 C–D). Another important phase is pyroxene. Such enclaves appear in the dacite of Hársas Hill near Gönc. A diorite enclave turned up from this place, too (Fig. 4 E–F), its mineral composition is dominated by neutral plagioclase (~65%) and biotite (~25%), which is the alteration product of augite (~10%).

The enclaves with porphyric texture contain plagioclase phenocrysts as porphyric grains. Some enclaves in dacite from Nagy-Kopasz, Tokaj belong to this group. Petrographic analyses from this group were not carried out.

6.3. Opaque mineral and biotite bearing xenoliths. Biotite and opaque mineral bearing xenoliths macroscopically resemble biotite gneiss or biotite schist (Fig. 2 C). We assume that some of the former researchers have described this type of xenoliths as biotite gneisses. However we have not found any biotite gneiss xenoliths in the Tokaj Mountains.

Xenoliths containing opaque minerals and biotite are made up mainly by plagioclase (Fig. 5 A, B, C), which have a composition similar to the phenocrysts of the host rock. The inner parts of the enclaves are frequently enveloped by an outer coarse-grained plagioclase rim (up to 0.5 millimeters size, Fig. 5 B–C). In some cases xenoliths do not have a distinct rim; plagioclase is coarse-grained throughout the enclave. Generally fine-grained plagioclase, sometimes volcanic glass is present in the inner part of the xenoliths.

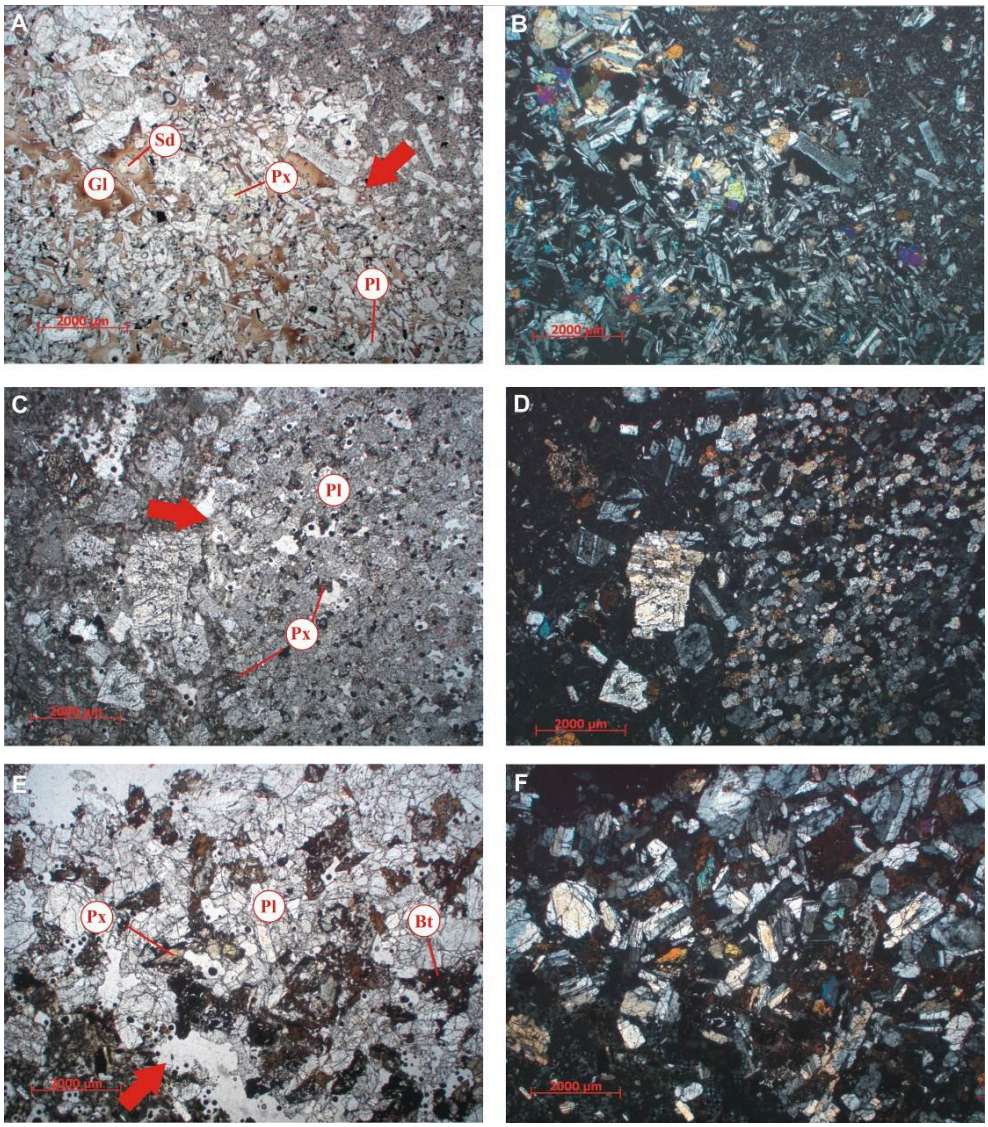

Figure 4. A) PM image of a glomeroporphyric cognate enclave from Kopasz Hill, Tállya. Parallel nicols. B) Crossed nicols. C) Cognate enclave from Hársas Hill, Gönc, microdiorite subtype. Parallel nicols. D) Crossed nicols. E) Diorite enclave (cognate?) from Hársas Hill, Gönc. Parallel nicols. Also on Fig. 2. B). F) Crossed nicols. Notes: Bt: biotite. Gl: volcanic glass. Pl: plagioclase. Px: pyroxene. Sd: siderite. Red arrows point to the enclaves.

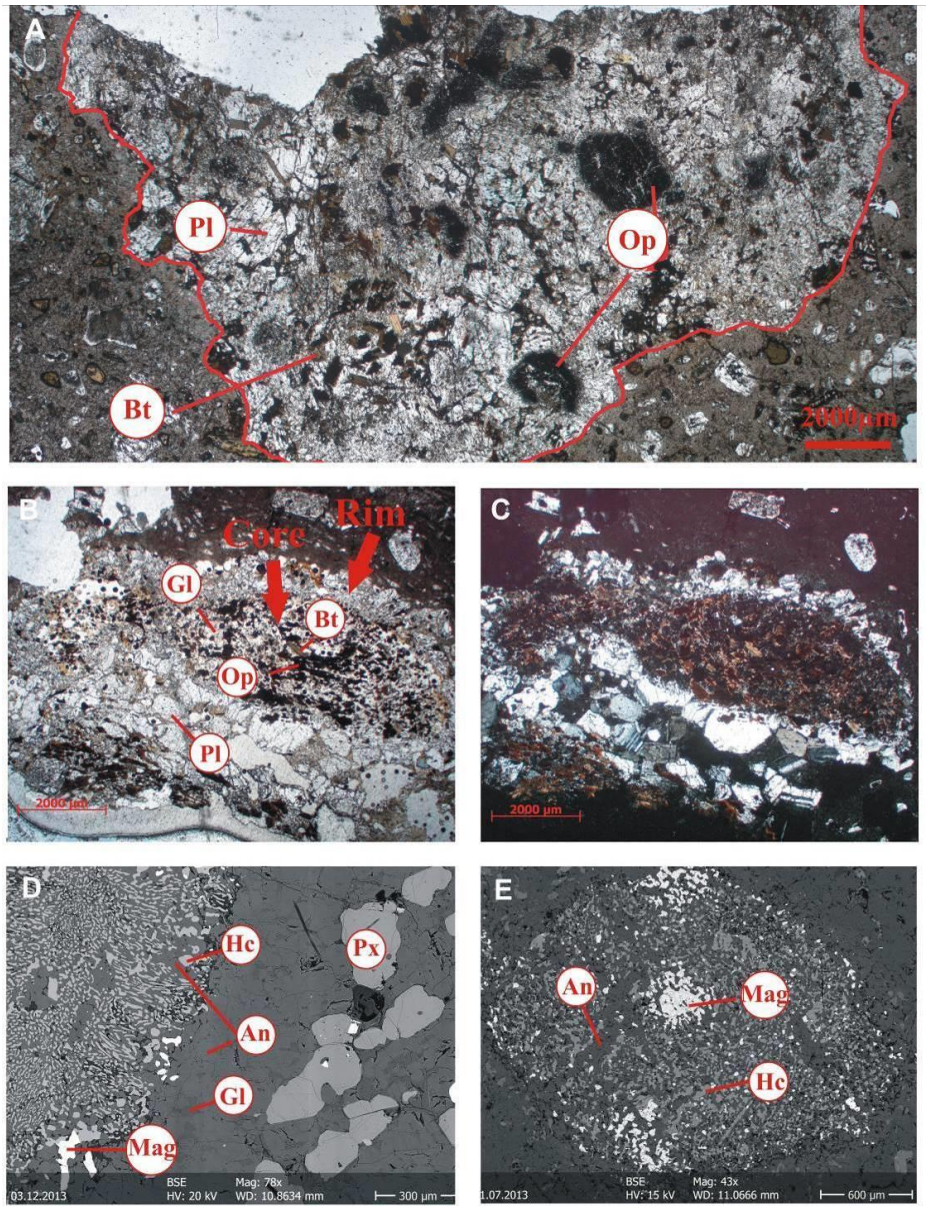

Figure 5. A) PM images of the opaque mineral and biotite bearing enclave from Cseresznyés, Vágáshuta, also on Fig. 2 C). Parallel nicols. B) Opaque mineral and biotite enclave from Bába Hill, Füzérkajata. Parallel nicols. C) Crossed nicols. D) Scanning Electron Microscope (SEM) view, spinel symplectite in opaque mineral and biotite enclave from Bohár-tető, Kovácsvágás. Also on Fig. 2 D. E) SEM image, spinel symplectite in the enclave from Cseresznyés, Vágáshuta. Also on Fig. 2 C) and Fig. 5 A). Notes: An: anorthite. Bt: biotite. Gl: volcanic glass. Hc: hercynite. Mag: magnetite. Op: opaque mineral. Pl: plagioclase. Px: pyroxene.

Here, scattered biotite crystals, opaque mineral crystals and opaque grain aggregates are located. In contrast to the plagioclase, the opaque minerals and biotite are considered to be the alteration products of extraneous material. The opaque minerals are hercynite ($Fe^{2+}Al_2O_4$) and magnetite, according to SEM+EDX results. Textural relations show that magnetite is often grown at the expense of hercynite. Magnetite generally, hercynite rarely contains exsolved ilmenite plates. The xenoliths always contain much biotite. Hercynite was identified in seven opaque mineral and biotite xenoliths. It occurs in two forms: the larger (20−500 μm) single crystals are subhedral or anhedral. The outline of the aggregates of small (10−40 μm) droplet-shaped (in one case euhedral-subhedral crystals) hercynite crystals together with magnetite and anorthite mostly resembles of isometric or stubby crystals (Fig. 5 A, E). The shape of the opaque mineral aggregates can be rounded, drop-like, too (one enclave). The hercynite aggregates occur in four thin-sections. This is a typical symplectitic fabric. Single hercynite crystals do not show symplectitic structure or reaction rims.

A biotite and opaque mineral containing xenolith studied in detail is shown on Fig. 5 A. The marginal part consists of neutral plagioclase with basic core. The inner part of the xenolith is composed of coarse-grained labradorite together with much biotite and hercynite-magnetite symplectites. Scattered pyroxene pseudomorphs filled with clay mineral are also present. Small monazite crystals (30−100 μm) occur in plagioclase unlike in the phenochrysts of the andesite. The opaque mineral symplectites (Fig. 5 D, E) consist of hercynite, magnetite and anorthite between the spinels. Magnetite contains ilmenite plates oriented along crystallographic directions.

One biotite and opaque xenolith is composed of basic plagioclase. The small space between the plagioclase tables is filled up by volcanic glass. The enclave is bordered by a narrow glass rim (~0.1 mm). The opaque minerals and biotite are accumulated in dark grey spots surrounded by a light grey edge of microcrystalline plagioclase and glass mixture (Fig. 2 D). Hercynite occurs in symplectitic groups. It is interesting that pyroxene can also form symplectites beside single crystals (only in this enclave).

6.4. Xenoliths from the basement. Petrographic studies revealed that beyond macroscopically isolated rock types, cordierite hornfels, leucogranite and biotite schist also appears. These xenoliths stem probably from Vilyvitány Block.

The leucogranite xenolith collected from Vágáshuta is not mentioned in former publications. It is composed of alkaline feldspar (~45%), plagioclase (~40%), subordinate amounts of quartz (~10%) and scarce relics of former biotite crystals. Its fabric is equigranular with 500 μm average grain size. The granite shows metamorphic signs as indicated by pertitic feldspar crystals and undulatory extinction of quartz (Fig. 6 F).

An altered claystone xenolith from Vágáshuta appears to be a silicified fine-grained rock by the naked eye (Fig. 3 C). SEM+EDX analyses revealed that it consists of the intergrowth of very fine-grained quartz and alkaline feldspar (sanidine, based on XRD analysis) which is responsible for the great strength of the rock. Sanidine may have been formed from illite during thermal reaction with magma. It contains tiny albite spots. Weak banding of the rock fragment is observable which is due to minor changes in porosity and in the K/Na ratio of feldspar.

Muscovite schist, found at the same location, is made up of quartz and muscovite (Fig. 6 A, B). Some plagioclase porphyroblasts and few, lengthwise dissected tourmaline crystals are also present. Quartz forms thin, elongated fine-grained bands, lenses or rounded

porphyroblasts which often have small tails (σ-clasts). The fabric of the rock indicates strong shear during formation.

A xenolith made up dominantly of cordierite ($Mg_2Al_4Si_5O_{18}$) and plagioclase was found in pyroxene-andesite near Kovácsvágás and was classified as cordierite hornfels (Fig. 6 C–E). Cordierite grains form slightly elongated lenses which are poorly oriented. Plagioclase laths are smaller (10−50 μm) than cordierite crystals (30−150 μm).

Hercynite appears (~10%) as single crystals or in the form of symplectites with magnetite and anorthite, as experienced in other biotite and opaque xenoliths.

Symplectitic hercynite contains significantly more Ti, V, Cr and Zn than single crystals. Some corundum crystals (several hundred μm sized) occur in the xenolith in association with single hercynite crystals (Fig. 6 E). Hercynite replaces corundum as shown by their fabric-structural relations. The cordierite+corundum+plagioclase+hercynite mineral assemblage may result from the high temperature metamorphism of the xenolith (amphibolite facies, HEIMANN et al. 2006) preceding ascending in the hot magma which may have caused relatively minor alterations compared to metamorphism. The altered rock was probably a fragment of iron rich, clayey sediment. NIŢOI et al. (2002) reported similar mineral parageneses in the xenoliths from Eastern Carpathians.

They have found corundum+spinel+alkaline feldspar+cordierite high temperature mineral assemblages, too.

Biotite schist, found at Nagy-Milic, NE from Hollóháza, is not mentioned in former publications. The schist is composed of basic plagioclase, biotite and hercynite (Fig. 7 A–C). Plagioclase contains numerous apatite needles. The xenolith shows basic composition unlike the phenocrysts in the host rock. The fragment does not show reaction rim, recrystallization did not happen. The clear plagioclase rim around the xenolith is of neutral composition similarly to the phenocrysts in the host rock indicating that the xenolith was a cooling centre for the plagioclase rim to crystallize onto. This phenomenon is observed in several biotite and opaque containing xenoliths, too.

The main constituents of the gneiss xenoliths from Hársas Hill, Gönc are ~35−40% plagioclase, ~35% quartz, ~15% biotite and ~15% cordierite. Cordierite replaces biotite in the central parts of the xenolith. The edge of the xenolith contains more biotite giving a darker colour here (Fig. 3 E, 7 E–F).

Slate xenoliths are abundant in the felsic rocks near Ond (Fig. 3 F–G). They show perfect schistosity, sometimes crenulation (Fig. 7 D) which is determined by the sericite like fine-grained material. The grain size of the xenoliths falls into the silt and clay range. The xenoliths have grey, dark grey colour due to the organic matter content. Thus the edge of several xenoliths is white as a result of organic matter oxidation (Fig. 3 G). The xenoliths consist of quartz and muscovite with minor kaolinite, monazite and Ti-dioxide. The slate xenolith from Kassa Hill, Ond (Fig. 3 F) has light parts with coarse-grained muscovite, while the darker lenses consist of quartz that indicate anchi- or epimetamorphic origin. The zeolitization of the host rhyolite tuff did not have any effect on the slate xenoliths.

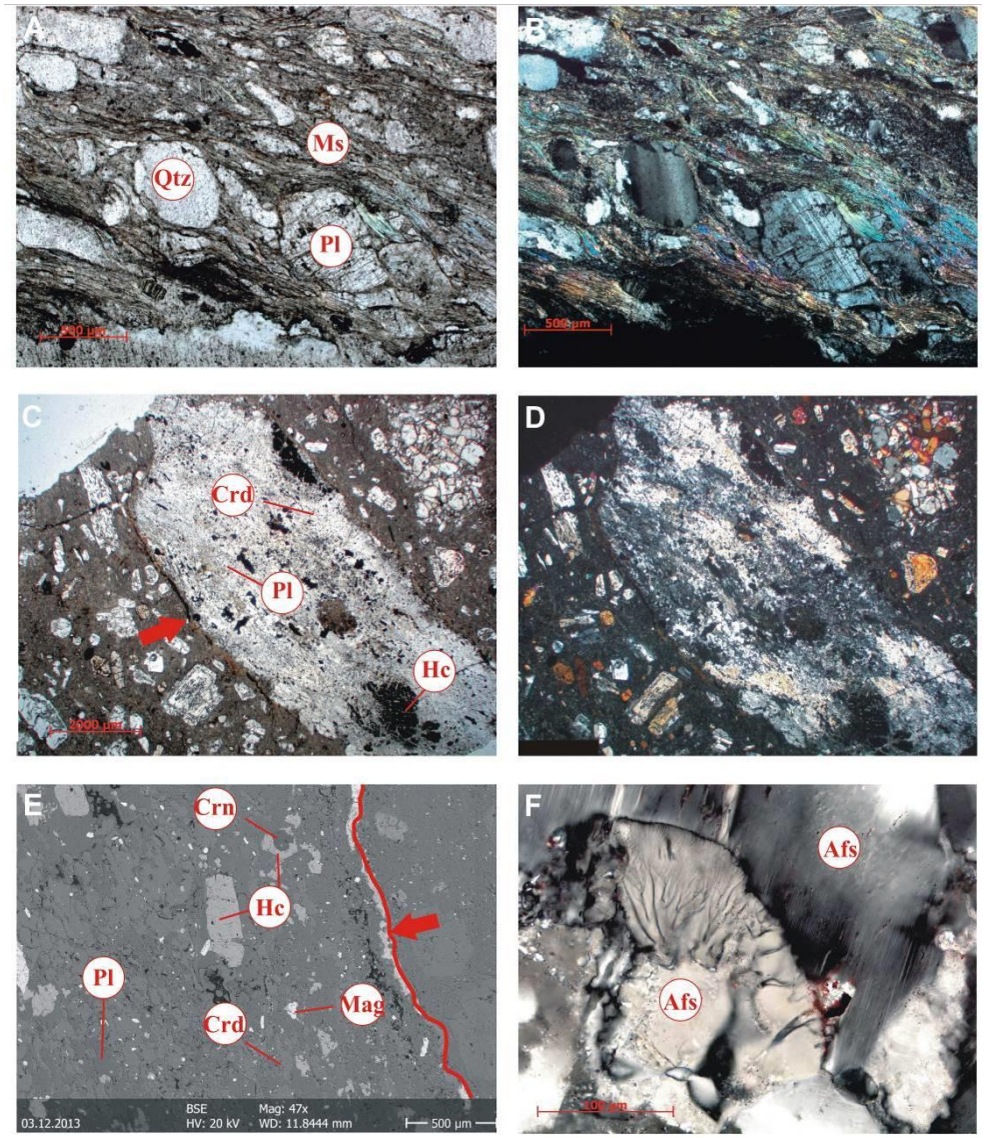

Figure 6. A) Muscovite schist from Cseresznyés, Vágáshuta. Parallel nicols. B) Crossed nicols. C) Cordierite hornfels from Bohár-tető, Kovácsvágás. Parallel nicols. D) Crossed nicols. E) SEM view of the cordierite hornfels xenolith, also on Fig. 6 C–D. F) Petrographic view of granite xenolith from Cseresznyés, Vágáshuta. Flame perthite and perthite. Crossed nicols. Notes: red arrows point towards the enclaves. Afs: alkaline feldspar. Crd: cordierite. Crn: corundum. Hc: hercynite. Mag: magnetite. Ms: muscovite. Pl: plagioclase. Qtz: quartz.

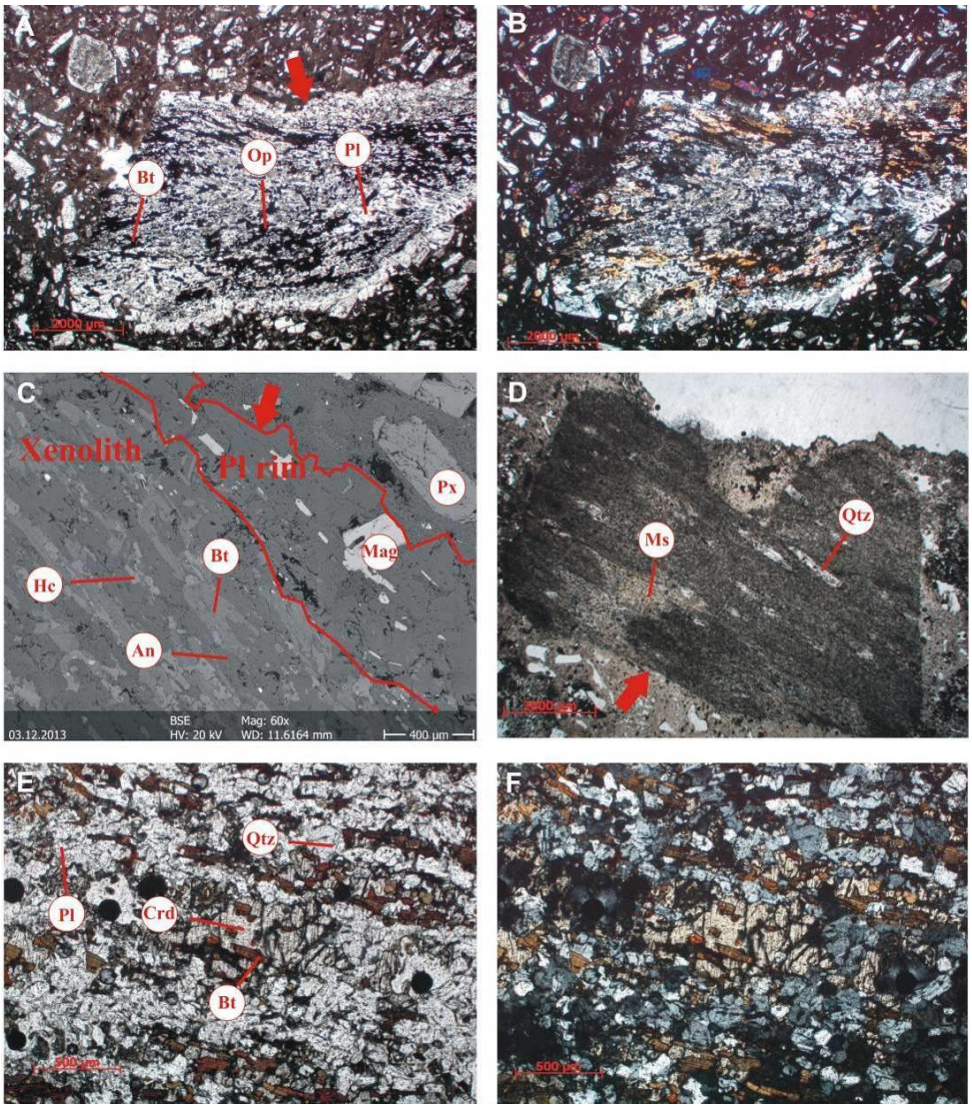

Figure 7. A) PM image of biotite schist from Nagy-Milic, Hollóháza. Parallel nicols. B) Crossed nicols. C) SEM view of the biotite schist. D) Slate from Kassa Hill, Ond. Parallel nikols. Also on Fig. 3 F. E) Gneiss xenolith from Hársas Hill, Gönc. Parallel nicols. Also on Fig. 3 E. F) Crossed nicols. Notes: An: anorthite. Bt: biotite. Crd: cordierite. Hc: hercynite. Mag: magnetite. Ms: muscovite. Op: opaque minerals. Pl: plagioclase. Px: pyroxene. Qtz: quartz.

7. Discussion

The basement of the mountains consists of mosaics of blocks with different origin. Most of the basement of the Tokaj Mountains is not known because direct evidences (borehole data) are mostly missing from this area. However, xenoliths provide a useful help to evaluate the type of rocks underlying Miocene igneous rocks.

Xenoliths from the basement constitute the most various group among enclaves and xenoliths. Based on them and drillhole evidences, we assume the basement units depicted on Fig. 9.

The presence of Zemplinicum at the NE part is well documented, since the basement is in relatively elevated position here.

The biotite schist xenolith collected at Nagy-Milic near Hollóháza may represent Zemplinicum extending north-westwards from Vilyvitány Block. Metamorphic xenoliths (mica schist, gneiss) and the newly found granite, cordierite hornfels and sanidinite xenolith from the environment of Vágáshuta may originate from the Vilyvitány Block, while the sandstone and siltstone xenoliths are fragments from the Permian-Carboniferous sedimentary sequence overlying this metamorphic assemblage. Both successions belong to the Zemplinicum (VOZÁR et al. 2010, VOZÁROVÁ & VOZÁR 1988). Therefore, in accord with the previous observations, the extension of Zemplinicum is assumed southward from Vilyvitány Block (PENTELÉNYI 1972a).

As a small unit, upper Triassic Dachstein type limestone appears in the environment of Sárospatak (PENTELÉNYI et al. 2003), as witnessed by several drillholes. The origin of these upper Triassic carbonate rocks is uncertain; they may represent Silicicum s.l., since Dachstein Limestone does not fit into the Veporic-related Zemplinic succession.

Bükkium (Szendrő Palaeozoic) occupies the Western segment of the mountains. This statement is based only on xenoliths, although their lithological character is sharply different from the xenolith types occurring elsewhere in the mts.

The lithology of the metamorphic xenoliths at the North-western part of the mountains excludes Szendrő-type basement. Based on structural considerations and on the lithology of xenoliths we suggest the presence of Veporicum-type basement although we cannot exclude the presence of Zemplinicum, either.

During the investigation of the xenoliths several signs of xenolith-magma interaction were encountered. Many xenoliths contain mineral assemblages characteristic for high temperature environment.

Sanidine formed from a pelitic, illite rich protolith (GRAPES 2006) together with quartz and albite is also the product of high temperature alteration (Fig. 3 C). Banding of the xenolith crossing its boundary excludes the possibility of formation only by the interaction with the magma, high temperature metamorphic origin is supposed instead.

The hercynite+biotite+opaque mineral paragenesis in the opaque mineral and biotite bearing xenoliths is a typical high temperature, low pressure metapelitic assemblage (NIŢOI et al. 2002, VÁSQUEZ et al. 2009, MARIGA et al. 2006a). Partial melting of these xenoliths cannot be excluded because their hercynite and other opaque mineral content is high as observed in other restitic xenoliths, too (MARIGA et al. 2006a, VÁSQUEZ et al. 2009). The similar composition of plagioclase both in xenolith and in host rock indicates that the plagioclase may have crystallized from the magma in both cases. Hercynite is always associated with minor magnetite which refers to a genetic connection between these two minerals.

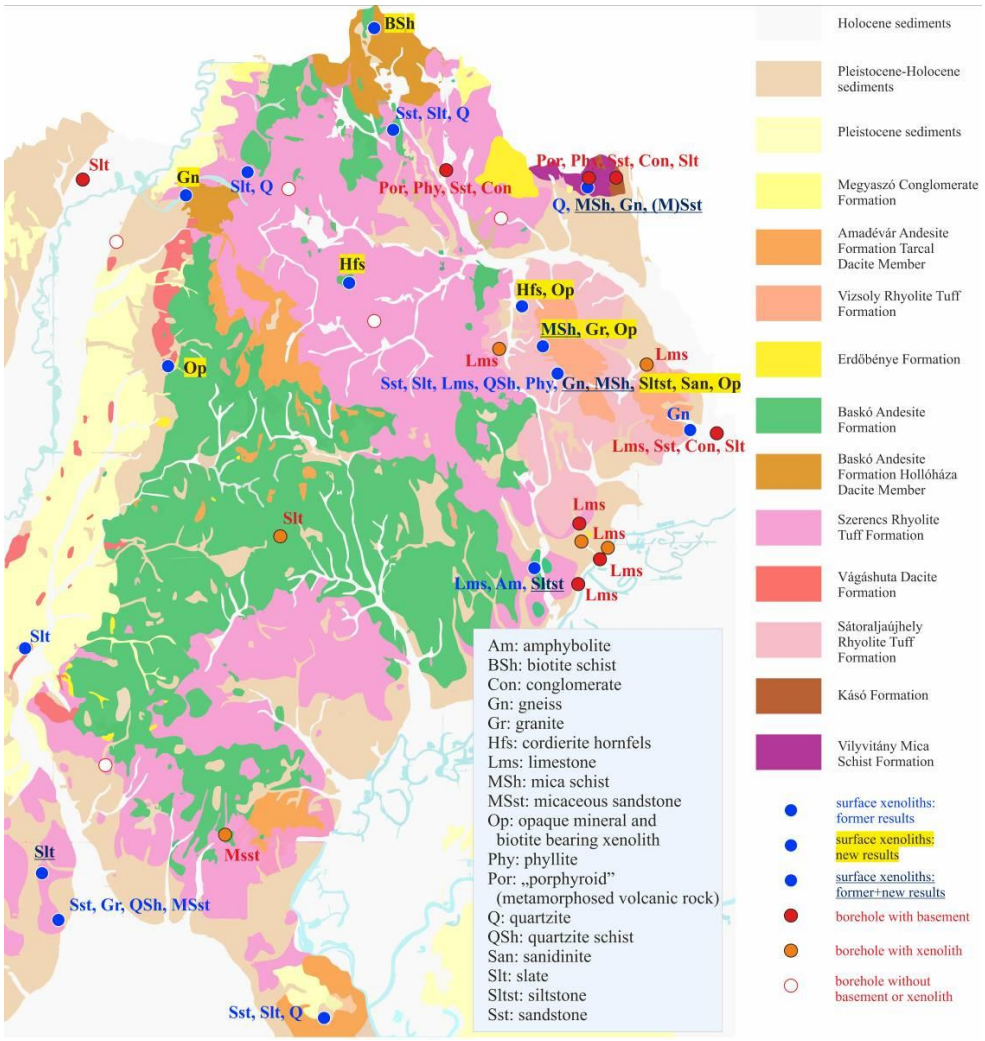

Figure 8. Borehole and xenolith data depicted on the geological map of the Tokaj Mountains (Geologic map modified after KUTI & PENTELÉNYI 2000a, b; PENTELÉNYI & KAISER 2000; SCHAREK & PENTELÉNYI 2000).

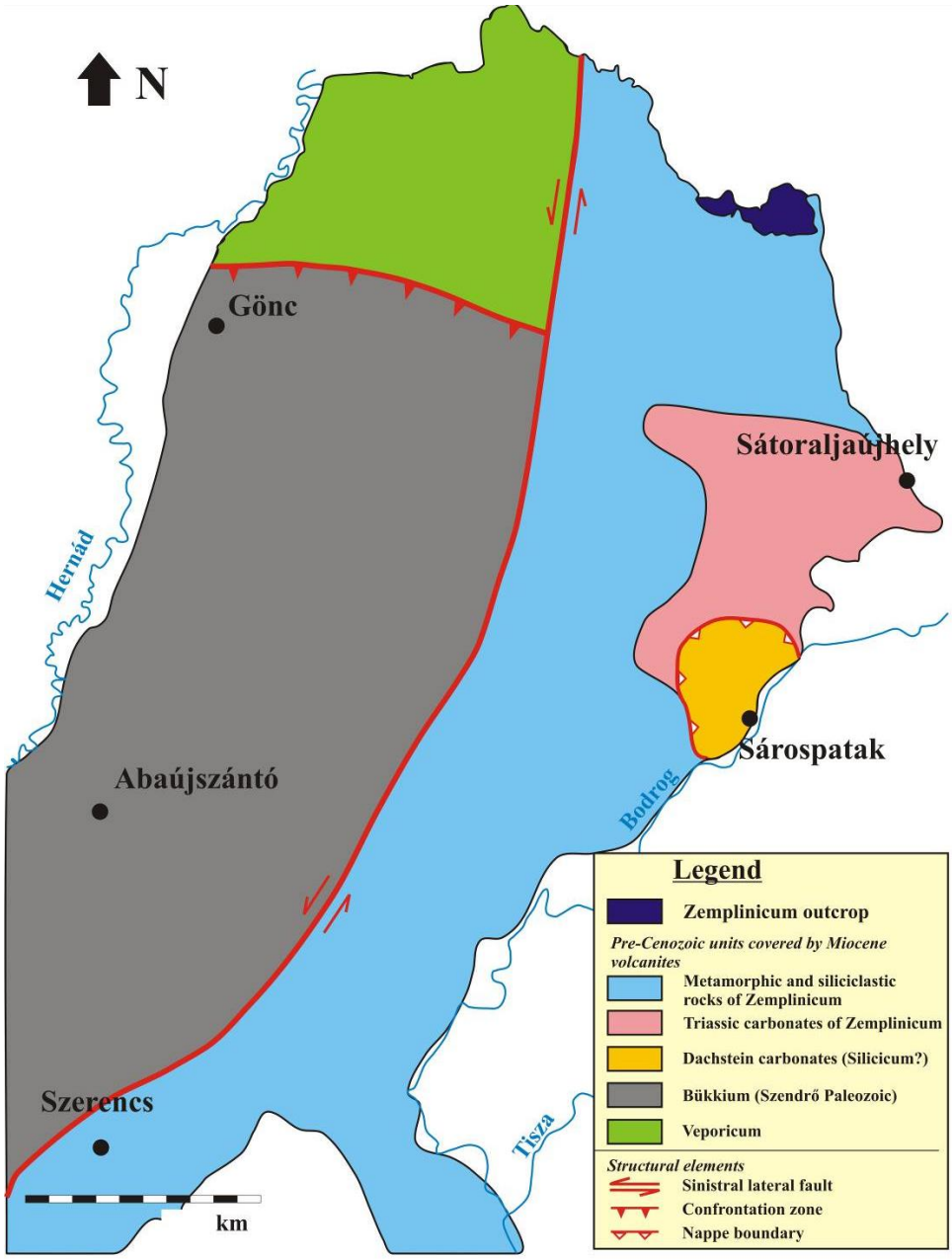

Figure 9. Schematic map of assumed basement units under the Miocene volcanic succession of the Tokaj Mountains.

The two hercynite types in these xenoliths (separated according to their fabric) are the result of two different processes or the alteration products of two different minerals based on the trace element content. Symplectitic hercynite may have been formed by the solid phase reaction (recrystallization) of corundum and magnetite, or mass transfer between magma and corundum (MARIGA et al. 2006b), formed in an earlier stage during thermal interaction with magma. Also a possible mode of formation is by the reaction between corundum of former pyrometamorphism and Fe (±Mg) released from a clayey matrix. We cannot rule out the thermal breakdown of garnet, sillimanite or pyroxene producing hercynite and plagioclase symplectites either (HIROI et al. 1997, MARIGA et al. 2006a), as the alteration was complete and has not left mineral relics. Cordierite and corundum are also common constituents in high temperature alteration processes (HEIMANN et al. 2006), but they are observed only in two samples one of which is the cordierite hornfels from Vágáshuta and Kovácsvágás. The other xenolith found between Telkibánya and Bózsva contains cordierite, plagioclase and quartz.

The biotite → cordierite process in the biotite-cordierite gneiss xenolith from Hársas Hill (Gönc) is of metamorphic origin (YOUNG et al. 1989). The second generation of biotite accumulating at the edge of the xenolith was formed by the thermal influence of the magma.

According to the fabric and mineral composition of the slate or phyllite xenoliths from Ond, the basement has undergone small grade metamorphism here.

8. Conclusions

Our investigations showed the presence of biotite schist, hornfels, sanidinite and diorite as new xenolith material types originating from the basement of Tokaj Mts. The hornfels xenolith may indicate regional metamorphism before getting into the magma or high-temperature pirometamorphism by the magma, this problem requires further research to be solved.

The biotite and opaque mineral bearing xenoliths were not investigated by previous researchers. Our results are the first which show their sedimentary origin strongly overprinted by recrystallization in contact with magmas.

Based on former findings and xenoliths collected during this work we assume Zemplinicum type basement at the E part of the mountains with a small nappe unit of the Silicicum (s.l.). The basement of the W part is divided from the E part by a supposed lateral strike-slip fault, and is composed of Bükkium- and Veporicum-type successions. Our results also support the minimal occurrence of limestone in basement xenoliths, restricted to the region of Sárospatak – Sátoraljaújhely.

9. Acknowledgments

This work was carried out as a part of Well Ahead (KÚTFŐ) project: TÁMOP-4.2.2.A-11/1/KONV 2012-0049. We are grateful for the important help of Norbert Zajzon, Tibor Zelenka, Péter Fuchs, György Szakmány, Réka Horváth and Sándor Szakáll.

10. References

[1] BÓCZÁN, B.–FRANYÓ, F.–FRITS, J.–LÁNG, S.–MOLDVAY, L.–PANTÓ, G.–RÓNAI, A. 1966: *Magyarázó Magyarország 200 000-es földtani térképsorozatához (Explanation to the geological map series of Hungary), 1:200 000, M-34 XXXIV*. Geological Institute of Hungary, 199 p.

[2] GRAPES, R. 2006: *Pyrometamorphism*. Springer, Berlin–Heidelberg–New York, 281 p.

[3] GYARMATI, P.–ZELENKA, T. 1968: *Magyarázó a Tokaji-hegység földtani térképéhez, 25 000-es sorozat (Explanation to the geological map of the Tokaj Mts.), Mád, 1:25000* (in Hungarian). Geological Institute of Hungary, 70 p.

[4] GYARMATI, P. 1977: A Tokaji-hegység intermedier vulkanizmusa (Intermediate volcanism in the Tokaj Mountains). *Annales Instituti Geologici Publici Hungarici.* 58, 196 p. (in Hungarian with English translation).

[5] HEIMANN, A.–SPRY, P. G.–TEALE, G. S.–JACOBSON, C. E. 2006: Coronas, symplectitic textures, and reactions involving aluminous minerals in gedrite-cordierite-garnet gneiss from Evergreen, Front Range, Colorado. *Canadian Mineralogist,* 44/5, 1025–1044.

[6] HIROI, Y.–MOTOYOSHI, Y.–SHIRAISHI, K.–MATHAVAN, V. 1997: Local formation of hercynite-plagioclase symplectite after garnet and sillimanite in khondalite from Habarana, Srí Lanka: Mineral textures.– *Proceedings of the NIPR Symposium on Antarctic Geosciences,* 10, 153–164.

[7] HORVÁTH, F. 1993: Towards a mechanical model for the formation of the Pannonian Basin. *Tectonophysics,* 226, 333–357.

[8] KUTI, L.–PENTELÉNYI L. 2000a: *Magyarország földtani térképe (Geological map of Hungary), Sárospatak, 1:100000*. Geological Institute of Hungary.

[9] KUTI, L.–PENTELÉNYI L. 2000b: *Magyarország földtani térképe (Geological map of Hungary), Sátoraljaújhely, 1:100000*. Geological Institute of Hungary.

[10] MARIGA, J.–RIPLEY, E. M.–LI, C.–MCKEEGAN, K. D.–SCHMIDT, A.–GROOVE, M. 2006a: Oxygen isotopic disequilibrium in plagioclase–corundum–hercynite xenoliths from the Voisey's Bay Intrusion, Labrador, Canada. *Earth and Planetary Science Letters,* 248, 263–275.

[11] MARIGA, J.–RIPLEY, E. M.–LI, C. 2006b: Petrologic evolution of gneissic xenoliths in the Voisey's Bay Intrusion, Labrador, Canada: Mineralogy, reactions, partial melting, and mechanisms of mass transfer. *Geochemistry, Geophysics, Geosystems,* 7/5, 25 p.

[12] NIŢOI, E.–MUNTEANU, M.–MARINCEA, S.–PARASCHIVOIU, V. 2002: Magma-enclave interactions in the East Carpathian Subvolcanic Zone, Romania: petrogenetic implications. *Journal of Volcanology and Geothermal Research*, 118, 229–259.

[13] PENTELÉNYI, L. 1968: *Magyarázó a Tokaji-hegység földtani térképéhez, 25 000-es sorozat (Explanation to the geological map of the Tokaj Mts.), Abaújszántó, 1:25000* (in Hungarian). Geological Institute of Hungary, 51 p.

[14] PENTELÉNYI, L. 1972a: *A Tokaji-hegység monográfiája (Monography of the Tokaj Mountains)*. Geological Institute of Hungary. Manuscript, 460 p.

[15] PENTELÉNYI, L. 1972b: *Magyarázó a Tokaji-hegység földtani térképéhez, 25 000-es sorozat (Explanation to the geological map of the Tokaj Mts.), Füzérradvány–Széphalom, 1:25000* (in Hungarian). Geological Institute of Hungary, 60 p.

[16] PENTELÉNYI, L–KAISER M. 2000: *Magyarország földtani térképe (Geological map of Hungary), Gönc, 1:100000.* Geological Institute of Hungary.
[17] PENTELÉNYI, L.–HAAS, J.–PELIKÁN, P.–PIROS, O. 2003: A Zempléni egység magyarországi részén feltárt triász képződmények újraértékelése (Reambulation of Triassic formations exposed at the Hungarian part of Zemplin Unit). *Földtani Közlöny,* 133/1, 1–21.
[18] SCHAREK, P.–PENTELÉNYI L. 2000: *Magyarország földtani térképe (Geological map of Hungary), Szerencs, 1:100000.* Geological Institute of Hungary.
[19] SOLLAS, J. W. 1894: On the volcanic district of Carlingford and Slieve Gullion, Part I. On the relation of the granite to the gabbro of Barnavave, Carlingford. *Transactions of the Royal Irish Academy,* 30, 477–512.
[20] SZABÓ, Cs.–HARANGI, Sz.–CSONTOS, L. 1992: Review of Neogene and Quaternary volcanism of the Carpathian-Pannonian region. *Tectonophysics,* 208, 243–256.
[21] VÁSQUEZ, P.–GLODNY, J.–FRANZ, G.–ROMER, R. L.–GERDES, A. 2009: Origin of fayalite granitoids: New insights from the Cobquecura Pluton, Chile, and its metapelitic xenoliths. *Lithos,* 110, 181–198.
[22] VOZÁR, J.–EBNER, F.–VOZÁROVÁ, A.–HAAS, J.–KOVÁCS, S.–SUDAR, M.–BIELIK, M.–PÉRÓ, Cs. 2010: *Variscan and Alpine terranes of the Circum-Pannonian Region.* Slovak Academy of Sciences, Geological Institute 232 p.
[23] VOZÁROVÁ, A.–VOZÁR, J. 1988: *Late Paleozoic in West Carpathians*. Dionýz Štúr Intitute of Geology, Bratislava. 320 p.
[24] YOUNG, E. D.–ANDERSON, J. L.–CLARKE, H. S.–THOMAS, W. M.–1989: Petrology of Biotite-Cordierite-Garnet Gneiss of the McCullough Range, Nevada I. Evidence for Proterozoic Low-Pressure Fluid-Absent Granulite Grade Metamorphism in the Southern Cordillera. *Journal of Petrology,* 30/1, 39–60.
[25] ZALAI, P. 1991: *A Zempléni-hegység regionális geofizikai kutatási programja (Regional geophysic research programme of the Zemplén Mts). Research report*. Eötvös Loránd Geophysical Institute, 80 p.

Geosciences and Engineering, Vol. 2, No. 4 (2013), pp 27–46.

NONLINEAR REGRESSION MODEL FOR PERMEABILITY ESTIMATION BASED ON ACOUSTIC WELL-LOGGING MEASUREMENTS

NORBERT PÉTER SZABÓ–CSILLA KALMÁR

Department of Geophysics, University of Miskolc

1. Abstract

Full waveform sonic logging is routinely applied in the oil industry practice. The primary and secondary waves inform about the porosity, elastic parameters and the orientation of in-situ stresses acting around the borehole. The separation of Stoneley waves propagating in the drillhole enables to determine the permeability of hydrocarbon reservoirs. Permeability is generally estimated from the inversion processing of Stoneley-interval transit-time data. Statistical methods can also be found in the literature, which offer quicker and simpler solution for revealing the empirical relationships between the characteristic data of Stoneley-waves and permeability. These methods do not require the prior knowledge of porosity. Case studies assume a linear connection between the relative decrease in Stoneley-wave's velocity of porous formations and the natural logarithm of permeability, which usually gives only a rough estimate. In this study, the regression model is improved by the determination of a more accurate nonlinear relationship between Stoneley-wave slowness and permeability. The new statistical algorithm is tested over a wide domains of petrophysical parameters using an exactly known permeability model and synthetic well logs. The exponential model is also applied to the statistical processing of real well-logging data, where the estimated permeability log is compared to laboratory data measured on core samples. The quality checks of synthetic and field results show that the application of the nonlinear model is highly recommended to get a more accurate and reliable estimation of hydrocarbon reserves.

2. Introduction

Sonic logging is a widely used borehole geophysical method in hydrocarbon exploration. Primary porosity can be determined from refracted P-wave transit times when the sonic travel times of the matrix and fluids filling the pore space are known (RAYMER et al. 1980). When different types of fluids are present in the rock, also their saturations must be quantified. The porosity calculated by acoustic logs is essential for estimating the secondary porosity of fractured formations, because the porosity obtained from acoustic method does not contain the secondary porosity part of the effective porosity. This porosity value must be compared to that of another method such as neutron-porosity or density measurement that includes both the primary and secondary components of the effective porosity (ELLIS and SINGER 2007).

The use of full waveform data in open holes – beyond determination of porosity – gives further possibilities. Using the shear and surface wave transit-times, it is possible to reveal the presence and orientation of fractures induced in the formation by natural or artificial processes, the anisotropy and magnitude of the stress-field acting in the environment of the borehole and the elastic parameters and permeability of the formation. The above characteristics are of fundamental importance for planning the hydraulic layer-fracturing, for the determination of fluid inflow to the well, with which it is possible to optimize the exploitation procedure (BADRI et al. 2000). The physical background of sonic wave

propagation with several hydrocarbon industry applications were summerized by HALDORSEN et al. (2006). The direct determination (through drilling) of formation permeability is possible using nuclear magnetic resonance (NMR) logging, but this method is very expensive. This is why in our domestic practice it is not widely used today (COATES et al. 1999). The use of NMR log is promissing for the future, because beyond the determination of effective porosity it is possible to determine the distribution of pore-sizes and the viscosity of the fluid filling the pore space. The latter quantity is in relation with fluid mobility (permeability/viscosity ratio) which is one of the basic parameters used in modeling sonic wave propagation in porous-permeable formations. The indirect (in-situ) methods for the calculation of permeability are based on the determination of formation porosity and bound-water saturation. If we evaluate the current methods used for data processing, we see that all methods have their weaknesses, because the results are often in contradiction with those determined from core samples or the estimation error of permeability may reach one (one and half) order of magnitude. Thus, the introduction of a new (independent) method could be of utmost importance. The common application of the new method and the existing ones can improve the accuracy and reliability of permeability estimation. The Stoneley-waves are surface waves propagating on the boundary of the mud column and the rock formation. Their velocity slightly varies with frequency. They can be generated with a monopole source, which emits wave-energy with equal intensity in all directions. Detection is done with a so called "array" type sonde, which may contain even several monopole sources and a group of receivers. In comparison with the classical borehole compensated (BHC) tools the monopole receivers have smaller spacing. Thus, higher vertical resolution can be reached. Owing to the construction of the sonde, because of the bigger source-receiver distance it is easier to separate the components of the wave train and, with the common processing of channels a higher signal-to-noise ratio can be reached. The low frequency component of the detected Stoneley-spectrum is the most sensitive one to the permeability of primary porosity reservoirs.

There have been many attempts to use the Stoneley-waves for reservoir characterization. BIOT (1955) has worked out the motion equation valid in porous media. With the aid of this equation the Stoneley-wave phenomenon may be related to the porosity and permeability of homogeneous and isotropic media, in case of elastic behaviour of the rock matrix and viscous porous fluid. The relation between the attenuation of the Stoneley-wave and permeability of the formation was predicted theoretically by ROSENBAUM (1974). The low frequency case of the dispersive wave was examined by WHITE (1983) and MATHIEU and TOKSÖZ (1984). WILLIAMS et al. (1984) have found a quantitative relation between permeability and attenuation of the Stoneley wave. The simplified models based on the Biot-theory were developed by SCHMITT et al. (1988) and CHANG et al. (1988). These were also confirmed by laboratory measurements (WINKLER et al. 1989). Based on the Biot-Rosenbaum model, TANG and CHENG (1994) developed an inversion method for processing Stoneley interval transit-time data which is still considered to be standard for the determination of sonic permeability. Within the frame of this method at several frequencies (between 0.2 and 0.8 kHz) fluid mobility is estimated with the joint inversion of Stoneley-slowness and attenuation data.

Besides the "complicated" inversion procedures there exist also some approximate procedures using empirical relations based on a multitude of field measurements, which estimate permeability from the measured and theoretical Stoneley-slowness ratios (i.e. Stoneley-index). BUFFIN (1996) published a method based on a crossplot technique, which

showed a good conformity between the estimated permeability values and the same data measured on core samples in Australian hydrocarbon exploration wells. BALA (2010) applied successfully the same statistical method for the investigation of miocen gas reservoirs in Poland. The advantage of the method is that it does not require the precalculation of porosity. Its disadvantage is that the linear or sequentially linear aproximation used by the two authors does not show high correlation between the Stoneley-index and permeability. Until now the method has been tested only on field data, therefore we found it necessary to test it on syntetic data, too.

In this study, we start from a known permeability model, then, after processing the syntetic well-logging data calculated on the model, we analyze how the exact permeability values are reconstructed. We describe that the correlation coefficient measured between the Stoneley-index and permeability can be improved if we consider the relation between the two variables non-linear. We test the statistical method on the wide domains of relevant petrophysical parameters applying homogenous and inhomogenous models. Using the non-linear regression model resulted from the syntetic tests we present also the evaluation of a field data set, which demonstrates the feasibility of the improved method.

3. Stoneley-waves in porous media

The Darcy-equation describes the flow of fluids in porous-permeable rocks

$$\frac{\partial \mathbf{u}}{\partial t} = -\frac{K}{\Phi \eta} \nabla p \,, \tag{1}$$

where K [m^2] denotes permeability, Φ [v/v] is porosity, η [Pa·s] is viscosity, $\mathbf{u}$ [m] is the relative displacement vector of the fluid and p [Pa] is the pore pressure. If the rock-matrix is considered to be incompresible the volumetric deformation of the (ideal) fluid filling the pore-space fullfils the Hook-equation

$$-\nabla \mathbf{u} = \frac{\Phi}{B_f} p \,, \tag{2}$$

where B_f [Pa] is the bulk modulus of the pore fluid (the ratio of the applied pressure and volumetric deformation). Eliminating $\mathbf{u}$ from equations (1) and (2) we get the following diffusion relation

$$\frac{\partial p}{\partial t} = C_0 \nabla^2 p \,, \tag{3}$$

where $C_0 = KB_f / \eta\Phi$ is the diffusion coefficient. In the case of elastic porous medium BIOT (1962) has found the relation between stress and strain. Based on this, calculation of the diffusion coefficient in equation (3) needs to be modified

$$C = \frac{C_0}{1 + \frac{B_f}{\Phi B}\left[(1-\alpha)(\alpha-\Phi) + \frac{\alpha^2}{1+(4\mu/3B)}\right]}, \tag{4}$$

where B is the bulk modulus of the dry rock (matrix) and μ [Pa] is the shear modulus. (The porosity of the dry and fluid saturated formation is considered to be equal). The elasticity parameter α is defined by the Biot–Gassmann-equation

$$B_c = B + \alpha^2 M = B + \left(1 - \frac{B}{B_s}\right)^2 \left(\frac{\Phi}{B_f} + \frac{\alpha - \Phi}{B_s}\right)^{-1}, \tag{5}$$

where B_c is the bulk modulus of the porous (saturated with water or hydrocarbon) formation and B_s is the same for the case of rock matrix.

The slightly dispersive Stoneley-wave is the slowest component of the sonic wave-train exhibiting the highest amplitude. The studied frequency range of this Stoneley-wave is generally between 0-10 kHz (the centre frequency is around 0.5 kHz) and it propagates, at low frequency as a tubewave in the borehole. The velocity of the tubewave in an impermeable formation ($v_{St}^{(imp)}$) is

$$v_{St}^{(imp)} = \frac{v_m}{\sqrt{1 + \frac{B_m}{\mu}}}, \tag{6}$$

where v_{m} [m/s] is the propagation velocity of the sonic wave in the mud and B_{m} is the bulk modulus of the mud. In porous-permeable formations the tubewave displaces the fluid particles relative to the matrix. This burns up some part of the wave energy. This phenomenon is accompanied by the attenuation and slowing down of the sonic waves. At low frequencies wave velocity becomes a complex quantity $v = \left[B^* / \rho_m\right]$, where B^* represents the complex bulk modulus of the mud and ρ_m is its density.

Because of pressure both the borehole of radius a and the pore fluid exhibit radial displacement. Based on the diffusion relation (3), considering mud pressure to be a harmonic function of time, the velocity ($v_{St}^{(p)}$) of tubewave in a permeable formation is given by the following equation (NORRIS 1989)

$$v_{St}^{(p)} = v_{St}^{(imp)} \left[1 - \Phi \frac{\mu}{\mu + B_m} \frac{B_m}{B_f} \sqrt{\frac{C_0}{C}} \sqrt{\frac{iC_0}{\alpha^2 \omega}}\right], \tag{7}$$

where ω [Hz] is the angular frequency of the compression wave (i is the imaginary unit). Since the diffusion coefficient depends on permeability and porosity, the propagation velocity in a permeable formation according to equation (7) decreases from $v_{St}^{(imp)}$ to $v_{St}^{(p)}$. The imaginary part of equation (7) describes the attenuation of the Stoneley-wave. This quantity increases with porosity and permeability, but decreases with the diameter of borehole. The above theoretical relation is confirmed by laboratory measurements, too. WINKLER et al. (1989) conducted observations on nearly homogeneous Berea sandstone and also on other samples produced artificially, in the 0–100 kHz frequency range. The dispersive properties of the Stoneley-waves were studied using model calculations by BRIE et al. (2000). They found that with growing fluid mobility the phase velocity and attenuation grow, also, significantly as a function of frequancy. They demonstrated that in the low frequency range propagation velocity reacts more significantly to the variation of permeability while in the high frequency range attenuation is the most sensitive to that. Based on these observations, it is possible to designate an optimal frequency around which both measurements can be applied. The above theory represents the base of those data processing methods which determine permeability based on Stoneley interval-times.

4. Non-linear permeability model

BUFFIN (1996) plotted the square of the measured Stoneley interval-times $\left(\Delta t_{St}^{(m)}\right)$ at low frequencies and the square of shear-wave interval-times $\left(\Delta t_{s}^{(m)}\right)$ normalized to the measured bulk density $\left(\rho_b^{(m)}\right)$ in the same co-ordinate system. On this crossplot the impermeable formations are represented along a line which is called shale-baseline. This line gives the calculated (theoretical) value of the Stoneley-wave slowness $\left(\Delta t_{St}^{(c)}\right)$ which does not include the effects of hole-diameter and other environmental factors (i.e. drilling mud and mudcake)

$$\Delta t_{St}^{(c)} = \sqrt{\frac{\rho_{mf}}{\rho_b}\Delta t_s^2 + \Delta t_{mf}^2}\ , \tag{8}$$

where ρ_{mf} and Δt_{mf} are the bulk density of the mudfiltrate and its sonic interval-time. Based on equation (8) the slope of the shale line is ρ_{mf} and the intersection with ordinate axis is Δt^2_{mf} in the given co-ordinate system. Relative to the shale base-line the measurement points which appear towards the bigger Stoneley interval-time (slowness) values indicate permeable formations on the crossplot. It was determined from field observations that permeability of primary porosity rocks is directly proportional to the magnitude of deviation from the shale base-line. The decrease of Stoneley-wave velocity relative to the impermeable formation is expressed by the Stoneley- index which is defined as the ratio of the measured and calculated Stoneley travel times

$$I_{St} = \frac{\Delta t_{St}^{(m)}}{\Delta t_{St}^{(c)}}\ . \tag{9}$$

The statistical procedures given in literature assume a linear relationship between permeability and Stoneley-index, where the regression coefficients depend on litology, porosity and pore content. Both the field results of other authors and our own calculations show that the above relation is not typically linear and this is mostly significant in the range of small permeabilities.

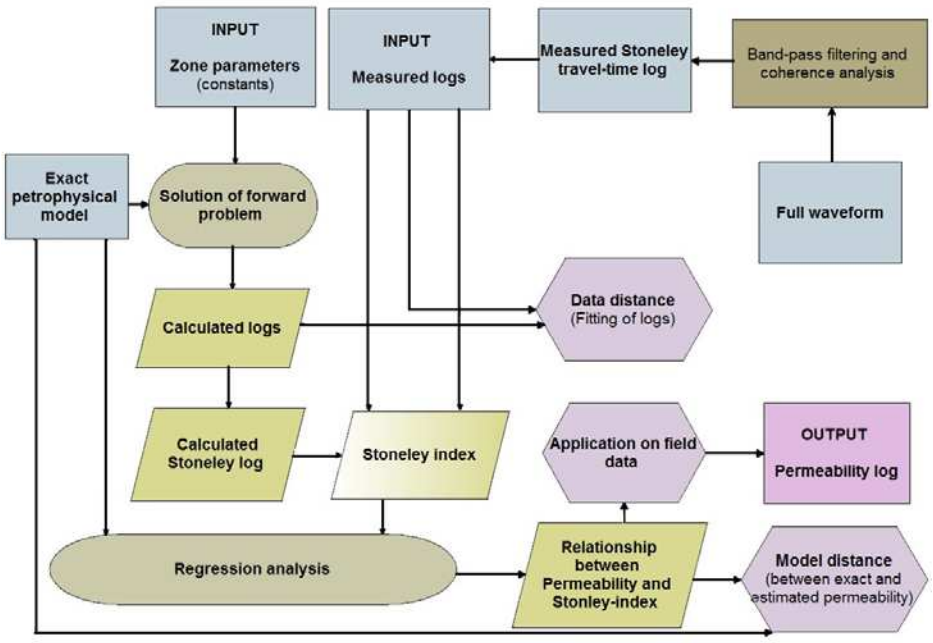

Figure 1

Statistical algorithm for permeability prediction

In Figure 1 the basic steps of our suggested modeling procedure are shown. Using the workflow, it is possible to determine the relationship between the Stoneley-index and permeability. The input data of the statistical procedure is given by the measured borehole logs such as natural gamma-ray intensity (GR [API]), density measured by gamma-gamma probe (ρ_b [g/cm^3]), shear-wave interval-time (Δt_s [μs/m]) and Stoneley interval-time (Δt_{St} [μs/m]). Well-logging data can be related to the parameters of the petrophysical model. A part of the model parameters changes rapidly with depth, others can be regarded constant within a longer zone. The first group of parameters should be determined point-by-point during the evaluation of the reservoirs. The porosity (Φ [v/v]), water saturation in the flushed zone (S_{xo} [v/v]), shale volume (V_{sh} [v/v]), sand volume (V_{sd} [v/v]) and permeability (K [mD]) are grouped among those reservoir parameters which can be determined individualy or by using an inversion method. The other group including zone parameters are set from laboratory measurments, literature or preliminary knowledge of the

measurement area. The forward problem can be solved by using constant values of longitudinal wave slowness of mud filtrate (Δt_{mf}), density of mudfiltrate (ρ_{mf}), longitudinal wave slowness of the shale (Δt_{sh}), shale density (ρ_{sh}), longitudinal wave slowness of the sand (Δt_{sd}), sand density (ρ_{sd}), hydrocarbon P-wave slowness (Δt_{hc}), hydrocarbon density (ρ_{hc}), natural gamma-ray intensity of the sand (GR_{sd}) and shale (GR_{sh}).

The functions describing the relation between well-logging data and model parameters are called theoretical probe response functions. For solving the forward problem we used the following response equations

$$\rho_b^{(c)} = \Phi\left[\rho_{mf} S_{xo} + (1 - S_{xo})\rho_{hc}\right] + V_{sh}\rho_{sh} + V_{sd}\rho_{sd}\,, \tag{10}$$

$$GR^{(c)} = GR_{sd} + \frac{1}{\rho_b^{(c)}}\left(V_{sh} GR_{sh}\rho_{sh} + V_{sd} GR_{sd}\rho_{sd}\right), \tag{11}$$

$$\Delta t_S^{(c)} = \sqrt{3}\left\{\Phi\left[\Delta t_{mf} S_{xo} + (1 - S_{xo})\Delta t_{hc}\right] + V_{sh}\Delta t_{sh} + V_{sd}\Delta t_{sd}\right\}, \tag{12}$$

$$\Phi + V_{sh} + V_{sd} = 1\,. \tag{13}$$

The theoretical values of Stoneley slownesses can be calculated by equation (8). Equation (13) is the material balance equation valid in unit bulk volume. Based on the measured and calculated Stoneley slownesses, it is possible to formulate the Stoneley index which can be related to permeability values originating from other (independent) sources. According to our experience the regression function is

$$\ln(K) = a - be^{-cI_{St}^{\kappa}}\,, \tag{14}$$

where *a, b, c* are regression coefficients and κ is a suitably scaled factor. The value of permeability ($K^{(St)}$) estimated by regression analysis can be compared, in case of field measurements with permeability data determined from other methods or, in case of syntetic tests, with exact permeability ($K^{(e)}$) values. The fitting of the different results can be measured by a model distance

$$D_m = \sqrt{\frac{1}{N}\sum_{i=1}^{N}\left(K_i^{(St)} - K_i^{(e)}\right)^2}\cdot 100[\%]\,, \tag{15}$$

where N is the number of depth-points along the borehole. The distance between the measured and calculated data is called data distance. The strenght of linear dependence between the Stoneley-index and permeability is traditionally characterized by the Pearson's correlation coefficient (r). But, for the characterization of the reliability of model (14) the rank correlation coefficient is a more suitable quantity. In case of non-linear relationships it

gives a more realistic evaluation and it is less influenced by outlying data (SPEARMAN 1904). For the calculation of rank correlation we used the following approximate formula

$$R = 1 - \frac{6\sum_{n=1}^{N} \delta_n^2}{N(N^2 - 1)} \ , \tag{16}$$

where δ_n is the difference between the ranks of the n-th data of the two variables. When the value of the above correlation coefficient is nearly 1, it shows a close (non-linear) relationship.

5. Model calculations using syntetic data

Consider that the parameters of the petrophysical model (porosity, water saturation, permeability etc.) are exactly known. By means of equation (8) and response equations (10)–(13), we can generate syntetic well logs. The values of zone-parameters of the response equations are given in table 1.

Table 1

Zone parameters of theoretical probe response equations

ρ_{mf} [g/cm^3]	ρ_{sd} [g/cm^3]	ρ_{sh} [g/cm^3]	ρ_{hc} [g/cm^3]	GR_{sd} [API]	GR_{sh} [API]	Δt_{mf} [μs/m]	Δt_{sd} [μs/m]	Δt_{sh} [μs/m]	Δt_{hc} [μs/m]
1.0	2.65	2.4	0.15	10	160	630	184	330	1050

By contaminating the synthetic data with random noise of different levels, it is possible to calculate quasi measured borehole logs to test how exactly the statistical procedure reconstructs the parameters of the exact model. This experiment evaluates the performance of the method, i.e. it characterizes its accuracy, stability and shows its noise sensitivity. During the tests, we compare the Stoneley-index to exact permeability values, which were taken from the generally accepted formula suggested by TIMUR (1968)

$$K = 0{,}136\left(\Phi^{4.4} / S_{w,irr}^2\right) , \tag{17}$$

where $S_{w,\,irr}$ [v/v] represents the bound-water saturation. The sand content is calculated from equation (13) deterministically. The syntetic tests are performed both on homogenous and inhomogenous models using well logs with different uncertainties, respectively.

6. Test on homogeneous model

The model parameters given in Table 2 represent the petrophysical model of a sedimentary structure (Model-I). The sequence of beds is composed of five shaly sandy layers. At the top a shaly-sand layer can be found, which is followed by a water reservoir containing smaller amount of shale. The third layer is shale, which separates the above water-bearing layer from the gas reservoir that is placed under it. The lithologic column ends with a shale bed downmost. The value of permeability covers five orders of magnitude. In the reservoirs

the proportion of bound-water is small due to a small amount of shale, about 20%, while in the impermeable layers it is 80–100%. The Stoneley-slownesses were calculated in the layers and were increased proportional to permeability. It resulted in quasi measured Stoneley interval times. The increment was chosen from the literature (0–15%). In the given case, we did not add noise to the synthetic well log data.

Table 2

Petrophysical parameters of layer-wise homogeneous model

Depth [m]	Φ [v/v]	S_{xo} [v/v]	V_{sh} [v/v]	$S_{w,irr}$ [v/v]	Δt_{St} [μs/m]	K [mD]
0–4.9	0.15	1.0	0.5	0.6	691	5.65
5–9.9	0.23	1.0	0.3	0.2	738	333
10–12.9	0.07	1.0	0.8	1.0	674	0.07
13–19.9	0.25	0.7	0.1	0.2	793	481
20–24.9	0.10	1.0	0.7	0.8	678	0.53

The crossplot of quasi measured Stoneley- and shear-wave slownesses can be seen in Figure 2.

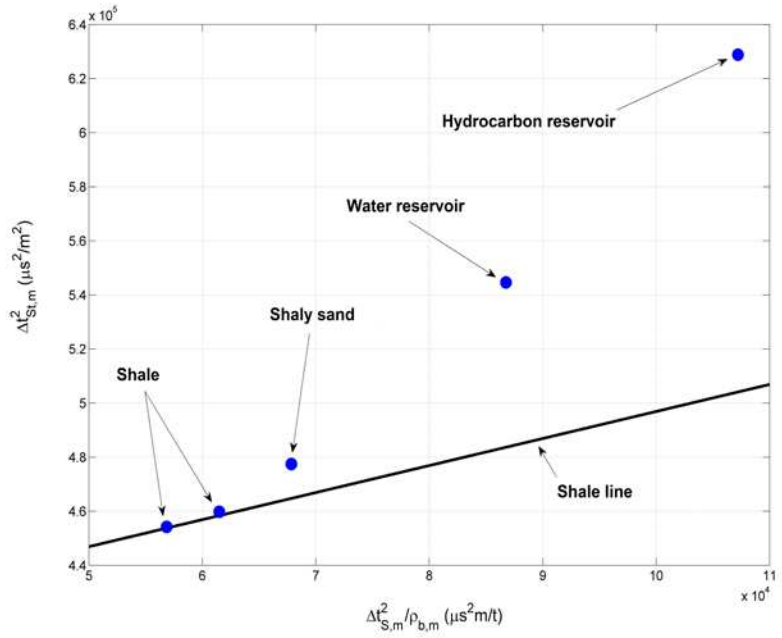

Figure 2

Stoneley- versus shear wave slowness (Model-I)

The baseline shows the impermeable layers, of which equation is

$$\Delta t_{St}^2 = \frac{\Delta t_s^2}{\rho_b} + 396900 \ . \tag{18}$$

The water-bearing and hydrocarbon reservoirs appear in the domain of increasing sonic interval times. The higher the deviation of the data from the shale line the higher the permeability of the sedimentary formation. The measurement of this effect is applied to permeability prediction using the acoustic wave train signals.

In noiseless situation, the Stoneley-index with permeability leads to regression relationship (14), where $a = 6$, $b = 7.28$, $c = 11.4$ (Figure 3). Compared to permeability the Stoneley-index changes several orders of magnitude smaller degree, then we chose $\kappa = 4$ in equation (14).

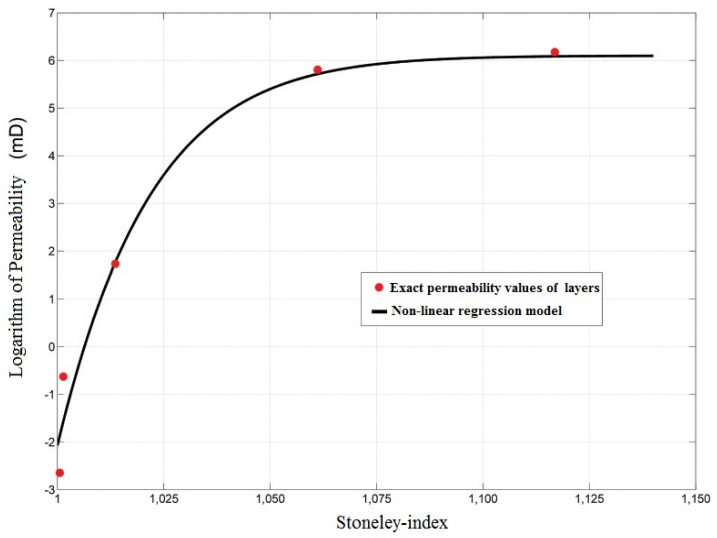

Figure 3

Natural logarithm of permeability versus Stoneley-index (Model-I)

In Figure 4 the applied borehole logs are shown (GR – natural gamma-ray intensity, RHOB – bulk density, DTS – shear wave slowness, DTSTC – calculated Stoneley-slowness, DTSTM – measured Stoneley-slowness, DDTST – difference of measured and calculated Stoneley-slownesses), the bulk volumes (POR – porosity, VSH – shale content, VSD – sand volume), the pore-content (SHCIRR = 1–SX0 – irreducible hydrocarbon saturation, SWIRR – bound water saturation) and the Stoneley-index (IST) as a function of relative depth. On the last track we present the Timur-permeability (PERMT) and the estimated permeability (PERMS) due to regression analysis using function (14). The

permeability values show strong similarity, the model distance calculated by equation (15) is 3.2%. Permeability stands in strong correlation with the Stoneley-index, since the value of rank correlation using equation (16) is 0.99. The regression model approximates well the known permeability values.

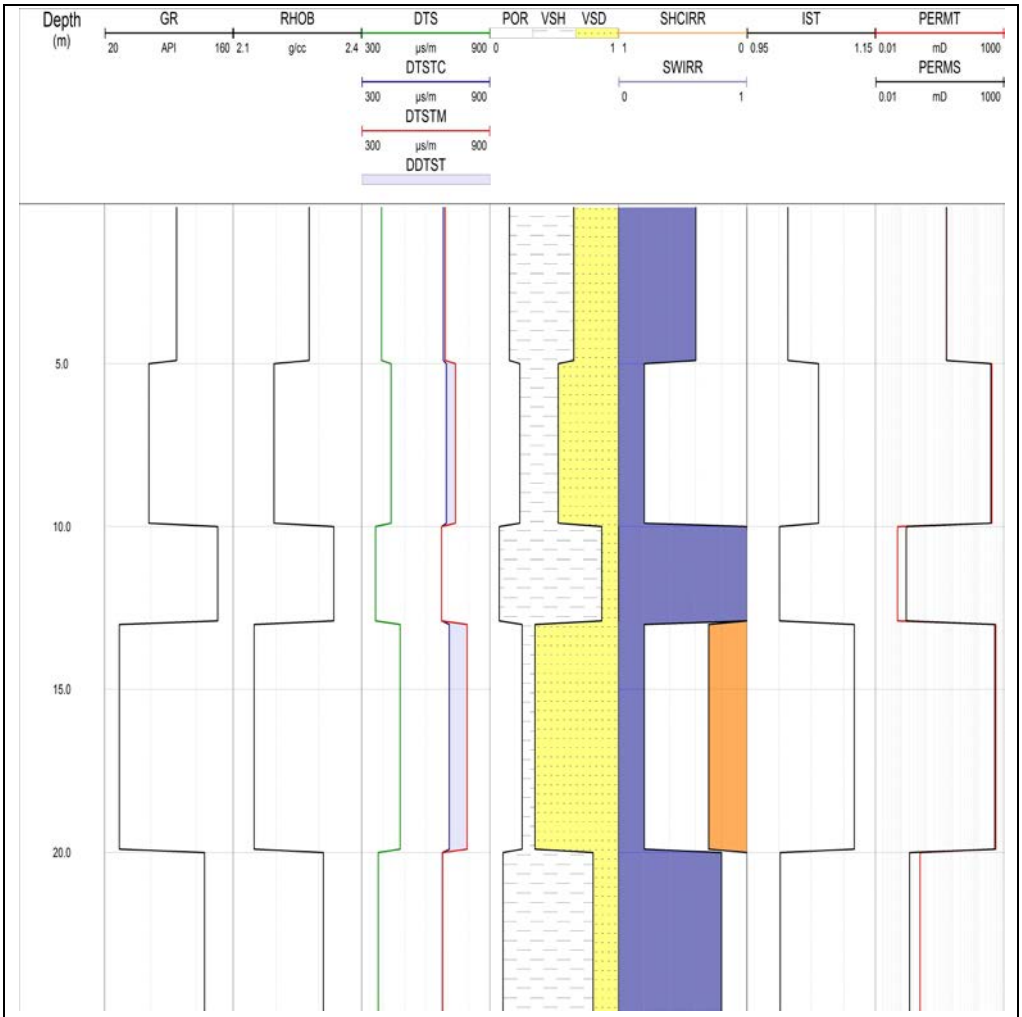

Figure 4

Synthetic well logs and result of permeabililty estimation (Model-I)

7. Test on inhomogeneous model

In real formations the petrophysical parameters can vary within the layers, hence the depth dependence of petrophysical parameters were approximated with eighteenth to twenty-second degree polynomials (Model-II). Synthetic data were calculated on the inhomogeneous model to which various degrees of Gaussian noise were added. In the case of 2% noise the model equation (14) has proved to be valid (Figure 5), where $a = 8.78$, $b = 48.22$, $c = 1.63$.

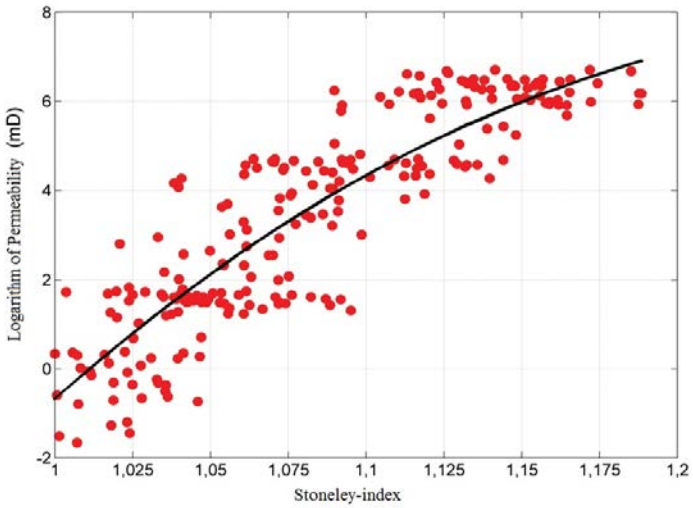

Figure 5

Natural logarithm of permeability versus Stoneley-index (Model-II)

The result of permeability estimation can be seen in Figure 6. The permeability log can be estimated with an error that is proportional to the data noise. If the noise is 2%, the distance between the exact and measured permeability logs is 6.9%, although the rank correlation coefficient indicates a close relationship ($R = 0.98$).

It can be seen that in inhomogenous petrophysical model even a slight error may cause a significant estimation error. Therefore, noise sensitivity of the model was further examined. The noiseless (synthetic) data set of the inhomogenous model was loaded with different amount of Gaussian-noise (1–5%). Besides the variation of noise, the variace of three grading parameters (model distance, rank correlation, linear correlation) were observed.

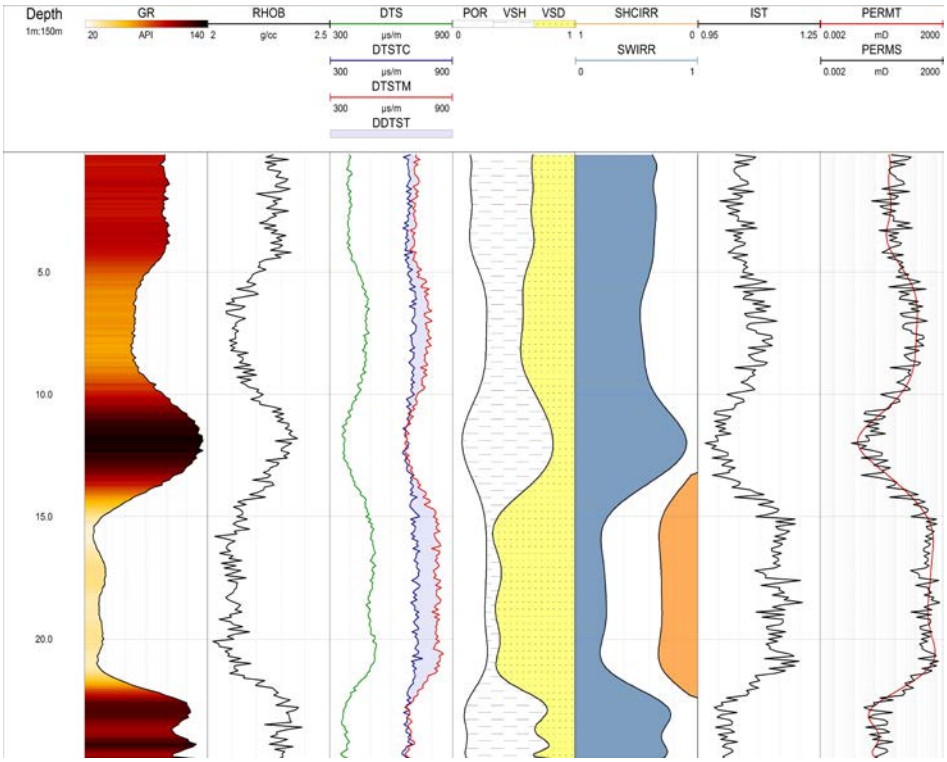

Figure 6

Synthetic well logs and result of permeabililty estimation (Model-II)

In Table 3 the result of data processing is shown, which includes the values of the regression coefficients related to formula (14). The rank correlation coefficient shows a strong relationship even at the highest noise level, although the degree of linear correlation decreases rapidly. The model distance at 5% noise level is four times higher than its initial value. The order and the sign of coefficients do not change significantly. It can be stated that the exponential model is valid in case of noisy data, however noise significantly affects the reliability of estimation. This phenomenon can be observed in the case of linear approximation, too. That is the reason, why we made an attempt for the improvement of this method with the suggestion of the non-linear model. The noise sensitivity is inherent for other well log methods, too. It may have a significant influence on the accuracy of permeability estimation.

Table 3

Regression coefficients estimated for noisy data sets and inhomogeneous model

Noise level [%]	D_m [%]	R	r	a	b	c
1	3.67	0.99	0.97	9.08	61.51	1.79
2	6.86	0.98	0.90	8.77	48.08	1.63
3	9.83	0.98	0.78	9.17	25.28	1.08
4	11.86	0.98	0.66	7.85	17.15	1.00
5	12.09	0.96	0.65	7.90	16.00	0.94

8. Case study

The Stoneley-index vs. permeability relationship can be applied to field data. For this purpose, the data set in Buffin's article (1996) was used, which allowed the validation of the estimated permeability log. The investigated borehole (Katnook-3) was drilled in a hydrocarbon-field of South-Australia (Figure 7). The Otway-basin, including the studied well-site was formed as a result of rifting between the Antarctic and Australian plates. It is approximately 500 km long, west to northwest trending. This area occurs along the southern coast of Australia, and comprises a series of Jurassic and Cretaceous basins with a

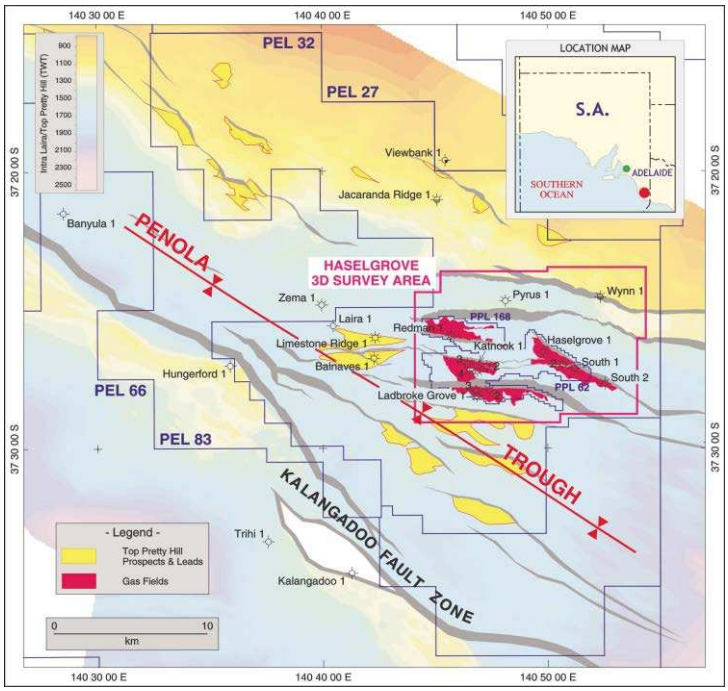

Figure 7

Location map of the South-Australian hydrocarbon field (Boult and Donley 2001)

Tertiary cover. Several hydrocarbon reservoir structures can be found in Otway-basin, which exhibit high porosity and permeability in general. The early Cretaceous Pretty Hill Formation is characterized by frequent facies changes, which consist of fine- to coarse-grained sandstone and other mineral components. The main producing gas reservoir in the Otway-basin is the Pretty Hill Formation. Its porosity is often over 25%, permeabilities in excess of 1000 mD, and has flowed over 451,000 m^3 gas per day on test in the Katnook field.

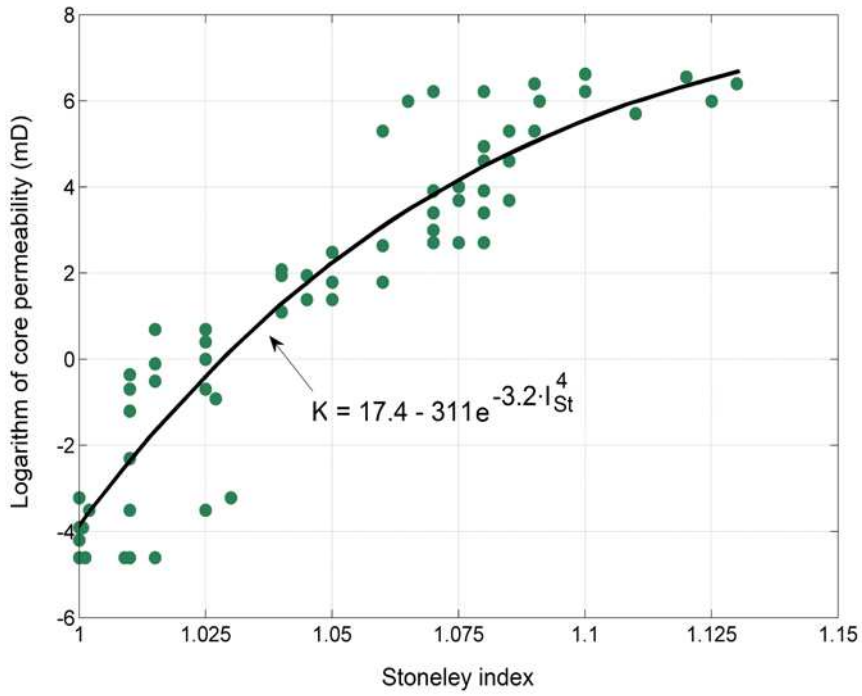

Figure 8

Regression relationship between core permeability and Stoneley-index in Katnook-3

The components of acoustic waveform were available in the form of well logs (DTS, DTSTC, DTSTM). Then the Stoneley-index (IST) was calculated using equations (8) and (9). In order to determine the regression function the Stoneley-index was compared to permeability values measured on core samples (Figure 8). As a result, the parameters of equation (14) regression function are $a = 17.4$, $b = 311$, $c = 3.2$. The rank correlation value is 0.98, which shows a very close connection between the Stoneley-index and core permeability (the value of linear correlation is $r = 0.78$).

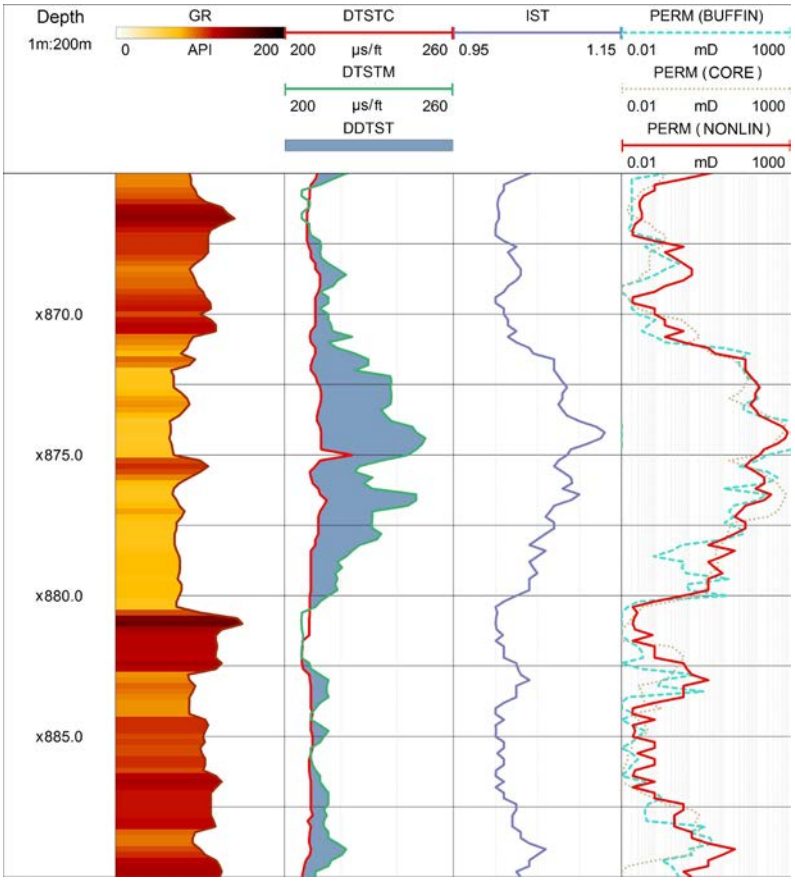

Figure 9

Input well logs and result of permeability estimation in Katnook-3

The processed borehole logs and the permeability logs estimated from Stoneley-index are shown in Figure 9, where PERM (CORE) represents the core permeability, PERM (BUFFIN) represents the permeability resulted by the (linear) model of BUFFIN (1996), and PERM (NONLIN) represents permeability due to our non-linear approximation. The core data were quite frequently available (sometimes 0.2 m). The model distance between the values estimated with the non-linear method and the laboratory measured permeability values was 7%. The model distance between the linear result of Buffin and the measured values on the core is 10.1%. The non-linear approximation provides ~30% relative improvement compared to the core data. The misfit in some intervals can be caused by rapid changes of borehole caliper, which is not taken into account by the model. Comparing this field case to the inhomogeneous synthetic test it can be seen that the dispersion of data around the regression model is smaller than in the previous case. The synthetic modeling

experiments show consistent results with those of the case study, which confirms that the suggested statistical method can be used advantageously to evaluate permeability in hydrocarbon formations.

9. Conclusions

In this study the possibility of permeability estimation from nuclear and acoustic logs is shown. Both the synthetic model analysis and the field application confirm that permeability can be derived based on Stoneley-wave arrival times with the statistical (approximate) method. The advantage of this method contrary to core measurements is its quickness and it is a direct method providing continuous (in-situ) information along the whole logging interval. The vertical resolution of this method depends on the length of the applied sonde that is usually 2 ft (0.6 m), in case of normal acoustic tools. The suggested method is a further development of a statistical method known from the literature, which assumes nonlinear relationship between Stoneley-index and permeability. In this case, the correlation coefficient value is bigger, than in case of conventional linear relationship. The field results confirm this close relation, too. The non-linear relationship is especially true in the range of small permeabilities. Therefore, with this method, the reservoirs with poor permeability can be characterized more accurately. The disadvantage of the suggested method is its noise sensitivity. Hence, the appropriate preparation of well logs and data processing is essential. To correct noise sensitivity we offer robust and resistant regression methods that are independent of the probability distribution of data and provide real estimate even in the case of having outliers in the data set. To solve this problem the iterative most frequent value method of STEINER (1997) can be applied effectively. Moreover, this method can be the base for calculation of permeability with inverse modeling. The nonlinear regression equation can be regarded as a theoretical probe response function, which forms a connection between permability and the measured Stoneley-slowness in the permeable layer. In that case, when the regression coefficients are known, the Stoneley-slowness data can be calculated with this equation in the permeable layer. During the iterative inversion procedure, permeability may be varied until the deviation between the measured and calculated Stoneley-curves becomes minimal. Before trying this method, the validity of non-linear response equation has to be certified in several well-sites and the sensitivity to permeability of the model equation have to be studied. These types of analyses will show whethe permeability be used as an inversion unknown or may reveal the problem of ambiguity.

10. Acknowledgement

The research was supported by the Hungarian Scientific Research Found (project number PD 109408). The first author thanks the support of the János Bolyai Research Fellowship of the Hungarian Academy of Sciences. The authors express their thanks to the research collective of the Geophysical Department (University of Miskolc), as well as to Peter Boult (GINKO ENP GNG) for the licence presenting the Australian data set.

11.List of symbols

Symbol	Description	Unit
a, b, c	Regression coefficients	–
B	Bulk modulus of dry rock	Pa
B^*	Complex bulk modulus of drilling mud	Pa
B_c	Bulk modulus of saturated formation	Pa
B_f	Bulk modulus of pore fluid	Pa
B_m	Bulk modulus of drilling mud	Pa
B_s	Bulk modulus of rock matrix	Pa
C_0, C	Diffusion coefficient	m^2s^{-1}
D_m	Model distance (RMSE)	%
GR	Natural gamma-ray intensity	API
GR_{sd}	Natural gamma-ray intensity of sand	API
GR_{sh}	Natural gamma-ray intensity of shale	API
I_{St}, IST	Stoneley-index	–
K	Permeability in Darcy's equation	m^2
N	Number of depth points along the borehole	–
p	Pore pressure	Pa
r	Pearson's correlation coefficient	–
R	Spearman's (rank) correlation coefficient	–
PERM	Permeability estimated from well logs	mD
S_{x0}	Water saturation in flushed zone	v/v
$S_{w,irr}$, SWIRR	Irreducible water saturation	v/v
SHCIRR	Irreducible hydrocarbon saturation	v/v
t	Time	s
u	Relative displacement vector	m
v_m	Sonic wave velocity in drilling mud	ms^{-1}
v_{St}	Stoneley-wave velocity	ms^{-1}
V_{sh}, VSH	Shale volume	v/v
V_{sh}, VSD	Sand volume	v/v
α	Elasticity	–
δ	Difference between ranks of data pairs	–
Δt_{hc}	Sonic interval transit time of hydrocarbon	μsm^{-1}
Δt_{mf}	Sonic interval transit time of mudfiltrate	μsm^{-1}
Δt_s, DTS	Shear-wave interval transit time	μsm^{-1}
Δt_{sd}	Sonic interval transit time of sand	μsm^{-1}
Δt_{sh}	Sonic interval transit time of shale	μsm^{-1}
Δt_{St}, DTST	Stoneley interval transit time	μsm^{-1}
η	Viscosity	Pa·s
κ	Scaling parameter	–
μ	Shear modulus	Pa
ρ_b, RHOB	Bulk density of formation	gcm^{-3}
ρ_{hc}	Density of hydrocarbon	gcm^{-3}
ρ_m	Density of drilling mud	gcm^{-3}
ρ_{mf}	Density of mudfiltrate	gcm^{-3}
ρ_{sd}	Density of sand	gcm^{-3}

ρ_{sh}	Density of shale	gcm^{-3}
Φ, POR	Porosity	v/v
ω	Angular frequency of compression wave	Hz

12. References

[1] BADRI, M.–SOUSA, S.–KLIMENTOS, T.: *Shear anisotropy applications in production optimization*, Western Desert, Egypt. SEG Annual Meeting, 2000, Paper 2000–1695, 1–4.

[2] BALA, M. J.: Can we determine permeability with the Stoneley wave slowness from acoustic full waveform. *EAGE Proceedings*, 2010, 1–5.

[3] BIOT, M. A.: Theory of propagation of elastic waves in a fluid-saturated porous solid. I. Low-frequency range. J. *Acoust. Soc. Am.*, 1955, Vol. 28, No. 2, 168–178.

[4] BIOT, M. A.: Mechanics of deformation and acoustic propagation in porous media. *J. Appl. Phys.*, 1962, 33, 1482–1498.

[5] BOULT, P. J.–DONLEY J.: Volumetric calculations using 3D seismic calibrated against porosity logs - Pretty Hill formation reservoirs, Onshore Otway Basin. *PESA Eastern Australasian Basins Symposium*, 2001, 425–433.

[6] BRIE, A.–ENDO, T.–JOHNSON, D. L.–PAMPURI, F.: Quantitative formation permeability evaluation from Stoneley waves. *SPE Reservoir Eval. & Eng.*, 2000, Vol. 3, No. 2, 109–117.

[7] BUFFIN A.: Permeability from waveform sonic data in the Otway Basin. *SPWLA 37th Annual Logging Symposium*, 1996, 16–19. June , 1–5.

[8] CHANG, S. K.–LIU, H. L.–JOHNSON D. L.: Low-frequency tube wave in permeable rocks. *Geophysics*, 1988, Vol. 53, No. 4, 519–527.

[9] COATES, R.–XIAO, L.–PRAMMER, M. G.: *NMR logging principles and applications*. Halliburton, 1999, Houston.

[10] DARCY, H.: Determination of the laws of flow of water through sand. In: *Physical Hydrogeology*, R. A. Freeze et W. Black (eds) Benchmark Papers in Geology, Hutchinson-Ross, 1983, Vol. 72, 8–20.

[11] ELLIS, D. V.–SINGER, J. M.: *Well logging for earth scientists*, 2nd Edition, Springer, 2007, 533–562.

[12] HALDORSEN, J. B. U.–JOHNSON, D. L.–PLONa, T.–SINHA, B.–VALERO, H. P.–WINKLER, K.: *Borehole acoustic waves*. Ridgefield, Connecticut, USA. Oilfield Review 2006, 34–43

[13] LARIONOV, V. V.: *Radiometry of Boreholes*. NEDRA, Moscow, 1969.

[14] LIU, H. L.: Borehole modes in a cylindrical fluid-saturated permeable medium. *J. Acoust. Soc. Am.*, 1988, Vol. 84, 424–431.

[15] MATHIEU, F.–TOKSOZ, M. N.: Determination of fracture permeability using acoustic logs. *S.A.I.D. Ninth Int. Formation Evaluation Trans.*, 1984, paper 47.

[16] NORRIS, A. N.: Stoneley-wave attenuation and dispersion in permeable formations. *Geophysics*, 1989, Vol. 54, No. 3, 330–341.

[17] RAYMER, L. L.–HUNT, E. R.–GARDNER, J. S.: An improved sonic transit time-to-porosity transform. *SPWLA 21st Annual Logging Symposium*, 1980, Paper 1980-P, 1–13.

[18] ROSENBAUM, J. H.: Synthetic Microseizmograms: Logging in porous formation. *Geophysics*, 1974, Vol. 39, 14–32.

[19] SCHMITT, D. P.–BOUCHON, M.–BONNET, G.: Full-waveform synthetic acoustic logs in radially semi-infinite-saturated porous media. *Geophysics*, 1988, Vol. 53, 807–823.
[20] SPEARMAN C.: The proof and measurement of association between two things. *The American Journal of Psychology*, 1904, Vol. 15, No. 1, 72–101.
[21] STEINER F. (ed.): *Optimum methods in statistics*. Academic Press, Budapest, 1997.
[22] TANG, X. M.–CHENG, C. H.–TOKSÖZ, M. N.: Dynamic permeability and borehole Stoneley waves: A simplified Biot-Rosenbaum model, J. *Acoust. Soc. Am.*, 1990, Vol. 90, 1632–1646.
[23] TANG, X. M.–CHENG, C. H.–TOKSÖZ, M. N.: Stoneley wave propagation in a fluid filled borehole with a vertical fracture. *Geophysics*, 1991, Vol. 56, 447–460.
[24] TANG, X. M.–CHENG, C. H.: Fast inversion of formation permeability from Stoneley wave logs using a simplified Biot-Rosenbaum model. Earth Resources Laboratory Industry Consortia Annual Report 1994–08, 209–226.
[25] TIMUR, A.: An investigation of permeability, porosity, and residual water saturation relationships. *SPWLA 9th Annual Logging Symposium*, 1968, 1–18.
[26] WHITE, J. E.: *Underground sound: Application of seismic waves*. Amsterdam; New York: Elsevier, 1983, 239–245.
[27] WILLIAMS, D. M.–ZEMANEK, J.–ARIGONA, F. A.–DENNIS, C. L.–CALDWELL, R. L.: The long spaced acoustic logging tool. Annual Logging Symposium, New Orleans, 1984.
[28] WINKLER, K. W.–LIU, H. L.–JOHNSON, D. L.: Permeability and borehole Stoneley waves: Comparison between experiment and theory. *Geophysics*, 1989, Vol. 54, No. 1, 66–75.

Geosciences and Engineering, Vol. 2, No. 4 (2013), pp 47–58.

MODELLING THE PRESSURE DEPENDENCE OF P WAVE VELOCITY AND POROSITY ON SANDSTONES

JUDIT SOMOGYI MOLNÁR[1,2]–ANETT KISS[1]

[1]*Department of Geophysics, University of Miskolc*
[2]*MTA–ME Research Group of Geoengineering*

1. Abstract

Acoustic velocity in rocks strongly depends on pressure which influences the mechanical, transport and elastic properties of rocks such as porosity and elastic moduli. Therefore a quantitative model – which provides the physical explanation – of the mechanism of pressure dependence is required. In this paper a petrophysical model is presented which provides the connection between the propagation velocity of longitudinal wave and rock pressure. Since porosity is an important parameter in the exploitation of hydrocarbons we developed also a model describing that of pressure dependence. The proposed models are based on the idea that microcracks in a rock in unit volume are closing with increasing pressure thus increasing velocity, decreasing secondary porosity and as a result decreasing total porosity can be measured. The models were applied to laboratory measured acoustic P wave velocity and porosity data sets as function of pressure – published in literature – and they were inverted to prove the applicability of the model and to obtain that of parameters. The quality checked inversion results showed that the calculated data matched accurately with measured data and also proved that the suggested petrophysical models perform well in practice.

2. Introduction

Due to the increasing demand for hydrocarbons and the depletion of the known hydrocarbon fields there is a growing claim to predict rock physical parameters more accurate at non-conventional conditions also. Geophysics has a wide palette to determine the required properties, for example acoustic velocity, porosity, permeability, elastic moduli and it is well known that pressure has a strong influence on them. To interpret seismic, acoustic well logging data and to relate laboratory measurement to in-situ parameters properly it is necessary to understand what the effects of pressure are to them. Therefore the investigation of pressure dependence of propagation wave velocity in rocks is in focus of researchers. Beside others WYLLIE et al. [1], STACEY [2], SENGUN et al. [3] published their results of measuring acoustic velocity under different load in laboratory. NUR and SIMMONS [4], YU et al. [5], HE and SCHMITT [6] used a test system with varying pore pressure. EBERHART-PHILLIPS et al. [7] tried to predict the P wave velocity based on only three parameters: porosity (Φ_t), shale content (C) and effective pressure (P_e) as

$$\alpha = 5{,}77 - 6{,}94\Phi_t - 1{,}73\sqrt{C} + 0{,}466(P_e - \exp(-16{,}7P_e)) \quad (1)$$

They applied forward stepwise multiple regressions on measurement data sets to find the best-fitting empirical relationship. The phenomenon that the observable wave velocity is increasing because of increasing pressure is well-known and was explained in various

rock mechanical studies [5] [8] [9]. Such as that pore volume reduces with increasing pressure, thus increasing velocity can be measured [8]. One of the most frequently used mechanisms for explaining the phenomenon is based on the closure of microcracks in rocks under the change of pressure [3] [10].

General observation is that the relationship between velocity and pressure is nonlinear in the beginning phase of loading [5] [10] and often can be described with exponential function. In the literature several qualitative models are available [8] [11] [12] [13] to describe the pressure dependence of acoustic wave velocity but these empirical models do not explain the physical meaning of the process, they only give the regression function of the curve fitted to the measured data. To reasonably interpret laboratory measurements quantitative models – which provide the physical explanation of the mechanism of pressure dependence – are required. In this paper we introduce new petrophysical models describing the pressure dependence of acoustic velocity and porosity.

3. The pressure dependent velocity model

The response of rocks to stress depends on their microstructure, constituent minerals and porosity, which is manifested in pressure dependence of velocity of elastic waves. Following WALSH and BRACE [11] we assume that the main factor determining the stress dependence of the propagation velocity of P wave is the closure of microcracks. For this reason we introduce the parameter N as the number of microcracks in rocks in unit volume. The model is restricted only for uniaxial stress state. If a stress increase $d\sigma$ is created in a rock let us assume that the change in the number of microcracks dN is directly proportional to the applied stress increase $d\sigma$. One can describe the two assumptions with the following differential equation

$$dN = -\lambda N d\sigma , \tag{2}$$

where λ is new material quality dependent petrophysical parameter. The negative sign represents that with increasing stress the number of microcracks decreases. The solution of the upper equation is

$$N = N_0 \exp(-\lambda\sigma) , \tag{3}$$

where N_0 is the number of microcracks related to secondary porosity at stress-free state ($\sigma = 0$). We assume also a linear relationship between the infinitesimal change of the propagation P wave velocity $d\alpha$ and dN

$$d\alpha = -\kappa dN , \tag{4}$$

where κ is a proportionality factor, a new material characteristic. The negative sign represents that the velocity is increasing with decreasing number of microcracks. Combining this assumption with Eqs. (2-3) we obtain

$$d\alpha = \kappa\lambda N_0 \exp(-\lambda\sigma)\, d\sigma . \tag{5}$$

Solving the differential equation one can obtain

$$\alpha = K - \kappa N_0 \exp(-\lambda\sigma), \tag{6}$$

where K is an integration constant. At stress-free state ($\sigma = 0$) the propagation velocity α_0 can be measured and K can be computed from Eq. (6) as $\alpha_0 = K - \kappa N_0$. With this result and introducing the notation $\Delta\alpha_0 = \kappa N_0$ Eq. (6) can be rewritten in the following form

$$\alpha = \alpha_0 + \Delta\alpha_0 (1 - \exp(-\lambda\sigma)). \tag{7}$$

Eq. (7) provides a theoretical connection between the P wave velocity and rock pressure. In the framework of the model, the velocity of acoustic wave increases from α_0 (at zero pressure) to $\alpha_{max} = \alpha_0 + \Delta\alpha_0$ (at high pressure, when all microcracks are closed). So, $\Delta\alpha_0$ can be considered the velocity-drop caused by the presence of microcracks at zero pressure [13]. Note that in the range of high pressures, reaching a critical pressure the reversible range is exceeded and destruction of the sample may occur thus decreasing velocity can be observed. This effect is outside of our present investigations. Therefore this model is valid only in the reversible range. As it was mentioned λ is a new petrophysical constant, of which physical meaning is necessary to be given. Introducing the notation $\Delta\alpha = \alpha_{max} - \alpha$, (the velocity-drop caused by the presence of microcracks at pressure σ Eq. (7) can be written in the form

$$\Delta\alpha = \Delta\alpha_0 \exp(-\lambda\sigma). \tag{8}$$

Experiences denote that rocks show different velocity response to the same change in the rock pressure or in other words the velocity shows different sensitivity to pressure. Sensitivity functions are extensively used in the seismic, geoelectric, electromagnetic and well-logging literature. Hence we introduce the (logarithmic) stress sensitivity of the velocity-drop $\Delta\alpha = \alpha_{max} - \alpha$ as

$$S(\sigma) = -\frac{1}{\Delta\alpha}\frac{d\Delta\alpha}{d\sigma} = -\frac{d\ln(\Delta\alpha)}{d\sigma}. \tag{9}$$

By using Eq. (8) it can be seen that

$$\lambda = -\frac{d\ln(\Delta\alpha)}{d\sigma} = S, \tag{10}$$

which shows that the petrophysical characteristic λ is the logarithmic stress sensitivity of the velocity-drop [14] [15].

4. The pressure dependence of porosity

Stress-dependent porosity has been widely studied at laboratory scale [12] [16] [17] [18], as it can significantly affect reserve estimates, well production rate and profitability. HAN and DUSSEAULT [19] found relationship among compressibility and total porosity change

$$d\Phi_t = -C_{bc}(1 - \Phi_t)d\sigma', \tag{11}$$

where C_{bc} is the effective bulk compressibility, Φ_t is the total porosity, σ' is the difference between total stress and pore pressure. The effective bulk compressibility is the sum of the pseudo-bulk and the matrix compressibility. It is well known that the total porosity (Φ_t) of a rock consists of the primary (Φ_1) and secondary porosity (Φ_2)

$$\Phi_t = \Phi_1 + \Phi_2. \tag{12}$$

The former one is related to the pores originated in diagenesis, while the latter one is connected to the microcracks in the rock.

Similarly to the velocity model we assume that microcracks related to the secondary porosity are closed with loading. Following the same analogy used at the velocity model, it is obvious that if we increase the stress the porosity Φ_2 is decreasing (microcracks are closing), i.e.

$$d\Phi_2 = -\lambda\Phi_2 d\sigma, \tag{13}$$

where λ is the same material quality dependent petrophysical parameter used at the velocity model. Solving the differential equation one can obtain

$$\Phi_2 = \Phi_2^{(0)}\exp(-\lambda\sigma), \tag{14}$$

where $\Phi_2^{(0)}$ is the secondary porosity at stress free state. With Eq. (14) the total porosity can be written as

$$\Phi_t = \Phi_1 + \Phi_2^{(0)}\exp(-\lambda\sigma), \tag{15}$$

which describes that of pressure dependence. This model equation shows that the total porosity should tend to a limit value which is the primary porosity.

5. Description of the samples

To confirm the reliability of the model velocity and porosity data sets published by GOMEZ et al. [20] were processed. The pulse transmission technique [21] was used for P wave velocity measurements at 1 MHz frequency. During measurements - performed at dry conditions - the P transducers and receivers were matched to the end caps of the samples

and the travel time was measured (Figure 1). The velocity can be calculated easily from the sample length and the travel time. The error of the velocity measurements was around 1 % [20]. We tested our model on four different sandstone samples: Sample marked A11, A117, A82 and F410 respectively. Table 1 contains the main features of the samples.

Table 1

Properties of the samples. Data obtained from GOMEZ et al. [20]

Sample	**Type**	**Porosity (%)**	**Permeability (mD)**
A11	Oligocene Fontainebleau sandstone	7	10
A117	Oligocene Fontainebleau sandstone	11	103
A82	Oligocene Fontainebleau sandstone	8	7
F410	Oligocene Fontainebleau sandstone	6	1

The measured velocity and porosity versus uniaxial pressure of the described samples are shown in Figure 2. Measurement data indicate that the velocity increases first strongly nonlinearly with increasing pressure (because the quantity of microcracks are relatively high in this region) then in the higher pressure domain the increase in velocity (with increasing pressure) is moderate which can be attributed to the decrease of microcracks in the rock sample. It can be seen that the decrease of total porosity is tend to a limit value. We suppose that this limit is the primary porosity which is not closed during loading.

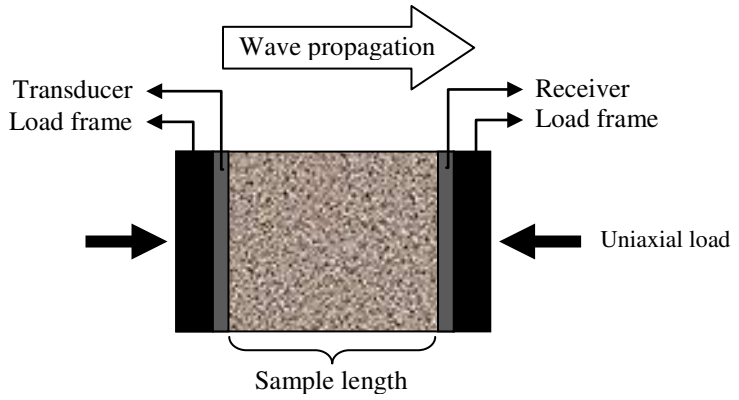

Figure 1
Illustration of the pulse transmission technique

6. Case studies

Proving the validity and applicability of the introduced velocity model, we present the interpretation of measurement data of the described samples. The 5 model parameters ($\alpha_0, \Delta\alpha_0, \lambda, \Phi_1, \Phi_2^{(0)}$) can be determined by processing measurement data based on the method of geophysical inversion. Since λ is a common parameter a joint inversion process was used. The relevant data sets contained relatively low amount of noise and the problem was overdetermined, thus the Gaussian Least Squares Method was used. The inversion results for each sample can be seen in Table 2. For the characterization of the accuracy of inversion estimates, the estimation errors of individual inversion parameters are also provided within the brackets. Errors were calculated by using the method given by MENKE [22]. According to the method the elements of the main diagonal of covariance matrix in parameter space ($cov(m)$) provide the variances (σ_m) of model parameters, that means

$$\sigma_{m_i} = \sqrt{\mathrm{cov}(\mathbf{m})_{ii}} \tag{16}$$

gives the estimated error of the i-th model parameter (i = 1,2,3,4,5 in the given problem).

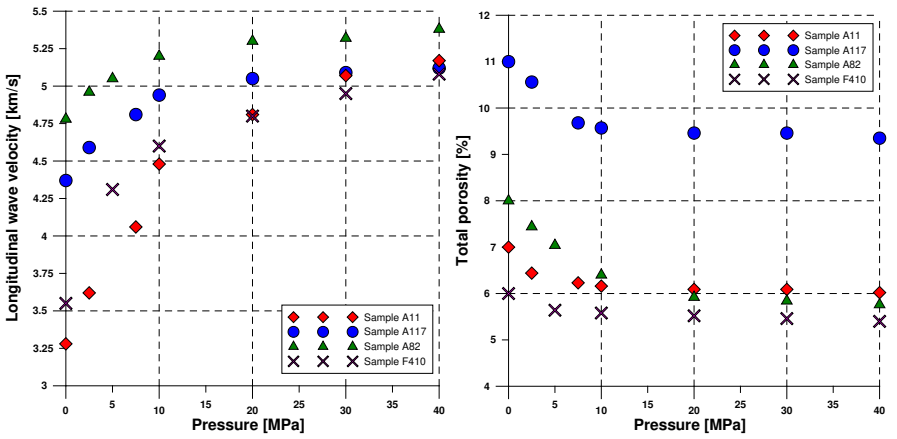

Figure 2
Pressure dependence of P wave velocity and porosity.
Data obtained from GOMEZ et al. [20]

Table 2

Model parameters with estimation errors by linearized inversion

Sample	α_0 **(km/s)**	$\Delta\alpha_0$ **(km/s)**	λ **(1/MPa)**	Φ_1 **(%)**	$\Phi_2^{(0)}$ **(%)**
A11	3,21 (±0,07)	1,93 (±0,09)	0,096 (±0,013)	5,95 (±0,08)	0,83 (±0,14)
A117	4,34 (±0,04)	0,73 (±0,05)	0,184 (±0,022)	9,38 (±0,05)	1,67 (±0,09)
A82	4,79 (±0,02)	0,57 (±0,02)	0,119 (±0,004)	5,75 (±0,02)	2,27 (±0,03)
F410	3,57 (±0,06)	1,43 (±0,07)	0,133 (±0,015)	5,43 (±0,03)	0,54 (±0,07)

With the estimated parameters, the velocities and porosities can be calculated at any pressure by substituting them into the model equations [Eq. (7)/(15)]. The results are shown in Figure 3–6. The solid lines show the calculated velocity/porosity-pressure functions while symbols represent the measured data. One can see that the calculated curves fit well to the measured data which confirms the applicability of the physical models in practice.

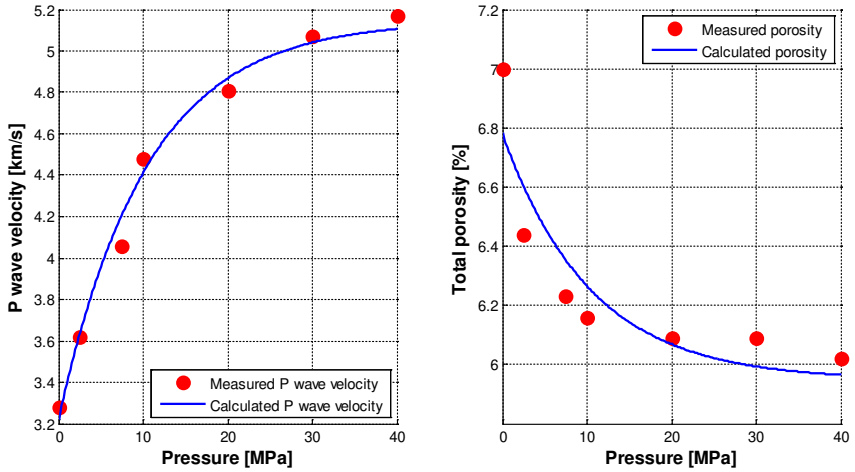

Figure 3
P wave velocity and total porosity vs. uniaxial pressure of Sample A11. Measured data obtained from GOMEZ et al. [20]

For the characterization of the accuracy of inversion estimates the RMS (Root Mean Square) value was calculated according to the following formula [22]

$$D = \sqrt{\frac{1}{N_d - 1}\sum_{k=1}^{N_d}\left(d_k^{(m)} - d_k^{(c)}\right)^2}\ 100[\%], \tag{17}$$

where N_d is the number of measured points, $d_k^{(m)}$ is the measured velocity/porosity at the k–th pressure and $d_k^{(c)}$ is the k–th calculated velocity/porosity data which can be computed by Eq. (7)/(15).

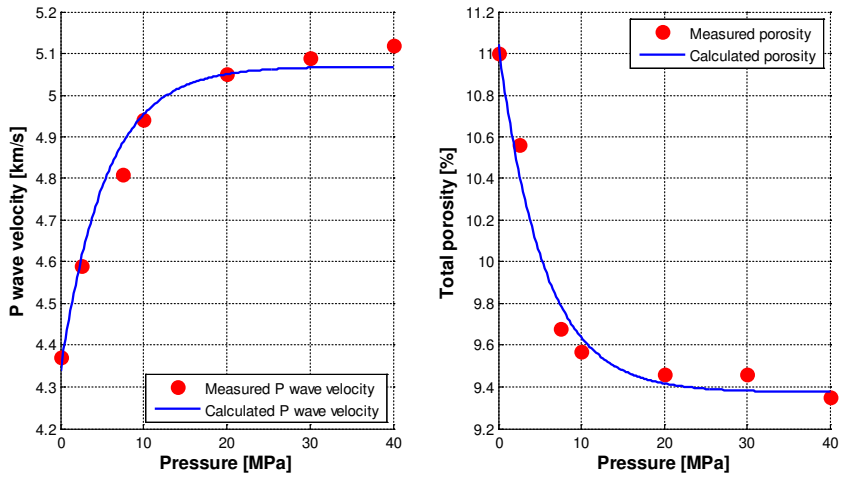

Figure 4

P wave velocity and total porosity vs. uniaxial pressure of Sample A117. Measured data obtained from GOMEZ et al. [20]

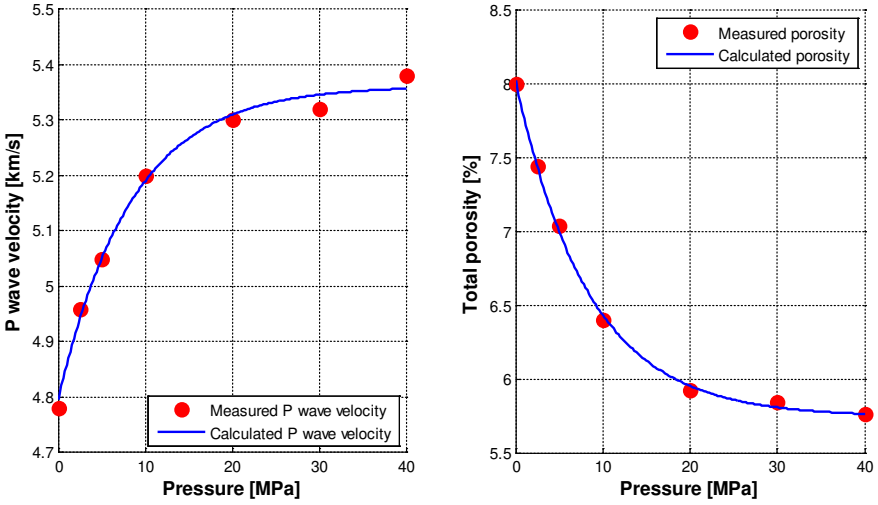

Figure 5

P wave velocity and total porosity vs. uniaxial pressure of Sample A82. Measured data obtained from GOMEZ et al. [20]

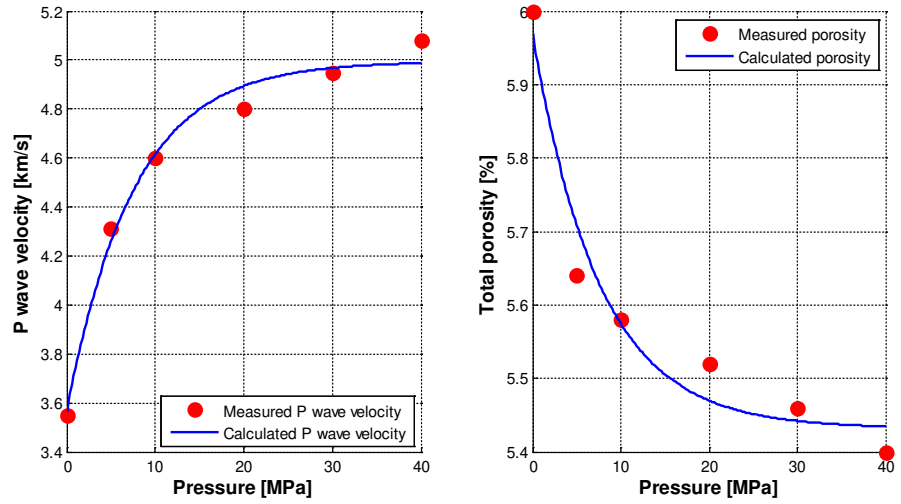

Figure 6

P wave velocity and total porosity vs. uniaxial pressure of Sample F410.

Measured data obtained from GOMEZ et al. [20]

To characterize the reliability of the suggested petrophysical models the mean spread [22] was also calculated by

$$S^{AVG} = \sqrt{\frac{1}{M(M-1)} \sum_{i=1}^{M} \sum_{j=1}^{M} \left(corr(m)_{ij} - \delta_{ij}\right)^2} , \tag{18}$$

where δ is a Kronecker-delta symbol (which equals 1 if $i = j$, otherwise 0), M is the number of model parameters and *corr(m)* is the correlation matrix. Table 3 contains the calculated RMS and mean spread values for each sample in the last iteration step.

Table 3

RMS and mean spread values

	A11	A117	A82	F410
D (%)	1,88	1,82	0,38	1,0
S^{AVG}	0,37	0,38	0,39	0,36

It can be seen that the data misfits (RMS) were small and the mean spread values indicate that the parameters are in low-moderate correlation, but the inversion results are

still reliable. These results confirm the accuracy of the inversion estimates and the feasibility of the developed petrophysical models.

7. Conclusion

In this paper based on Walsh and Brace's theory, petrophysical models for calculating stress-dependent P wave velocity and porosity were developed. The advantage of the models is that they are not based on simple curve fitting, but give physical explanation for the process with three-parameter exponential equations. For the longitudinal velocity it states $\alpha = \alpha_0 + \Delta\alpha_0 (1-\exp(-\lambda\sigma))$. α_0 is the velocity at zero pressure, $\Delta\alpha_0$ is the velocity drop caused by the presence of microcracks and λ is a new petrophysical parameter. The pressure dependence of porosity can be described by the equation $\Phi_t = \Phi_1 + \Phi_2^{(0)}\exp(-\lambda\sigma)$, where Φ_t is the total, Φ_1 is the primary, $\Phi_2^{(0)}$ is the secondary porosity at stress-free state, λ is the same petrophysical constant as in the velocity model. Acoustic velocity and porosity measurement data of sandstone samples (chosen from the literature) were used to confirm the reliability of the model. By means of inversion-based processing the model parameters were determined from measurement data. Calculated data could be produced by using the petrophysical model. A very good correlation between measured and calculated data was found thus inversion results confirmed the accuracy and feasibility of the petrophysical models.

8. Acknowledgement

The research of Judit Somogyi Molnár was supported by the European Union and the State of Hungary, co-financed by the European Social Fund in the framework of TÁMOP 4.2.4.A/2-11-1-2012-0001 'National Excellence Program'. The research of Anett Kiss was carried out in the framework of the Sustainable Resource Management Center of Excellence at the University of Miskolc, as part of the TÁMOP-4.2.2/A-11/1-KONV-2012-0049 „WELL aHEAD" project in the framework of the New Széchenyi Plan, funded by the European Union, co-financed by the European Social Fund.

9. List of symbols

Symbol	Description	Unit
C	shale content	–
C_{bc}	effective bulk compressibility	1/MPa
corr(m)	correlation matrix	–
cov(m)	covariance matrix in parameter space	–
D	Root Mean Square (RMS)	%
$d_k^{(c)}$	calculated velocity/porosity at the k-th pressure value	kms^{-1},%
$d_k^{(m)}$	measured velocity/porosity at the k-th pressure value	kms^{-1},%
dα	change of propagation P wave velocity	km/s
dN	change in the number of microcracks (per unit volume)	–
dσ	stress increase	MPa
$d\Phi_2$	change in the secondary porosity	%
K	integration constant	–

Symbol	Description	Unit
M	number of model parameters	–
N	number of microcracks in unit volume	–
N_d	number of measured points	–
N_0	number of microcracks at stress-free state	–
P_e	effective pressure	MPa
S^{AVG}	mean spread	–
$S(\sigma)$	stress sensitivity of velocity-drop	1/MPa
α	longitudinal (P) wave velocity	km/s
α_0	longitudinal (P) wave velocity at stress-free state	km/s
α_{max}	longitudinal (P) wave velocity at maximum pressure	km/s
δ	Kronecker-delta symbol	–
$\Delta\alpha$	velocity-drop at pressure σ	km/s
$\Delta\alpha_0$	velocity-drop	km/s
$\Delta\Phi_t$	total porosity change	%
κ	proportionality factor	km/s
λ	new material quality dependent petrophysical parameter	1/MPa
σ	stress	MPa
σ'	difference between total stress and pore pressure	MPa
σ_m	estimated error of the i-th model parameter	–
Φ_t	total porosity	%
Φ_1	primary porosity	%
Φ_2	secondary porosity	%
$\Phi_2^{(0)}$	secondary porosity at stress-free state	%

10. References

[1] WYLLIE, M. R. J.–GREGORY, A. R.–GARDNER, G. H. F.: An experimental investigation of factors affecting elastic wave velocities in porous media. *Geophysics*, 1958, 23(3), 459–493.

[2] STACEY, T. R.: Seismic assessment of rock masses. *Symp. on Exploration for Rock Engineering*, Johannesburg, 1976, 2, 113–117.

[3] SENGUN, N.–ALTINDAG, R.–DEMIRDAG, S.–YAVUZ, H.: P-wave velocity and Schmidt rebound hardness value of rocks under uniaxial compressional loading. *International Journal of Rock Mechanics and Mining Sciences*, 2011, 48, 693–696.

[4] NUR, A.–SIMMONS, G.: The effect of saturation on velocity in low porosity rocks. *Earth and Planetary Science Letters*, 1969, 7, 183–193.

[5] YU, G.–VOZOFF, K.–DURNEY, D. W.: The influence of confining pressure and water saturation on dynamic elastic properties of some Permian coals. *Geophysics*, 1993, 58(1), 30–38.

[6] HE, T.–SCHMITT, D. R.: Velocity measurements of conglomerates and pressure sensitivity analysis of AVA response. *Proceedings of the 76th SEG International Exposition and Annual Meeting, New Orleans*, USA, 2006, 1–6 Oct.

[7] EBERHART-PHILLIPS, D.–HAN D. H.–ZOBACK, M. D.: Empirical relationships among seismic velocity, effective pressure, porosity, and clay content in sandstone. *Geophysics,* 54/1 P82–89

[8] BIRCH, F.: The velocity of compression waves in rocks to 10 kilobars, Part 1. *Journal of Geophysics Researc*h, 1960, 65, 1083–1102.
[9] SINGH, R.–RAI, C.–SONDERGELD, C.: Pressure dependence of elastic wave velocities in sandstones. *Proceedings of the 76th International Exposition and Annual Meeting*, SEG, 2006, 1883–1887.
[10] BEST, A. I.: The effect of pressure on ultrasonic velocity and attenuation in near-surface sedimentary rocks. *Geophysical Prospecting*, 1997, 45, 345–364.
[11] WALSH, J.B.-BRACE, W.F.: A fracture criterion for brittle anisotropic rock. J. *Geophysical Research*, 1964, 69, 3449–3456.
[12] WEPFER, W. W.–CHRISTENSEN, N. I.: A seismic velocity-confining pressure relation, with applications. International Journal of Rock Mechanics and Mining Science, 1991, 28, 451–456.
[13] JI, S.–WANG, Q.–MARCOTTE, D.–SALISBURY, M. H.–XU, Z.: P wave velocities, anisotropy and hysteresis in ultrahigh-pressure metamorphic rocks as a function of confining pressure. *Journal of Geophysical Research*, 2007, 112, B09204.
[14] DOBRÓKA, M.–SOMOGYI MOLNÁR, J.: New petrophysical model describing the pressure dependence of seismic velocity. *Acta Geophysica*, 2012, 60(2), 371–383.
[15] SOMOGYINÉ MOLNÁR, J.: *Rugalmas hullámok terjedési jellemzőinek nyomásfüggése – új kőzetfizikai modellek*. Miskolci Egyetem, PhD-értekezés, 2013.
[16] MOHIUDDIN, M. A.–KORVIN, G.–ABDULRAHEEM, A.–AWAL, M. R.–KHAN, K.–KHAN M. S.–HASSAN, H. M.: Stress-dependent porosity and permeability of a suite of samples from Saudi Arabian sandstone and limestone reservoirs. SCA2033, *Symposium of Core Analysts*, Abu Dhabi, 2000.
[17] RHETT, D. W.–TEUFEL, L. W.: Effect of reservoir stress path on compressibility and permeability of sandstones. *SPE 24756, the 67th SPE Annual Technical Conference and Exhibition*, Washington, 1992 Oct.
[18] ZIMMERMAN, R. W.: Compressibility of sandstones. *Developments in Petroleum Science*, 29, Elsevier, New York, 1991.
[19] HAN, G.–DUSSEAULT, M. B.: Description of fluid flow around wellbore with stress-dependent porosity and permeability. *Journal of Petroleum Science & Engineering*, 40, 1–16, 2003.
[20] GOMEZ, C. T.–DVORKIN, J.–VANORIO, T.: Laboratory measurements of porosity, permeability, resistivity and velocity on Fontainebleau sandstones. *Geophysics*, 2010, 75/6.
[21] TOKSÖZ, M. N.–JOHNSTON, D. H.–TIMUR, A.: Attenuation of seismic waves in dry and saturated rocks, I. Laboratory measurements. *Geophysics*, 1979, 44(4), 681–690.
[22] MENKE, W.: *Geophysical data analysis – Discrete inverse theory*. Academic Press, Inc. London Ltd., 1984.

Geosciences and Engineering, Vol. 2, No. 4 (2013), pp 59–65.

COMPARATIVE STUDY OF A SUBURBAN AND A RURAL TOWN'S QUALITY OF LIFE

TIBOR KORODI–JUDIT MOLNAR

University of Miskolc, Institute of Geography

1. Abstract

Quality of life studies since the 1970s have increasingly focused on ˝well-being" instead of welfare, so a more precise, differentiated analysis has become important [1]. Thus among the factors put forward by Allart, apart from "having", "loving", "being" and, especially, health are beginning to be seen as more important in determining quality of life. [2][3]. This work is part of a wider project in which different settlements with different geographical characteristics are examined in Borsod-Abaúj-Zemplén County and both the objective and subjective factors in quality of life are assessed. In this study we compare Bódvaszilas, a rural village, and Kistokaj a suburban settlement by investigating the population's attitude to their health issues and welfare.

2. Introduction

Previous studies have shown that there is no correlation between objective health (i.e. as measured by medical doctors) and well-being, but there is between subjectively ascribed health and well-being [4]. This study's goal is to examine what the subjective quality of life is in the two selected settlements in Borsod-Abaúj-Zemplén County. Kistokaj is a small town (2011 population: 2071) in the suburban area of Miskolc with an increasingly growing population. Bódvaszilas is also a small town, but in the north of the county, next to the national border, and far away from cities (Figure 1). It had 1101 inhabitants in 2011 and has a decreasing population. Presumably the quality of life is higher in Kistokaj, which is more engaging for young people, than in Bódvaszilas, which has an ageing society. Investigating the statistical data it can be seen that living standards are higher in Kistokaj then in Bódvaszilas. The unemployment rate is relatively low in Kistokaj (5.69%) while in Bódvaszilas this value is almost double (10.76%). In the case of the number of cars the figures show similar differences: inhabitants in Bódvaszilas own 16.2 cars/100 person and 32.7 cars/100 person in Kistokaj. Therefore about every third inhabitant has a car in Kistokaj and around every sixth person owns one in Bódvaszilas.96% of the houses are part of the mains water-supply system in Kistokaj, but in Bódvaszilas this value is only 80%. Eight new homes were built in Kistokaj (seven with four or more rooms) in 2010 while only one was built in Bódvaszilas in 2010.

This paper focuses on 'subjective well-being' which we need to distinguish from real well-being. As FEKETE, following ZAPF, explains we only can speak about real well-being if the objective and subjective aspects of well-being exist simultaneously [4].

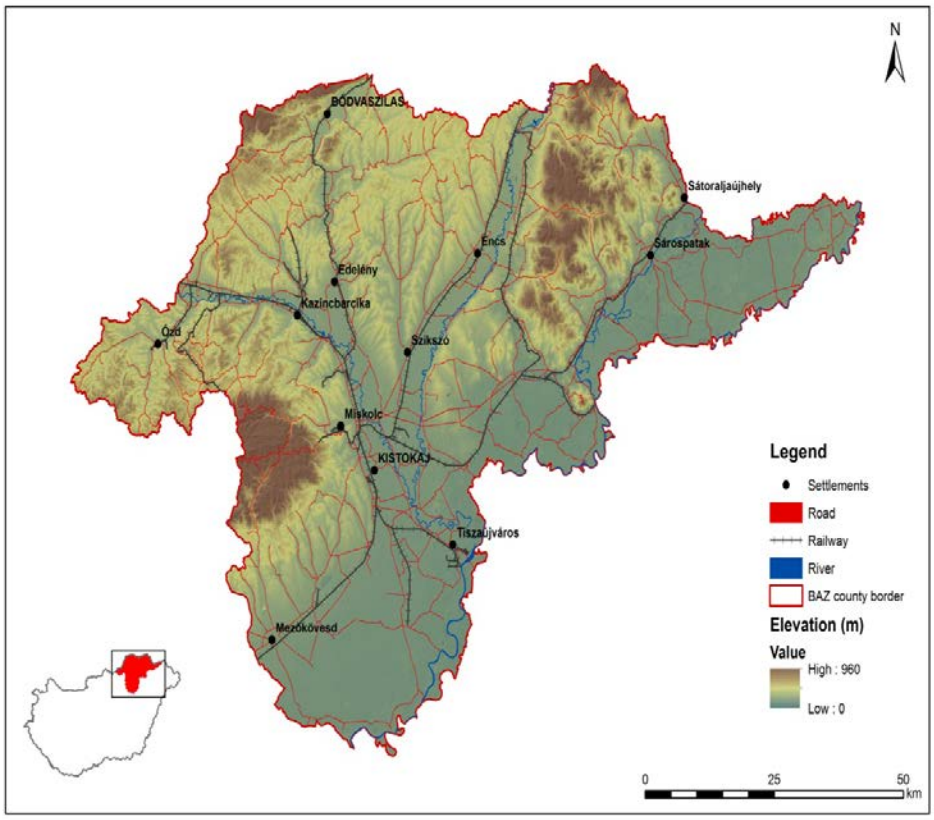

Figure 1
The research settlements and their surrounding area

The study has the following questions:

- What are the priority factors in quality of life in the study population?
- What is the relationship between living standards and subjective quality of life?
- Is there any relationship between the studied villages' settlement hierarchy role, the population's socio-economic situation and their subjective quality of life?
- If there is any relationship, what characteristics can be used to describe them?

3. Materials and methods

The method of research is questionnaire survey and statistical data-analysis. We asked 104 people in Kistokaj (total population in 2011: 2071) and 96 dwellers in Bódvaszilas (total population in 2011: 1101). We did not perform a probability sample, but we raised the

number of our sample to 5% in Kistokaj and 8% in Bódvaszilas. Data processing was done using SPSS software.

4. Priority values in quality of life

In our survey we were curious to see the most important factors in the study population's 'quality of life'. We asked our respondents to put into order the following factors: job, family, money, health, religion, and environment. Then we processed the data and gave a value to every factor according to the rankings in order to produce a 6 point scale. The most important element was given the maximum value (6), and the least important was given the minimum value (1).

In Figure 2 the priority values are shown. First of all, there is a noticeable similarity between the study populations' attitudes, the ranking of the factors being almost the same. Both of them placed the highest value on family. Bódvaszilas has a higher mean age and a higher aging rate than what is usual in rural places. Tradition plays an important role, which would explain the higher value of family in Bódvaszilas (5.17). However, this number is also high in Kistokaj (5.00), because mainly young, new family-starting people, who value family highly, have moved there in the recent period.

The second most important factor is health. Similarly, it is slightly higher in Bódvaszilas (4.57), then Kistokaj (4.47). The survey has a lot of questions about health and healthy lifestyle and we have found that although people recognize that their health is important, they do not do enough to improve it. Usually the respondents answered that they do not have enough opportunities to live a healthy lifestyle - mainly due to "time" and "money". Our results show that if someone put "money" or "job" high in their hierarchy than "health" received a low level of importance and vice versa. There are several studies confirming that the social-economic situation really has a great impact on health qualities [5][6]. Hungary, especially Borsod-Abaúj-Zemplén County, has a notably low quality of health, so it is a hopeful sign that inhabitants of this area understand the importance of their health, but it is also necessary to examine how we can help people to improve the health related aspects of their quality of life.

Work and money factors have a medium value in both settlements. Kistokaj has a higher value for work (3.88) and money (3.59) than Bódvaszilas (3.53 and 3.46). These values represent the young population's career orientation in Kistokaj. Commonly the importance of work entails less importance being placed on family in such studies, but our research suggests that in these communities the situation is different [7]. We need more evidence to ensure that our findings are facts and, if so, potentially special characteristics of this area.

The respondents rank religion and the environment last. We can see here the only difference of the sequences. In Kistokaj there is a higher priority value of environment (2.38) than religion (1.77), in contrast in Bódvaszilas, where the religion (2.27) is more important than environment (1.97). It is interesting that Bódvaszilas is surrounded by hills, forests and located in a clean, quiet and undisturbed area and yet the environment is considered the least important factor there.

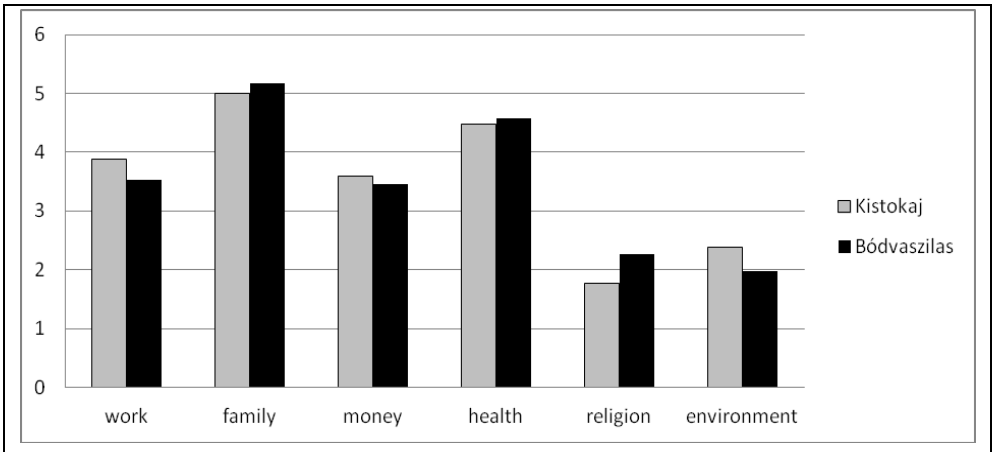

Figure 2
Priority values in quality of life

Interestingly, we cannot see big differences in the case of these priority values given by our respondents in Bódvaszilas and Kistokaj, despite palpable disparity in living standards and the role of the settlement hierarchy between these villages.

5. Subjective factors in quality of life

Researchers mainly measure subjective quality of life using satisfaction and happiness variables [8]. In our survey we have paid particular attention to health variables too. We asked four questions, which focus on the subjective quality of life:

- How satisfied are you with your life?
- Do you feel happy in your living environment?
- How stressful is your life?
- How would you rate your health status?

The respondents could answer these questions on a 1 to 10 scale.

In Figure 3 we can see the average values of these variables. The major difference is experienced in the satisfaction variable, in Kistokaj there is a value of 5.80, while in Bódvaszilas it is 6.43. The happiness value is also higher in Bódvaszilas (6.82), than in Kistokaj (6.65). We saw that in Bódvaszilas religion is more important among our respondents than in Kistokaj. Many researches evinced that religious people are happier and generally more satisfied [9]. That could alter this difference in our study as well. Of course, it is not the only variable which is likely to cause this difference. We might expect that the lower value of satisfaction and happiness in Kistokaj is derived from the more urban and more stressful lifestyle there, but this is not supported by this research. 'Stressful lifestyle' has a similar value in Kistokaj (6.38) to that in Bódvaszilas (6.30) according to the answers of our respondents. However, we do not know about these people's expectations; maybe

those who live in Kistokaj and answered our questions, could not meet their own requirements as well as respondents in Bódvaszilas. They assess their health quality in the same way, in Bódvaszilas there is a value of 6.61, while in Kistokaj it is 6.50. We examine the reasons for this in the next section.

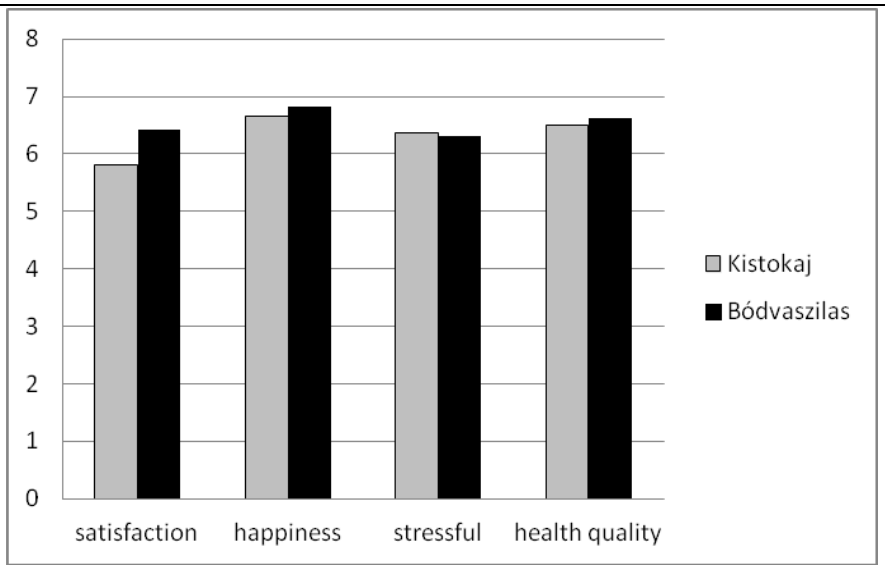

Figure 3
Subjective factors in quality of life

In this early stage of our research it seems that the statistically measured living standards do not correlate well with the subjective quality of life indices in the case of these settlements. Despite the evidence suggesting better living standards in Kistokaj, values of satisfaction and happiness are higher in Bódvaszilas. To discover the reason behind these results we need to conduct further investigations into the objective and subjective well-being in the research area.

6. Influential health factors

Health has a very important role in subjective quality of life. Chronic diseases can affect many parts of people's lives, and can even impede some essential activities [10]. In our survey we asked four questions about influential health factors:

- How much can you influence your own health?
- How much does your quality of health depend on your living environment?
- To what extent are you living a healthy lifestyle?
- How do you rate the health care of your living environment?

The respondents could answer these questions on a 1 to 10 scale. Figure 4 shows the results of our findings regarding these issues. Nowadays, more and more experts believe that improving the health status of the population is not only a medical but also a social task, and the idea that our quality of health mainly depends on our lifestyle is becoming generally accepted [11][12][13]. Based on our research data, it seems that Kistokaj's younger and more qualified population is more aware of this than Bódvaszilas's older and less qualified population, but we have to mention that there is no enormous difference between the two values (6.68 and 6.54). A larger difference can be observed in the environment's influence on health. In Kistokaj our respondents gave a score 5.21 for this, while in Bódvaszilas they only valued it to 4.78. Interestingly enough, based on their own accounts, people feel in Kistokaj that they live a less healthy lifestyle (5.74) than how people who we asked in Bódvaszilas evaluated this factor (6.02). Also interesting was that in Bódvaszilas the respondents are more satisfied with the health care system (7.23) than in Kistokaj (6.59) where people have better access to health facilities and better quality of care in Miskolc. It is indeed intriguing that Bódvaszilas received such high values for this factor, because in Borsod-Abaúj-Zemplén County there is a low quality of health care compared to the national average.

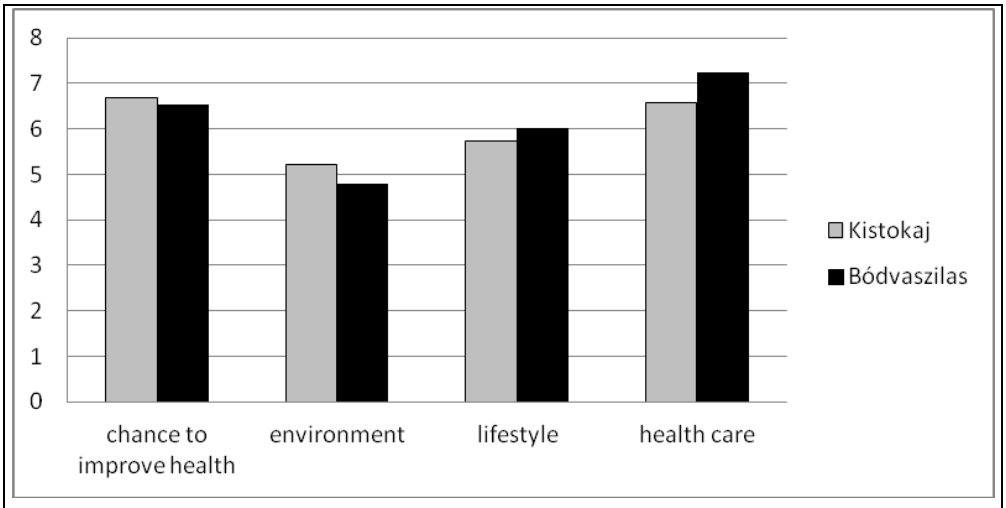

Figure 4
Influential health factors

7. **Conclusion**

Through the research we found that there is no significant difference between the settlement hierarchy role and their population's subjective quality of life at first sight. We think we will need to investigate further variables, like expectations, cultural issues etc. which could alter our results in measuring and comparing quality of life in settlements with different characteristics. In Bódvaszilas despite living far away from the county center and urban

places, people have better subjective quality of life parameters. They also have a worse socio-economic situation. Although Kistokaj has virtually become the new residence of the wealthier employees of Miskolc our respondents there were less happy and less satisfied than those in Bódvaszilas. Our hypothesis is that their life has been more affected by the down turning of Miskolc than people's lives in the remote part of the county which has suffered from crisis and disadvantaged or unfavorable economic and social circumstances for decades.

8. References

[1] HÁRI, P.: A magyar társadalom attitűdjei a környezethez és ezek kapcsolata az emberek boldogságérzetével. In: *Az életminőség feltételei*. (szerk.: Utasi Á.) Műhelytanulmányok (11) 2007/1. pp. 38–46.

[2] ALLART, E.: Having, Loving, Being: An Alternative to the Swedish Model of Welfare Research. In: Nussbaum, M–Sen, A. (szerk.): *The Quality of Life*. Clarendon Press, Oxford, 1993.

[3] KOLLÁNYI, ZS.–IMECS, O.: *Az egészség – befektetés. Az egészségi állapot hatása a gazdasági teljesítőképességre és az életminőségre*. Demos Magyarország, Budapest 2007. 118 p.

[4] FEKETE, ZS.: Életminőség. Koncepciók, definíciók, kutatási irányok. In: *A szubjektív életminőség forrásai*. Szerk.: Utasi Ágnes. MTA PTI, Budapest, 2006. 277–-309.

[5] UZZOLI, A.: *Az egészségi állapot társadalmi-területi különbségei Magyarországon*. Doktori tézisek. Eötvös Loránd Tudományegyetem, Budapest, 2004. 11 p.

[6] BEKE, SZ.: *Békés megye népességének egészségi állapota és egészségügyi ellátása*. Doktori disszertáció. Pécsi Tudományegyetem, Pécs, 2009. 193 p.

[7] VARGA, A.: Munkaközpontúság és a társas kapcsolatok eltérő szerveződése. In: *Az életminőség feltételei*. (szerk.: Utasi Á.) Műhelytanulmányok (11) 2007/1 pp. 84–93.

[8] MOLNÁR, J.: Szubjektív életminőség vizsgálat a Bodrogközben. *Települési környezet Konferencia*, CD kötet. Debrecen. 2005

[9] BARNA, ZS.: Vallásosság a szubjektív életminőségben. In: *Az életminőség feltételei*. (szerk.: Utasi Á.) Műhelytanulmányok (11) 2007/1. pp.116–134.

[10] KUCSERA, CS.: *Egyedülálló, idős budapestiek szubjektív életminősége*. Doktori disszer-táció. Eötvös Loránd Tudományegyetem, Budapest, 2008. pp. 36-47.

[11] CSOBOTH, CS.: Magtartás-epidemiológia. In: Buda B.–Kopp M.–Nagy E. (szerk): *Magatartástudományok*. Medicina Könyvkiadó Rt. Budapest, 2001. pp. 715–728.

[12] TUNSTALL, H. Z. V.–SHAW, M.–DORLING, D.: Glossary: Places and health. *Jurnal of Epidemiology and Community Health* 2010. 58, pp 6–10.

[13] UZZOLI, A.: Az egészségi állapot világméretű különbségei. Földrajzi Értesítő 2008. LVII. évf., 3–4 füzet, pp. 399–415.

Geosciences and Engineering, Vol. 2, No. 4 (2013), pp 66–80.

ANALYSIS OF DROUGHT CONDITIONS IN THE CARPATHIANS USING STANDARDIZED PRECIPITATION INDEX (SPI) 1951–2050

JÁNOS VÁGÓ–ANDRÁS HEGEDŰS–ENDRE DOBOS

University of Miskolc, Institute of Geography and Geoinformatics, Miskolc – Egyetemváros, 3515. Hungary, ecovago@uni-miskolc.hu

1. Abstract

The Standardized Precipitation Index (SPI) is a valuable tool to analyze the frequency and severity of drought events. Under the aspect of future climate change, it is important to know how drought conditions might change. In this study – within the framework of CarpathCC project –, these future drought conditions were examined on the basis of SPI values in the Carpathian Region to map adequate adaptation measures.

The results show that the frequency and severity of drought events are expected to be increased in the whole Region. However, significant regional differences are expected in the distribution and severity of drought events. The most affected areas by droughts are the Southwestern Carpathian subregion, the Southern Carpathian subregion and the Tarnave Mare area.

2. Introduction

Drought is a natural phenomenon, which is usually caused by the lack of precipitation over a sustained period of time. It is one of the most important climate-related natural hazards.

Droughts can be classified as meteorological, hydrological and agricultural droughts [1]. The meteorological drought can be expressed by the drought indices. According to the National Meteorological and Hydrological Services (NMHSs) the Standardized Precipitation Index (SPI) is one of the most reliable indices to be used to characterize meteorological droughts [2].

The Standardized Precipitation Index [3, 4] is widely accepted and used throughout the world. According to its definition the standardized precipitation is simply the difference of precipitation from the mean for a specified time period divided by the standard deviation, where the mean and standard deviation are determined from past records [3]. The standardization allows the SPI to determine the severity and rarity of a current drought event [5]. The SPI can be calculated for a variety of timescales. This versatility allows the SPI to monitor short-term water supplies, such as soil moisture, and longer-term water resources such as groundwater supplies, lake and reservoir levels [6]. A great advantage of the SPI that it is also a useful tool to determine the wet periods and can be applied in the monitoring of flood events as well [7].

In this study - as a part of the CarpathCC project - SPI was used as an indicator to analyze drought events and to provide drought forecast regarding to the future climate change. The aim of the CarpathCC project was to analyze the Carpathian Region's vulnerability to climate changes. The examinations were carried out for the entire Carpathian Region and for five representative focal areas, which are under the direct impacts of climate change: Iron Gates NP (RO), Tarnave Mare Area (RO), Rodna-Maramures (RO), Bükk Mountains (HU) and Tatra Mountains (High Tatras, SK).

3. Materials and methods

The CLAVIER database was used for the calculation of SPI values, where climate change was analyzed between 1951 to 2050, based on existing data and on very high detail climate projections with to fulfill the need of local and regional impact assessment. The Carpathian Region database is presented by a grid having 9113 cells, where each grid cell represents a 7 by 11 km wide area (0.1 degree). The database contains minimum-, maximum- and mean daily temperature data and 6-hour daily precipitation data from 1951 to 2050.

The calculation of SPI value is simple, requires only one input variable: the monthly precipitation data, ideally for at least 30 consecutive years. The monthly precipitation dataset was prepared from the 6-hour daily precipitation dataset by the Climate Data Operators 1.5.3 (CDO).

Calculation of SPI begins with building a frequency distribution from precipitation data at a certain location for a specified time period [8]. The SPI can be computed for a 1-month total of precipitation as well as 48-months total of precipitation. A gamma probability density function is fitted to the precipitation data and the cumulative distribution of precipitation is determined. This step is followed by an equiprobability transformation made from the cumulative distribution fitted to a the standard normal distribution. This transformed probability is the SPI value [9]. Positive SPI values indicate greater than median precipitation (wet period), and negative values indicate less than median precipitation (drought period).

This calculation can be done by applying the SPI calculators. In this study the SPI_SL_6 calculator was used (available at http://drought.unl.edu). The script is able to calculate SPI values for different time periods: 1, 3, 6, 12, 24, 48 months [9], that makes possible to analyze the changes of precipitation at different scales. The length of the calculated period is optional, but the minimum period is 30 years. The 1-month SPI reflects relatively short-term conditions, therefore it is applicable mainly in the agricultural sector. In regions where rainfall is normally low during a month, large negative or positive 1-month SPI values may mislead the users. The 3-month SPI provides seasonal estimation of precipitation; it can also be applied for agricultural purposes. The 6-month SPI indicates medium-term trends in precipitation, it can be applied in hydrological researches. The 12-month SPI (and longer periods) reflects long-term conditions, for example changes of groundwater level.

The SPI_SL_6 computes the SPI values for discrete locations ("precipitation stations"). In this study the monthly precipitation data of 82 locations were used for the calculations (Figure 1.). The locations were selected from the CLAVIER database, where each location represent a grid cell with precipitation data from 1951 to 2050.

The script is very easy to operate: the first step is to enter the number of monthly intervals (1–6). The first phase is to enter the SPI monthly intervals (1, 3, 6, 12 months etc.). After entering the input and output file names, the program calculates the SPI values and export them into an ASCII file. The SPI represents a cumulative probability in relation to the base period for which the gamma parameters were estimated [9]. Using the SPI as an indicator, a drought event is defined as a period in which the values are continuously negative [3], the wet period begins when the value rises above zero.

The output files of the 82 locations were aggregated in a table and were joined to locations' GIS layer. These point were used to interpolate the drought maps.

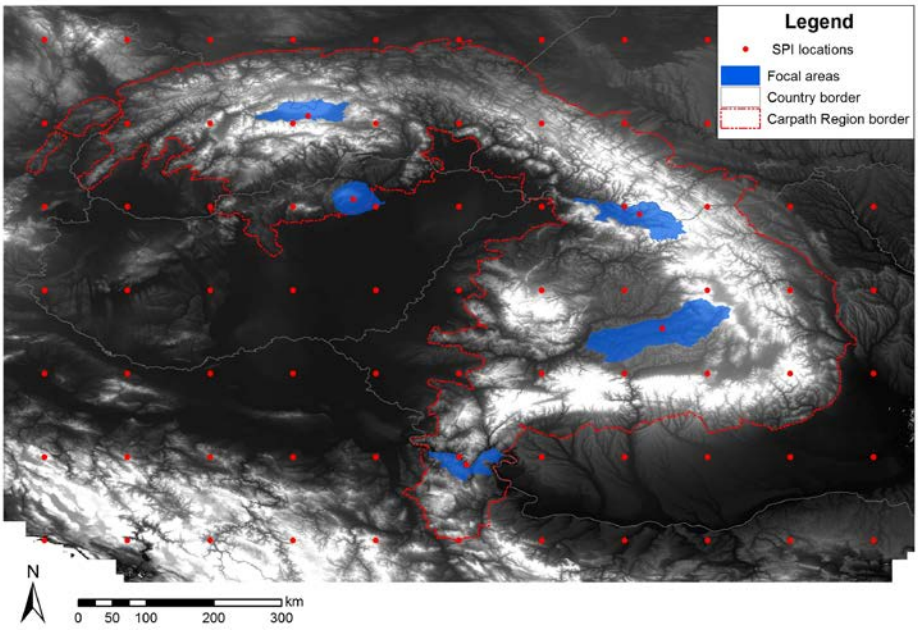

Figure 1

Location of the SPI calculating points in the Carpathian Region

Table 1

Wet and drought period classification and probability of occurrence based on the SPI values [3, 10]

Index value	Class	Probability
SPI≥ 2.00	Extremely wet	0.023
1.50 ≤SPI≥ 2.00	Very wet	0.044
1.00 ≤SPI≥ 1.50	Moderately wet	0.092
–1.00 ≤SPI≥ 1.00	Near normal	0.682
–1.50 ≤SPI≥–1.00	Moderate drought	0.092
–2.00 ≤SPI≥–1.50	Severe drought	0.044
SPI≤–2.00	Extreme drought	0.023

4. Results and discussion

4.1. Analysis of SPI values in the Carpathian Region

The 1-, 3-, 6- and 12-months SPI values were calculated for each location for the 100 year period. Because of the above mentioned uncertainty only the 3-, 6- and 12-months SPI values were analyzed and the 1-month SPI was ignored.

Analyzing the SPI values in the whole Carpathian Region, the most conspicuous change is that the climate is getting more arid. The trend fitted on the graphs (Figure 2) shows slight decrease in the mean of the SPI values, which indicates the increasing lengths of the dry periods. This increase is expressed both in the frequency and the severity of drought events.

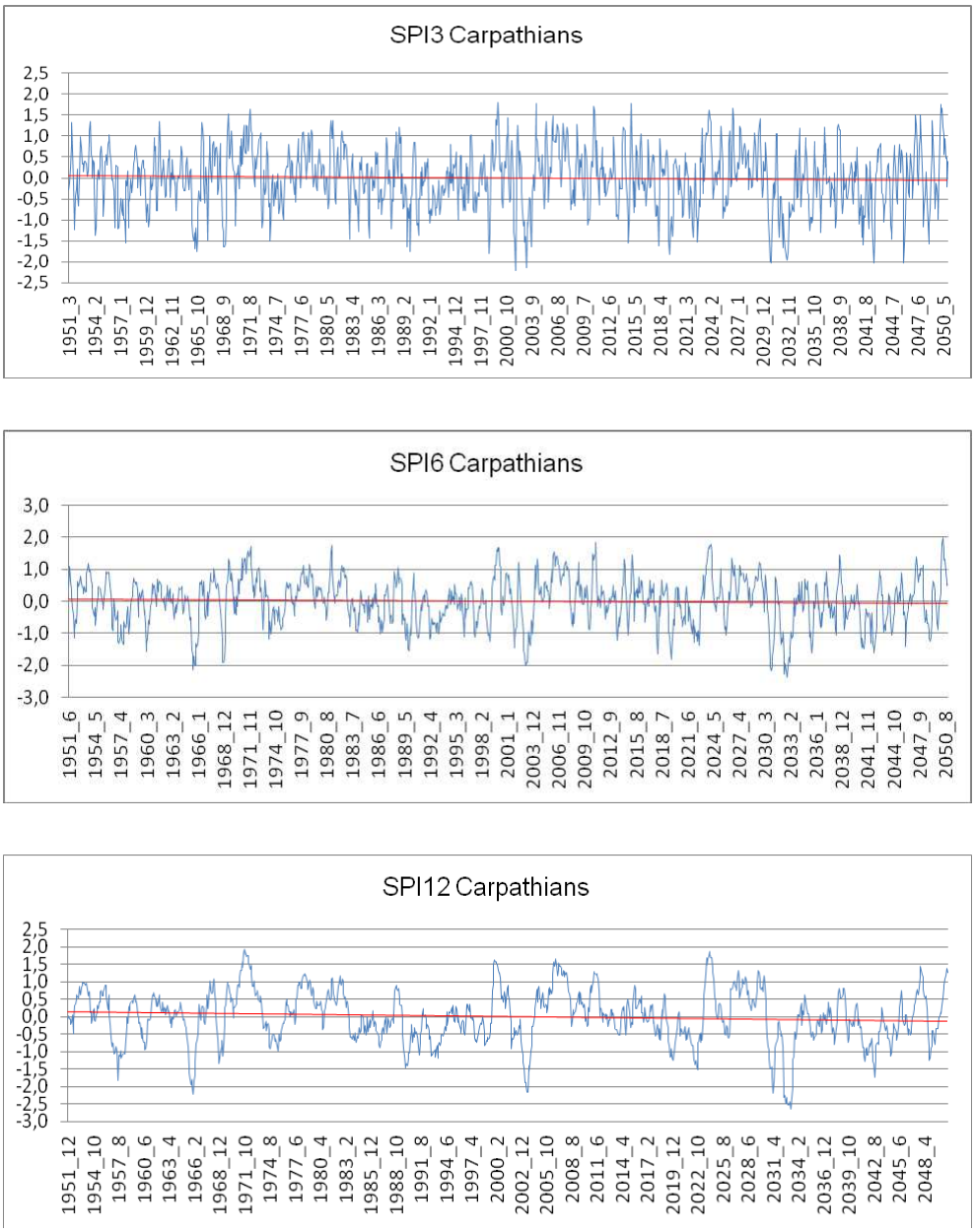

Figure 2

Mean SPI values of the Carpathian Region for the 3-, 6- and 12-months time scale (1951–2050)

The most significant increase of drought events can be seen on the medium- and long-term (SPI6 and SPI12) graphs. According to our study the frequency and severity of the short-term droughts (SPI3) will not change until the end of the period. On the basis of 30-years average SPI values (Table 2) it can be stated that in the middle of the last century (1971–2000) the climate was slightly wetter (SPI: 0,040–0,063). While at the end of the examined period (2021–2050) the climate will get more arid, especially in case of long-term droughts (SPI: -0,051–-0,126), the SPI values are in the "near normal" SPI class in the whole 100 years.

The SPI indices can be used to analyze both wet and drought periods. The "normal" climate conditions are represented by –1<SPI<1 values. When the SPI value is below –1, or above +1, "not normal" conditions can be observed. According to the calculations (Table 3), the frequency of these not normal events will increase as compared with the beginning of the period. The rate of the years between 1871 and 2000 with not normal climate conditions was 13-15%, while in the 2021–2050 period this rate will probably increase to 21–23%.

Analyzing the frequency of moderate, severe, and extreme drought conditions (Table 3) a well expressed increase can be recognized in 3-, 6-, and 12-months periods as well. The change is the most significant in case of severe and extreme droughts: according to the CLAVIER model output, in the 1971–2000 period the frequency of these droughts was very low (0-1,11%), while the frequency of these events will rise up to ~4-5% in the 2021-2050 period.

Table 2

30-years average SPI values of the Carpathian Region

	SPI3	SPI6	SPI12
1971–2000	0,040	0,041	0,063
2021–2050	–0,051	–0,080	–0,126

Table 3

Percentage of different precipitation conditions
in the period of 1971–2000 and 2021–2050
in the whole Carpathian Region

Not normal conditions (-1 ≥ SPI value ≥ 1)

	SPI3 (%)	SPI6 (%)	SPI12 (%)
1971–2000	13,33	14,72	15,56
2021–2050	21,94	23,06	21,11

Moderate drought conditions (-1,5 < SPI value < -1)

	SPI3 (%)	SPI6 (%)	SPI12 (%)
1971–2000	5,56	5,83	4,17
2021–2050	11,39	14,72	11,67

Severe drought (-2 < SPI value < -1,5)

	SPI3 (%)	SPI6 (%)	SPI12 (%)
1971–2000	1,11	0,28	0,00
2021–2050	3,61	4,72	5,00

Extreme drought conditions (SPI value < -2)

	SPI3 (%)	SPI6 (%)	SPI12 (%)
1971–2000	0,00	0,00	0,00
2021–2050	0,83	2,22	3,89

4.2. Spatial analysis of SPI values – Drought maps

Drought maps were created applying GIS based methods to characterize the changes in the drought conditions. The bases of these maps were the above mentioned 82 SPI locations, where the drought indices were calculated for. The 1971–2000 and 2021–2050 periods were compared and examined.

Instead of using the "raw" SPI values in the mapping process, the number of time periods was determined and mapped, which satisfied the drought criterion according to the following criterion:

SPI < –1 (moderate drought conditions)
SPI < –1,5 (severe drought conditions)
SPI < –2 (extreme drought conditions)

The number of these "selected" periods was compared to the whole 30-years period in each SPI locations, so the maps are visualizing the probability (%) of the moderate/severe/extreme drought events.

4.2.1. Results of the analysis of drought maps

4.2.1.1. Moderate drought events (Figure 3–4.)

The probability of moderate drought events was much lower in the period of 1971-2000 than it is expected in the period of 2010–2050 in short-, medium-, and long-terms for the whole Carpathian Region.

The most endangered areas by the moderate drought events are the central part of the Southwestern Carpathian subregion with the Iron Gates NP and the eastern side of Southern Carpathians with Tarnave Mare Area. At the southern part of NW Carpathians (around Budapest) the probability of drought events is also expected to be increased.

The least affected areas are expected to be the Rodna-Maramures Area and the eastern borders of NW Carpathians.

4.2.1.2. Severe drought events (Figure 5–6.)

The probability of severe drought conditions is expected to be increased in the Carpathian Region in the 2021–2050 period. In fact the change is more expressed than it was in case of moderate droughts.

The most affected areas are similar: Southwestern Carpathian subregion north from the Iron Gates NP and the eastern side of Southern Carpathians with Tarnave Mare Area. The probability of long-term (12 months) severe drought events could be also relatively high in the NW Carpathian subregion, at the western border of Bükk Mountains and in the Rodna-Maramures area.

The least affected areas by severe droughts are expected to be the Tatra Mountains and the NE Carpathian subregion.

4.2.1.3. Extreme drought events (Figure 7–8.)

The largest change is expected to be in the probability of the occurrence of extreme drought events between the 1971–2000 and 2021–2050 periods. While the increase of probability between the two periods was ~3,5x at moderate droughts, ~5x at severe droughts, in case of extreme droughts this change is ~7x.

The most affected areas are the region between the Bükk Mountains and the northern part of SW Carpathian subregion and the Tarnave Mare Area. The probability of long-term (12 months) extreme drought events is even higher in the Eastern Carpathian subregion and in the eastern half of Rodna-Maramures Area.

The least affected areas by extreme droughts could be the Tatra Mountains, the NE Carpathian subregion and in case of long-term drought events the region of Iron Gates NP.

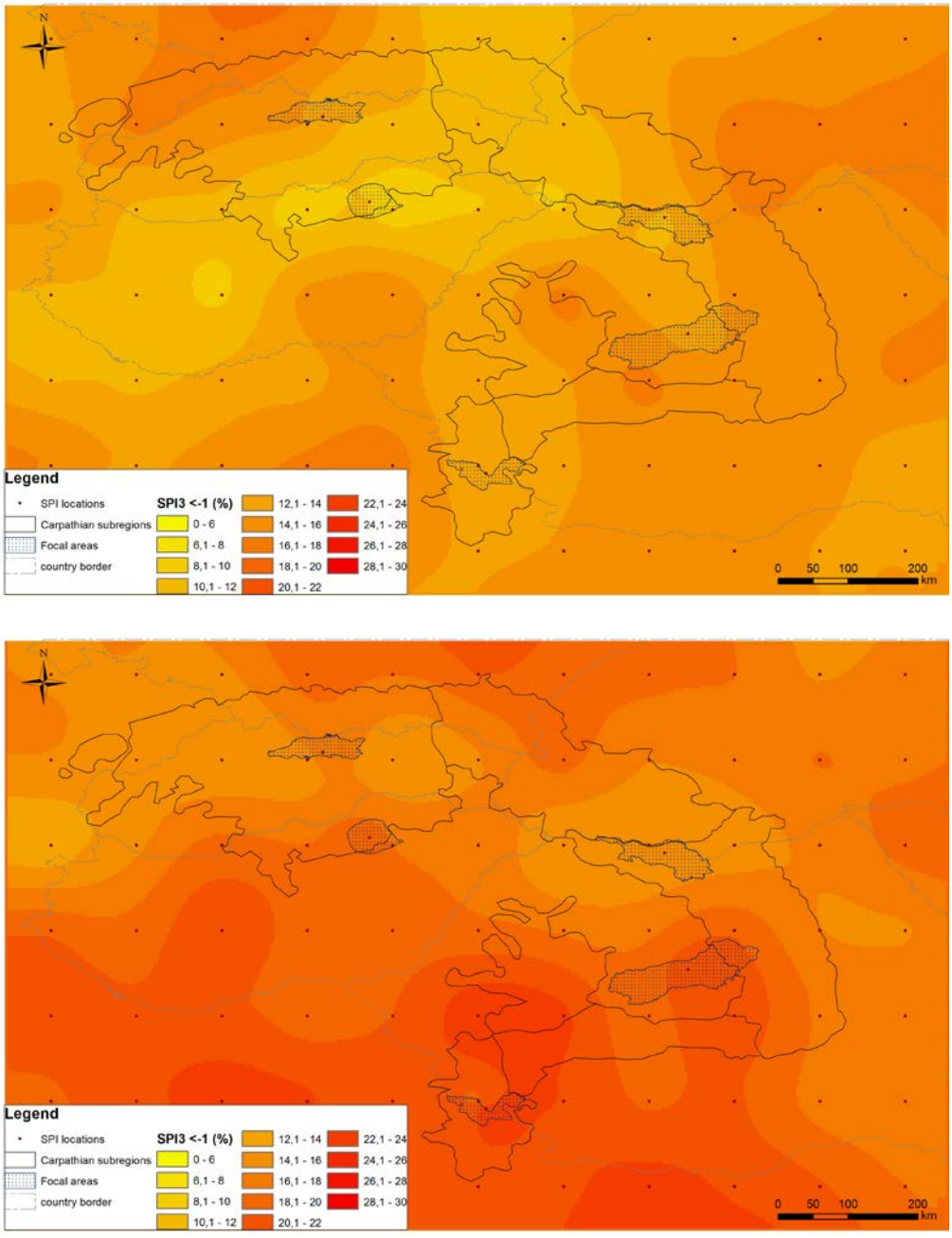

Figure 3

Probability of short-term (3 months) moderate drought events (%) between 1971–2000 (above) and 2021–2050 (below)

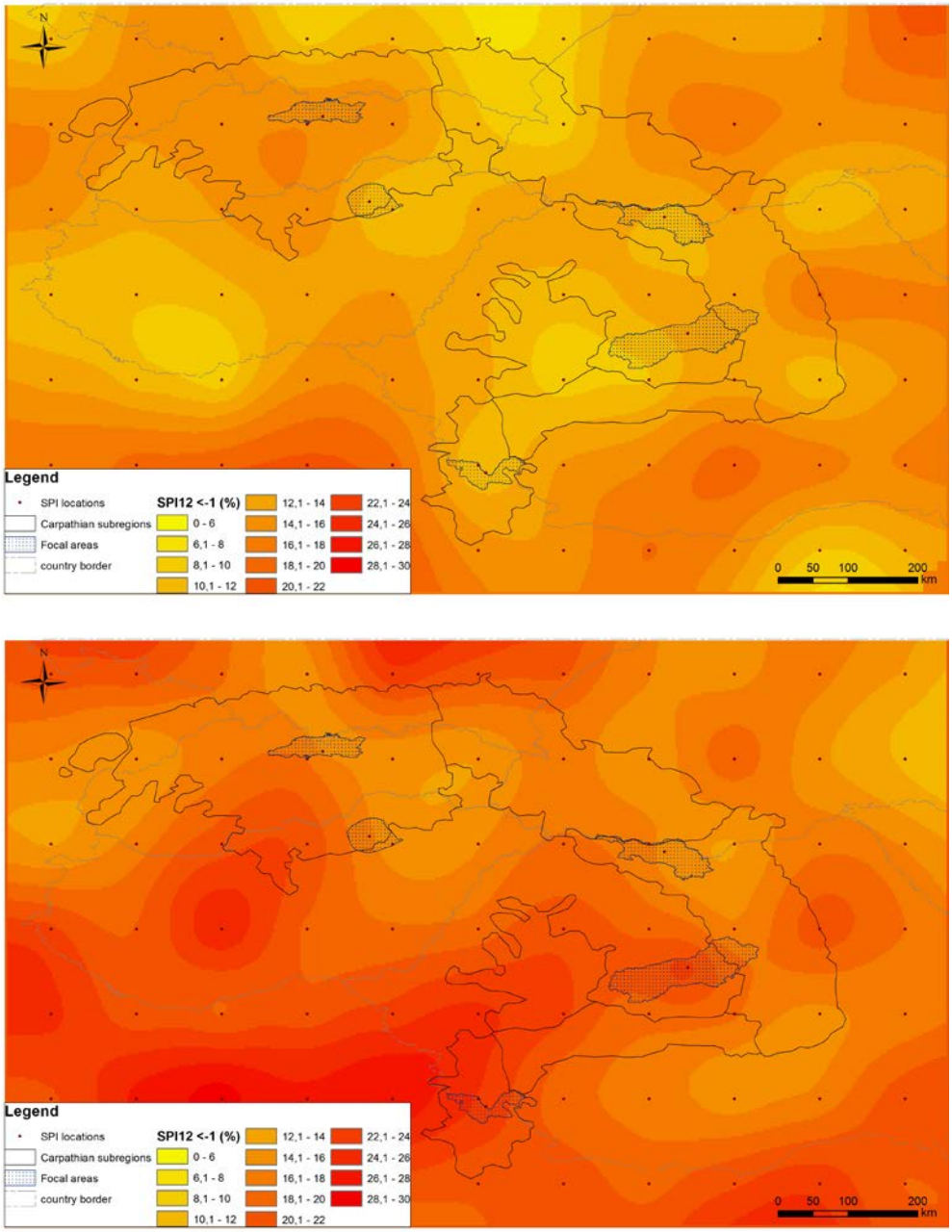

Figure 4

Probability of long-term (12 months) moderate drought events (%) between 1971–2000 (above) and 2021–2050 (below)

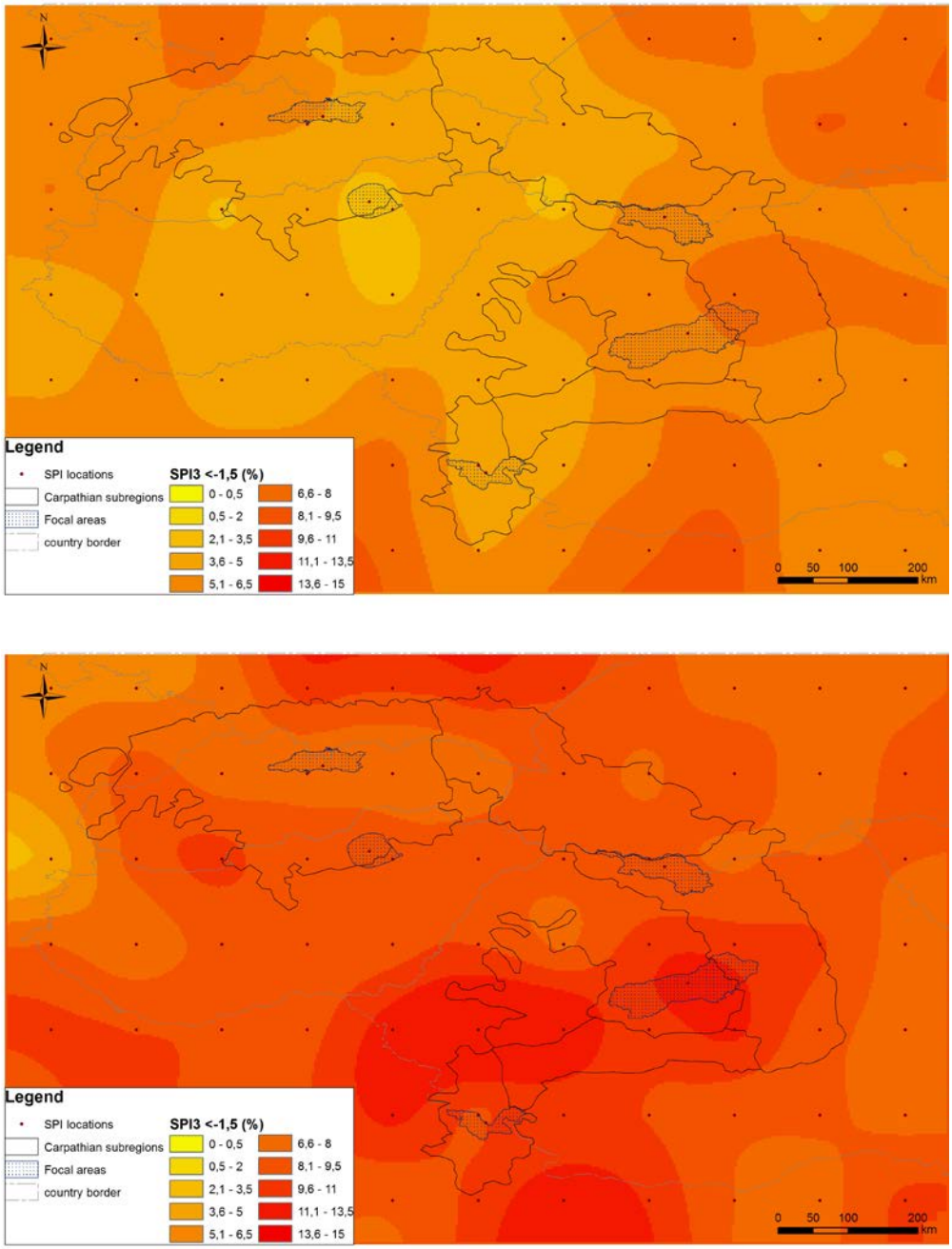

Figure 5

Probability of short-term (3 months) severe drought events (%) between 1971-2000 (above) and 2021-2050 (below)

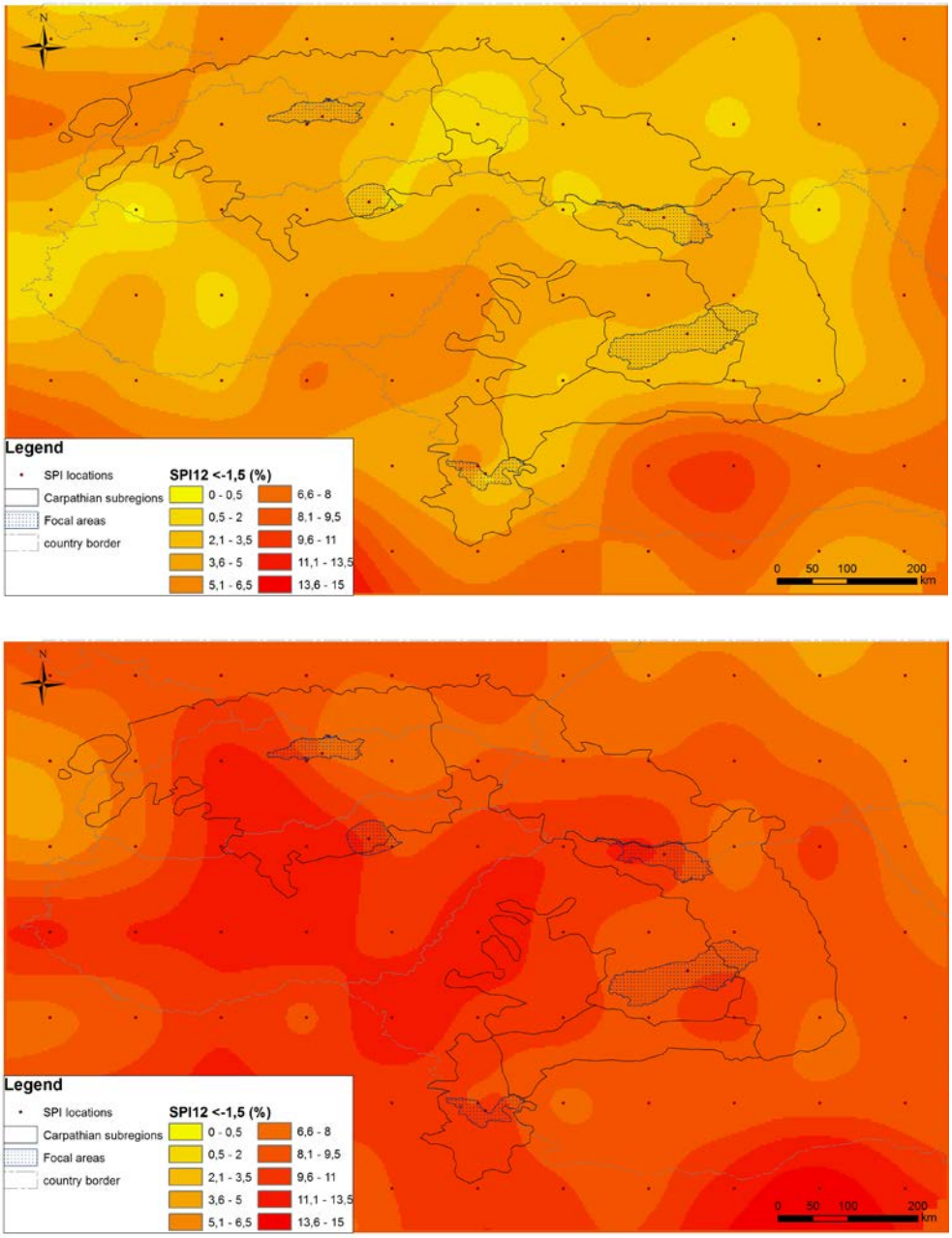

Figure 6

Probability of long-term (12 months) severe drought events (%) between 1971-2000 (above) and 2021-2050 (below)

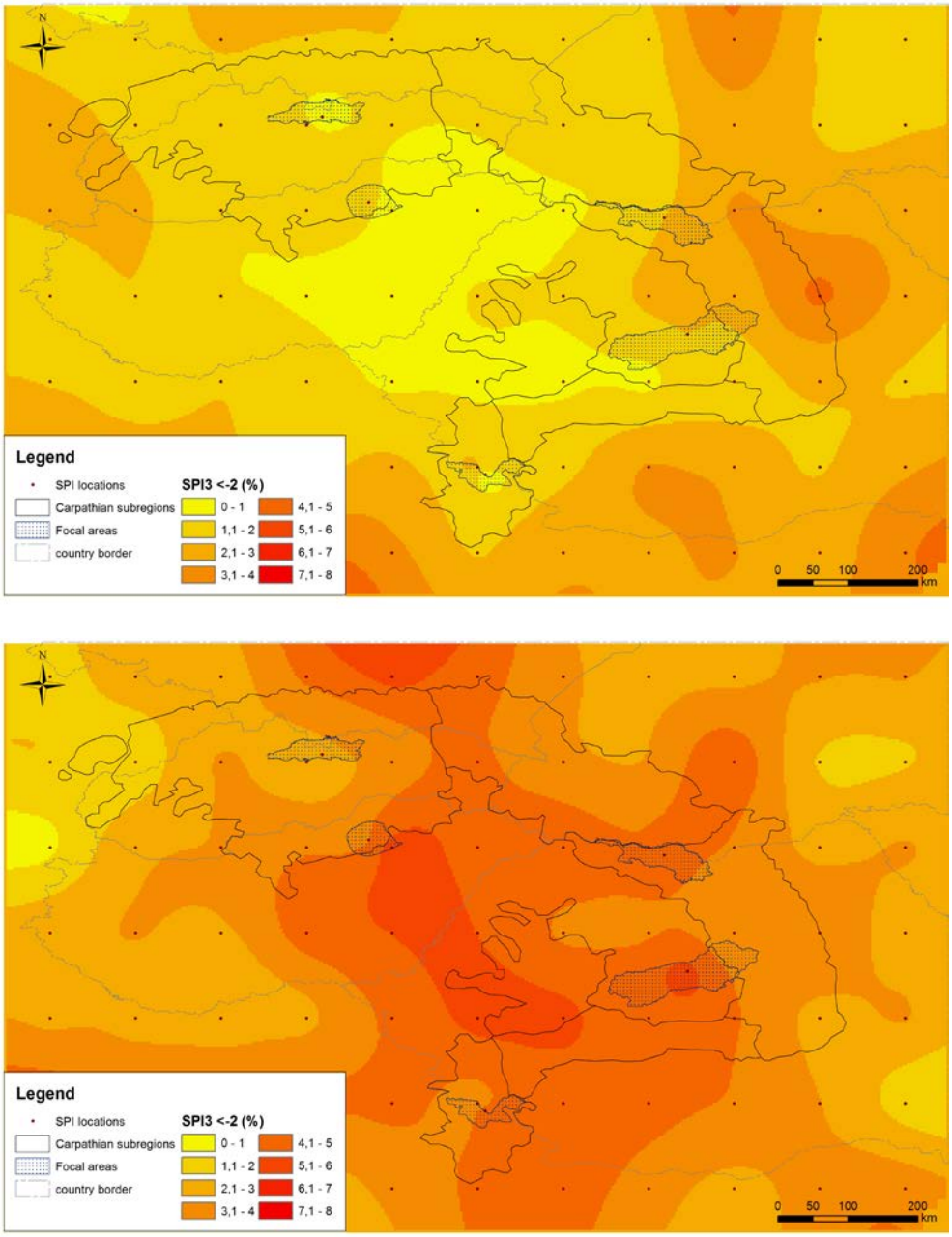

Figure 7

Probability of short-term (3 months) extreme drought events (%) between 1971-2000 (above) and 2021-2050 (below)

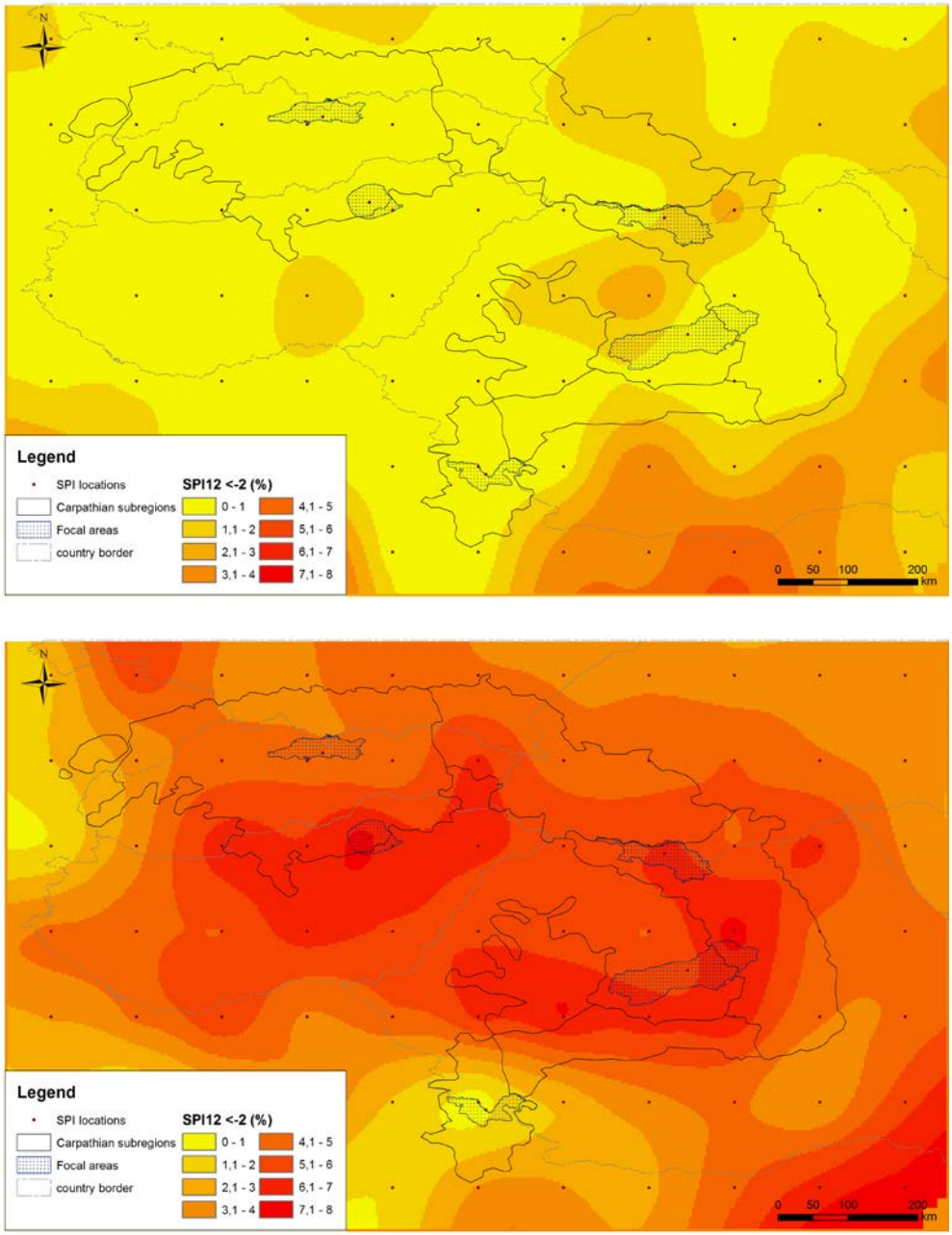

Figure 8

Probability of long-term (12 months) extreme drought events (%) between 1971–2000 (above) and 2021–2050 (below)

5. Conclusion

On the basis of the examinations the following major conclusion can be drawn:

- The frequency and severity of drought events are expected to be increased in the whole Carpathian Region.
- This projected increase can be observed in all cases of moderate, severe and extreme droughts and in short-, medium-, and long term periods as well.
- Significant regional differences are expected in the distribution and severity of drought events.
- The long-term drought events are expected to occur mainly inside the Carpathian Mountains, especially in case of extreme droughts.
- The most affected areas by droughts are the Southwestern Carpathian subregion, the Southern Carpathian subregion and the Tarnava Mare Area focal area.
- The least affected areas are the Tatra Mountains focal area, the Rodna-Maramures Area and the NE Carpathian subregion.

6. Acknowledgement

The work was supported by the CarpathCC Climate Change in the Carpathian Region framework project supported by the European Union.

7. References

[1] LIVADA, I.–ASSIMAKOPOULOS, V. D.: Spatial and temporal analysis of drought in Greece using the Standardized Precipitation Index (SPI). *Theoretical and Applied Climatology*, Volume 89. 2006, 143–153.

[2] HAYES, M. J.–SVOBODA, M. D.–WALL, N.–WIDHALM, M.: The Lincoln Declaration on Drought Indices: Universal Meteorological Drought Index Recommended. *Bulletin of the American Meteorological Society* 92. 2011, 485–488.

[3] MCKEE, T. B.–DOESKEN, N. J.–KLEIST, J.: The relationship of drought frequency and duration of time scales. *Eighth Conference on Applied Climatology*, American Meteorological Society, 17–23. Jan, 1993, Anaheim CA. 1993, 179–186.

[4] MCKEE, T. B.–DOESKEN, N. J.–KLEIST, J.: Drought monitoring with multiple time scales. *Ninth Conference on Applied Climatology*, American Meteorological Society, 15-20. Jan, 1995, Dallas TX. 1995, 233–236.

[5] WU, H.–SVOBODA, M. D.–HAYES, M. D.–WILHITE, D. A.–WEN, F.: Appropriate application of the Standardized Precipitation Index in arid locations and dry seasons. *International. Journal of Climatology*, Volume 27. 2007, 65–79.

[6] HAYES, M. J.–SVOBODA, M. D.–WILHITE, D. A.–VANYARKHO, O. V.: Monitoring the 1996 drought using the standardized precipitation index. *Bulletin of the American Meteorological Society,* 80. 1999, 429–438.

[7] SEILER, R. A.–HAYES, M.–BRESSAN, L.: Using the Standardized Precipitation Index for Flood Risk Monitoring. *International Journal of Climatology*, Volume 22. 2002, 1365–1376.

[8] WU, H.–HAYES, M.–WEISS, A.–HU, Q.: An evaluation of the Standardized Precipitation Index, China-Z Index, and statistical Z-Score. *International Journal of Climatology, Volume* 21. 2001, 745–758.

[9] EDWARDS, D. C.–MCKEE, T. B.: Characteristics of 20th century drought in the United States at multiple timescales. *Climatology Rep*. 97–2, Department of Atmospheric Science, Colorado State University, Fort Collins, Colorado. 1997.
[10] CANCELLIERE, A.–DI MAURO, G.–BONACCORSO, B.–ROSSI, G.: Drought forecasting using the Standardized Precipitation Index. *Water Resources Management*, 21(5). 2007, 801–819.

Geosciences and Engineering, Vol. 2, No. 4 (2013), pp 81–92.

DIFFERENTIAL EQUATIONS AND COMPARISON OF FEM TE AND TM MODE WITH CONDUCTIVITY ANISOTROPY

GÁBOR PETHŐ

Department of Geophysics, University of Miskolc
H-3515 Miskolc- Egyetemváros
gfpg@uni-miskolc.hu

1. Abstract

Assuming conductivity anisotropy the basic relationships are derived for frequency domain electromagnetic (FEM) TE (E polarization) and TM mode (H polarization) for the 2D (two-dimensional) and the 2.5D situations. In the course of the anisotropy investigation presented here the principal directions of conductivity tensor are parallel to the main structural strike directions of the elongated conductivity structure. For the anisotropic case of 2D MT (magnetotellurics) it is proved that independent of the angle of the incident plane wave the EM field can be decomposed for two polarizations, just like in the case of 2D MT isotropic situation. For this reason the two polarizations can be treated mathematically separately. In the 2D MT TE (E polarization) mode partial differential equation the strike directional field component is the unknown and the strike directional conductivity value controls the effect of anisotropy. In the 2D MT TM (H polarization) mode the strike directional magnetic field component is the unknown and the conductivities in dip and the vertical direction control the effect of anisotropy. The 2.5D anisotropic FEM problem is solved in the strike directional wave number domain and from the Fourier transforms of the Maxwell's equations coupled partial differential equations are derived for the two polarizations. The unknowns of the differential equations are the Fourier transforms of the strike directional electric and magnetic field components. Due to the differential equation systems the two modes are coupled and the anisotropy effect is controlled by the three principal values of conductivity tensor. Approaching the theoretical far field zone similarity can be observed between the controlled and the plane wave source methods in the point of view of anisotropy effect as well.

***Keywords**:* conductivity anisotropy, frequency domain electromagnetics, plane wave source, controlled source, E polarization, H polarization, wave number domain

2. Introduction

The geophysical electromagnetic methods apply either natural or artificial source(s) [1, 2]. If the investigated conductivity structure is elongated and the source field is due to EM plane waves, just like in the magnetotellurics, we encounter with a pure 2D MT problem. Generally, the conductivity structures are anisotropic 3D ones and the 2D assumption is a theoretical approach. However, we frequently encounter with partially elongated conductivity structures, which are far from being 1D, they are practically 3D, but they can be approximated by 2D structures at least in the middle 1/3 part of the structure. For isotropic 2D MT it was proved ([1, 2]) that the E- and H polarization can be treated separately [1, 2]. If the source is an electric dipole source, the problem to be solved is a 3D one. There is a special situation for a 2D structure when it is exited by an electric dipole which can be approximated mathematically as a point source. If we encounter a 2D model which is exited by a point source the situation is called as a 2.5D problem. Just like in MT in the course of EM investigation on elongated conductivity structures exited by electric

dipole source special emphasis has to be put on the two modes. Distinction is made between TE mode, when the electric source is parallel to the structural strike, and TM mode, when the electric source is perpendicular to it. Assuming elongated isotropic conductivity inhomogeneities exited by electric dipole source the partial differential equations were presented by Pethő [3] and besides the investigation of some effects different numerical model studies were also carried out [4], [5], [6], [7], [8] and [9]. For anisotropic case differential equations were provided in [10] and [11], however, difference was made only between the conductivity values parallel to the horizontal layering and perpendicular to it. In this paper the principle directions of the conductivity tensor are parallel to the main structural direction of the 2D structure. The partial differential equations for the 2D situation with conductivity anisotropy are derived. This situation practically corresponds to MT (Magnetotellurics) and VLF (Very Low Frequency). The latter method was also applied in the CRITICEL project [12], and it is obvious that the geological structures investigated there were rather anisotropic than isotropic ones. The type of the conductivity anisotropy assumed here is far from being the general one, however, it may occur that one geoelectric domain in the inhomogeneous half-space can be characterized by this kind of anisotropy and this strongly anisotropic domain is embedded into homogeneous isotropic (layered) half-space or 2D isotropic host. For the 2.5D situation with conductivity anisotropy partial differential equation systems are derived. The similarities and differences between the two cases (2D and 2.5D) will be also provided putting emphasis on the effect of anisotropy.

2. 2D MT problem for anisotropic case

In geophysical EM exploration the basic relationships governing the electromagnetic phenomenon are the Maxwell's equations with the constitutive equations. One Maxwell's equation represents the physical law that electric fields result from time-varying magnetic induction:

$$rot\vec{E} = -\partial\vec{B}/\partial t \tag{1}$$

The next Maxwell's equation expresses the fact that the magnetic fields are caused by displacement and conduction current flows. In geophysical practice conduction current is dominant over displacement current (high-frequency georadar can be regarded as an exception), for this reason displacement current can be neglected:

$$rot\vec{H} = \vec{i} = [\sigma]\vec{E} \tag{2}$$

In order to have relationship between electromagnetic fields and subsurface conductivity the introduction of Ohm's law is required. Generally, the conductivity determining the relationship between the current density vector and the electric field vector must be a tensor (it is a scalar quantity only for an isotropic case). The conductivity tensor has a simple form if two of the orthogonal coordinate directions are selected to lie in the direction of maximum conductivity and the third one into the minimum conductivity. If the principal directions of the conductivity tensors coincide with the strike, dip and vertical directions the off-diagonal terms are zero based upon [13, 14]. In this point we remark that the anisotropy discussed in this paper is not a general treatment, we consider the situation when the principle directions of the conductivity tensor are parallel to the main structural

directions of the 2D structure. We assume σ_x conductivity in the strike direction of *x*, σ_y conductivity along y, and σ_z conductivity value in the *z* direction.

$$\sigma = \begin{vmatrix} \sigma_{xx} & 0 & 0 \\ 0 & \sigma_{yy} & 0 \\ 0 & 0 & \sigma_{zz} \end{vmatrix} = \begin{vmatrix} \sigma_x & 0 & 0 \\ 0 & \sigma_y & 0 \\ 0 & 0 & \sigma_z \end{vmatrix} \tag{3}$$

Assuming an $e^{j\omega t}$ time dependent plane wave source and due to the 2D assumption all partial derivatives with respect strike direction (*x*) must be zero in (1):

$$\frac{\partial E_z}{\partial y} - \frac{\partial E_y}{\partial z} = -j\omega\mu H_x \tag{4}$$

$$\frac{\partial E_x}{\partial z} = -j\omega\mu H_y \tag{5}$$

$$\frac{\partial E_x}{\partial y} = j\omega\mu H_z \tag{6}$$

If we write the component equations of (2), we take into account the conductivity tensor given by (3) and the simplification coming from the zero value of the partial derivatives with respect the strike direction:

$$\frac{\partial H_z}{\partial y} - \frac{\partial H_y}{\partial z} = \sigma_x E_x \tag{7}$$

$$\frac{\partial H_x}{\partial z} = \sigma_y E_y \tag{8}$$

$$-\frac{\partial H_x}{\partial y} = \sigma_z E_z \tag{9}$$

Just like for isotropic 2D MT, there are two independent equation systems. One group consists of equation (4), (8), (9), in which only the strike directional magnetic field component and the non-strike directional electric field components are. This mode is called H-polarization or TM mode. The strike directional magnetic field component is the unknown in the second order partial differential equation, which is the densest form of H-polarization:

$$\frac{1}{\sigma_z}\frac{\partial^2 H_x}{\partial y^2} + \frac{1}{\sigma_y}\frac{\partial^2 H_x}{\partial z^2} = j\omega\mu H_x \tag{10}$$

The difference between the isotropic and anisotropic 2D TM modes is obvious: in isotropic case the strike directional magnetic field component depends on the scalar

conductivity value and in the anisotropic situation the strike directional magnetic field component depends on both non-strike directional conductivity values.

In the other group of component equations – consisting of (5), (6) and (7) – the strike directional electric field component and the non-strike directional magnetic field components can be found. Substituting the value of magnetic field components from (5) and (6) into (7), we receive the E-polarization or TE mode. Similar second order partial differential equation can be derived as (10):

$$\frac{\partial^2 E_x}{\partial y^2} + \frac{\partial^2 E_x}{\partial z^2} = j\omega\mu\sigma_x E_x \tag{11}$$

We call the attention for the difference between the 2D TE modes for the anisotropic and isotropic situations: here the strike directional conductivity value, in the isotropic case the scalar conductivity value determines the strike directional electric field component of the second order partial differential equation.

3. 2.5D FEM problem in wave number domain for anisotropic case

3.1. Basic equations

Just like in the case of MT, emphasis is put the Maxwell's equations in the controlled source frequency domain electromagnetic methods. The equation (1) is used in an unchanged form:

$$rot\vec{E} = -\partial\vec{B}/\partial t$$

$\vec{i}_s = Id\vec{s}\,\delta(\vec{r})$ makes possible a point source approximation. An $e^{j\omega t}$ time dependent source term is assumed. Involving it into the other Maxwell's equation of (2):

$$rot\vec{H} = \vec{i} + \vec{i}_s \tag{12}$$

It represents the physical law that the magnetic fields are caused by conduction and source currents. The effect of displacement currents in the second equation was not taken into account.

For 2.5D FEM forward modeling with magnetic sources Stoyer and Greenfield recommended that the solution of the original 3D problem could be replaced by the series of solutions of 2D problem in the k_x wave number domain [15]. To follow this procedure the Maxwell's equations (1) and (2) are Fourier-transformed. The Fourier transformation can be expressed as:

$$\hat{F}(k_x, y, z) = \int_{-\infty}^{\infty} F(x, y, z) e^{-jk_x x} dx \tag{13}$$

To determine the Fourier transforms of the Maxwell's equations the partial derivative of the EM field components with respect the strike direction (x) is also needed:

$$\int_{-\infty}^{\infty} \frac{\partial F(x, y, z)}{\partial x} e^{-jk_x x} dx = \left[F(x, y, z) e^{-jk_x x} \right]_{-\infty}^{+\infty} + jk_x \int_{-\infty}^{\infty} F(x, y, z) e^{-jk_x x} dx = jk_x \hat{F}(k_x, y, z) \tag{14}$$

In (14) equation if x tends to either $+\infty$ or $-\infty$ then any field component approximates zero due to the finite energy of the source, for this reason the value of expression in brackets must be zero. For this reason the partial derivative of any EM field components with respect the strike direction is proportional the Fourier transform of the component itself. Taking into account this fact and the harmonic time dependence of EM fields as well, the Fourier transforms of Maxwell's equation (1) in terms of component equations can be detailed as follows:

$$\frac{\partial \hat{E}_z}{\partial y} - \frac{\partial \hat{E}_y}{\partial z} = -j\omega\mu\hat{H}_x \tag{15}$$

$$\frac{\partial \hat{E}_x}{\partial z} - jk_x\hat{E}_z = -j\omega\mu\hat{H}_y \tag{16}$$

$$jk_x\hat{E}_y - \frac{\partial \hat{E}_x}{\partial y} = -j\omega\mu\hat{H}_z \tag{17}$$

Due to the TM and TE mode, we have to assume that only horizontal electric dipole source (either in x or y direction) is applied. For these situations we can rewrite the Fourier transforms of (12) as:

$$\frac{\partial \hat{H}_z}{\partial y} - \frac{\partial \hat{H}_y}{\partial z} = \sigma_x\hat{E}_x + \hat{i}_{sx} \tag{18}$$

$$\frac{\partial \hat{H}_x}{\partial z} - jk_x\hat{H}_z = \sigma_y\hat{E}_y + \hat{i}_{sy} \tag{19}$$

$$jk_x\hat{H}_y - \frac{\partial \hat{H}_x}{\partial y} = \sigma_z\hat{E}_z \tag{20}$$

As it was mentioned, the effect of displacement current was abandoned, and for this reason in the isotropic case the complex wave number (k) can be expressed as $k^2 = -j\omega\mu\sigma$. Due to the anisotropy we introduce the complex wave number in the y and z directions as $k_y{}^2 = -j\omega\mu\sigma_y$ and $k_z{}^2 = -j\omega\mu\sigma_z$ it is not necessary to introduce the complex wave number in the strike direction; kx has denoted the strike directional wave number, introduced by the transformation of (14).

The aim of the following derivation is to yield partial differential equation systems with equations containing only strike direction EM field components in the wave number (k_x) domain. The first partial differential equation system will describe the situation when the electric dipole source is parallel to the structural strike direction. Another partial differential equation system is valid for the situation when the source term is perpendicular to the structural strike. From equations (16) and (20) $j\hat{H}_y$ can be expressed and taking them to be equal we obtain:

$$\sigma_z(1-k_x^2/k_z^2)\hat{E}_z=-\frac{\partial\hat{H}_x}{\partial y}-\frac{k_x}{\omega\mu}\frac{\partial\hat{E}_x}{\partial z} \tag{21}$$

With the notation of

$$q_z=1/(1-k_x^2/k_z^2) \tag{22}$$

and with the application of the resistivity instead of conductivity from (21) we receive

$$\hat{E}_z=-\rho_z q_z\frac{\partial\hat{H}_x}{\partial y}-\frac{k_x\rho_z q_z}{\omega\mu}\frac{\partial\hat{E}_x}{\partial z} \tag{23}$$

From equations (17) and (19) $j\hat{H}_z$ can be determined and taking them to be equal we obtain:

$$-\sigma_y(1-k_x^2/k_y^2)\hat{E}_y=-\frac{\partial\hat{H}_x}{\partial z}+\frac{k_x}{\omega\mu}\frac{\partial\hat{E}_x}{\partial y}+\hat{i}_{sy} \tag{24}$$

If we apply the resistivity instead of the conductivity in (24) and introduce (25) it follows:

$$q_y=1/(1-k_x^2/k_y^2) \tag{25}$$

$$\hat{E}_y=\rho_y q_y\frac{\partial\hat{H}_x}{\partial z}-\frac{k_x\rho_y q_y}{\omega\mu}\frac{\partial\hat{E}_x}{\partial y}-\rho_y q_y\hat{i}_{sy} \tag{26}$$

We can receive the non-strike directional magnetic field components in the wave number domain similarly. From equations (17) and (19) $\hat{E}_y$ can be determined and we can write:

$$-j\omega\mu(1-k_x^2/k_y^2)\hat{H}_z=-\frac{\partial\hat{E}_x}{\partial y}+\frac{jk_x}{\sigma_y}\frac{\partial\hat{H}_x}{\partial z}-\frac{jk_x}{\sigma_y}\hat{i}_{sy} \tag{27}$$

From (27) $\hat{H}_z$ can be expressed:

$$\hat{H}_z=-\frac{jq_y}{\omega\mu}\frac{\partial\hat{E}_x}{\partial y}-\frac{k_x\rho_y q_y}{\omega\mu}\frac{\partial\hat{H}_x}{\partial z}+\frac{k_x\rho_y q_y}{\omega\mu}\hat{i}_{sy} \tag{28}$$

$\hat{E}_z$ can be determined from equations (16) and (20) and taking them to be equal we receive:

$$j\omega\mu(1-k_x^2/k_z^2)\hat{H}_y=-\frac{\partial\hat{E}_x}{\partial z}-\frac{jk_x}{\sigma_z}\frac{\partial\hat{H}_x}{\partial y} \tag{29}$$

From this equation $\hat{H}_y$ can be obtained:

$$\hat{H}_y=\frac{jq_z}{\omega\mu}\frac{\partial\hat{E}_x}{\partial z}-\frac{k_x\rho_z q_z}{\omega\mu}\frac{\partial\hat{H}_x}{\partial y} \tag{30}$$

3.2. Partial differential equation systems for TE and TM mode of the 2.5D case

The ***TE mode*** is the case when there is only an electric dipole source with strike direction. Substituting equations (28) and (30) into (18) with the assumption of $\hat{i}_{sy}=0$ in (28) we obtain (31). The other equation for the TE mode is (32) which can be derived by the substitution of (23) and (26) into equation (15) with the assumption of $\hat{i}_{sy}=0$ in equation of (26):

$$\frac{j}{\omega\mu}\frac{\partial}{\partial y}\left(q_y\frac{\partial\hat{E}_x}{\partial y}\right)+\frac{k_x}{\omega\mu}\frac{\partial}{\partial y}\left(\rho_y q_y\frac{\partial\hat{H}_x}{\partial z}\right)+\frac{j}{\omega\mu}\frac{\partial}{\partial z}\left(q_z\frac{\partial\hat{E}_x}{\partial z}\right)-\frac{k_x}{\omega\mu}\frac{\partial}{\partial z}\left(\rho_z q_z\frac{\partial\hat{H}_x}{\partial y}\right)+\sigma_x\hat{E}_x=-\hat{i}_{sx} \tag{31}$$

$$\frac{\partial}{\partial y}\left(\rho_z q_z\frac{\partial\hat{H}_x}{\partial y}\right)+\frac{k_x}{\omega\mu}\frac{\partial}{\partial y}\left(\rho_z q_z\frac{\partial\hat{E}_x}{\partial z}\right)+\frac{\partial}{\partial z}\left(\rho_y q_y\frac{\partial\hat{H}_x}{\partial z}\right)-\frac{k_x}{\omega\mu}\frac{\partial}{\partial z}\left(\rho_y q_y\frac{\partial\hat{E}_x}{\partial y}\right)-j\omega\mu\hat{H}_x=0 \tag{32}$$

In the ***TM mode*** the electric dipole source is perpendicular to the structural strike. In order to receive the TM mode equations similar steps are required as we applied in the TE mode. In this case $\hat{i}_{sx}=0$ in (18) and $\hat{i}_{sy}\neq 0$ in (28). Substituting (28) and (30) into (18) we obtain equation (33). The second TM mode equation is (34). It can be derived by the substitution of equations (23) and (26) into equation (15):

$$\frac{j}{\omega\mu}\frac{\partial}{\partial y}\left(q_y\frac{\partial\hat{E}_x}{\partial y}\right)+\frac{k_x}{\omega\mu}\frac{\partial}{\partial y}\left(\rho_y q_y\frac{\partial\hat{H}_x}{\partial z}\right)+\frac{j}{\omega\mu}\frac{\partial}{\partial z}\left(q_z\frac{\partial\hat{E}_x}{\partial z}\right)-\frac{k_x}{\omega\mu}\frac{\partial}{\partial z}\left(\rho_z q_z\frac{\partial\hat{H}_x}{\partial y}\right)+\sigma_x\hat{E}_x=\frac{k_x}{\omega\mu}\frac{\partial}{\partial y}\rho_y q_y\hat{i}_{sy} \tag{33}$$

$$\frac{\partial}{\partial y}\left(\rho_z q_z\frac{\partial\hat{H}_x}{\partial y}\right)+\frac{k_x}{\omega\mu}\frac{\partial}{\partial y}\left(\rho_z q_z\frac{\partial\hat{E}_x}{\partial z}\right)+\frac{\partial}{\partial z}\left(\rho_y q_y\frac{\partial\hat{H}_x}{\partial z}\right)-\frac{k_x}{\omega\mu}\frac{\partial}{\partial z}\left(\rho_y q_y\frac{\partial\hat{E}_x}{\partial y}\right)-j\omega\mu\hat{H}_x=\frac{\partial}{\partial z}\rho_y q_y\hat{i}_{sy} \tag{34}$$

Just like in the case of isotropic 2.5D case, both modes can be described with the same partial differential equations and the differences between the modes are presented by the inhomogeneous terms on the right. The second order partial derivatives with respect to *y* or *z* can be finite differenced similarly as in the case of isotropic situation, but the terms with second order mixed partial derivatives should be transformed before they are finite differenced. For example instead of the first mixed second derivative of the strike directional Fourier magnetic field component in equation (31) or in (33) can be rewritten as:

$$\frac{k_x}{\omega\mu}\frac{\partial}{\partial y}\left(\rho_y q_y\frac{\partial\hat{H}_x}{\partial z}\right)=\frac{k_x}{\omega\mu}\frac{\partial(\rho_y q_y)}{\partial y}\frac{\partial\hat{H}_x}{\partial z}+\frac{k_x\rho_y q_y}{\omega\mu}\frac{\partial^2\hat{H}_x}{\partial y\partial z} \tag{35}$$

The next mixed second order partial derivative of the strike directional Fourier magnetic field components in (31) or in (33) can be transformed similarly:

$$\frac{k_x}{\omega\mu}\frac{\partial}{\partial z}\left(\rho_z q_z \frac{\partial \hat{H}_x}{\partial y}\right) = \frac{k_x}{\omega\mu}\frac{\partial(\rho_z q_z)}{\partial z}\frac{\partial \hat{H}_x}{\partial y} + \frac{k_x \rho_z q_z}{\omega\mu}\frac{\partial^2 \hat{H}_x}{\partial y \partial z} \tag{36}$$

Except for the coefficient of the strike directional Fourier magnetic field component in (32) or in (34) all coefficients on the left hand sides reflect the effect of anisotropy. The effect of anisotropy can be observed even in the inhomogeneous terms in equations of (33) and (34) in the TM mode. The latter statement does not hold for the TE mode. In contrast with the isotropic situation [3], second order mixed partial derivatives of the strike directional Fourier EM field components are in the anisotropic case.

3.3. Determination of spatial solutions

In order to obtain space-domain solution from the solution received in the strike-directional wave numer domain, inverse Fourier transforms have to be applied. The relationship resulting in space-domain solution from the wave number domain is as follows:

$$F(x,y,z) = \frac{1}{2\pi}\int_{-\infty}^{\infty} \hat{F}(k_x,y,z)e^{jk_x x}dk_x \tag{37}$$

For the ***TE mode*** it can be proved [3] that in broadside configuration only E_x, H_y, H_z components are different from zero. By inverse transform of (37) for the vertical plane containing the source (x=0) the strike directional electric field component for any point can be received as:

$$E_x(0,y,z) = \frac{1}{\pi}\int_0^{\infty} \hat{E}_x(k_x,y,z)\,dk_x \tag{38}$$

The non-strike directional magnetic field components can be determined from equations (30) and (28) with the assumption of source free terms. For the vertical plane containing the source (x=0) the spatial magnetic components can be gained based upon equation (37):

$$H_y(0,y,z) = \frac{1}{\pi}\int_0^{\infty}\left[\frac{jq_z}{\omega\mu}\frac{\partial \hat{E}_x}{\partial z} - \frac{k_x\rho_z q_z}{\omega\mu}\frac{\partial \hat{H}_x}{\partial y}\right]dk_x \tag{39}$$

$$H_z(0,y,z) = -\frac{1}{\pi}\int_0^{\infty}\left[\frac{jq_y}{\omega\mu}\frac{\partial \hat{E}_x}{\partial y} + \frac{k_x\rho_y q_y}{\omega\mu}\frac{\partial \hat{H}_x}{\partial z}\right]dk_x \tag{40}$$

For the ***TM mode*** in collinear configuration the following three electromagnetic field components - E_y, E_z, H_x - are not zero and they can similarly be expressed as the other three field components for TE mode. The expression for the strike directional magnetic field component is an inverse Fourier-transform of the wave number solution:

$$H_x(0,y,z) = \frac{1}{\pi}\int_0^{\infty} \hat{H}_x(k_x,y,z)\,dk_x \tag{41}$$

With the assumption of source free region and with the application of (37), the Fourier-transform of non-strike directional electric field components can be determined from (26) and (23)

$$E_y(0,y,z)=\frac{1}{\pi}\int_0^{\infty}\left[\ \rho_y q_y\frac{\partial\hat{H}_x}{\partial z}-\frac{k_x\rho_y q_y}{\omega\mu}\frac{\partial\hat{E}_x}{\partial y}\ \right]dk_x \tag{42}$$

$$E_z(0,y,z)=-\frac{1}{\pi}\int_0^{\infty}\left[\ \rho_z q_z\frac{\partial\hat{H}_x}{\partial y}+\frac{k_x\rho_z q_z}{\omega\mu}\frac{\partial\hat{E}_x}{\partial z}\ \right]dk_x \tag{43}$$

It can be noted that there is no difference between the inverse Fourier formulae of the strike directional EM field components valid for the anisotropic (38), (41) and the isotropic case [3]. At the same time in the course of the determination of the secondary EM field components additional anisotropy effect is superimposed to the primary EM field components. For this special case of anisotropy the conductivity perpendicular to the strike and the conductivity value in the z direction have effect on the secondary EM field components (39), (40), (42), (43).

4. Comparison between FEM 2D and 2.5D equations in the point of view of conductivity anisotropy

In the 2.5D FEM there are two unknowns in the two coupled equations, they are the Fourier transforms of the strike directional electric and magnetic field components. Due to the differential equation systems (consisting of (31) and (32) or (33) and (34)) there are neither pure TE nor TM mode, i.e. the two modes are coupled. the three anisotropy values have effect on the strike directional EM field components. The anisotropy effect is controlled by the three principal values of conductivity in both modes, i.e. the three anisotropy values have effect on the strike directional EM field components. For isotropic case the partial differential equations do not contain mixed second order derivatives and one geoelectric domain can be characterized by a constant electrical conductivity value.

In 2D MT it is equation (11) which governs the TE mode EM fields' behaviors. In the TE mode partial differential equation the strike directional electric field component is the only unknown and the strike directional conductivity value controls the effect of anisotropy. In the geophysical EM special emphasis is put on CSAMT (Controlled Source Audio Magnetotellurics) and VLF (Very Low Frequency) methods, both are working in the far-field zone. The theoretical far field zone (corresponding to MT) is presented from these equations if $k_x = 0$. For this strike directional wave number value $q_z = q_y = 1$ and assuming $\hat{i}_{sy}=0$ in (31) we can easily receive from (31):

$$\frac{\partial}{\partial y}\left(\frac{\partial\hat{E}_x}{\partial y}\right)+\frac{\partial}{\partial z}\left(\frac{\partial\hat{E}_x}{\partial z}\right)=j\omega\mu\sigma_x\hat{E}_x \tag{44}$$

The similarity between (11) and (44) is obvious. We can state that if we approach the theoretical far field zone, not only the coupling has been ceased, but the effect of the non-strike directional conductivities can be abandoned as well. Taking into account that the second term of integrand is zero and $q_z = q_y = 1$ in equations (39) and (40), we receive

similar physical relationship for the non strike directional magnetic field components of TE mode as we can have from (5)

$$H_y = \frac{j}{\omega\mu}\frac{\partial E_x}{\partial z} \tag{45}$$

and from (6):

$$H_z = -\frac{j}{\omega\mu}\frac{\partial E_x}{\partial y} \tag{46}$$

As for the 2.5D theoretical far field TM mode approximation is concerned instead of (32) -with the same assumption as we applied in the case of TE mode- we can write:

$$\frac{\partial}{\partial y}\left(\rho_z \frac{\partial \hat{H}_x}{\partial y}\right) + \frac{\partial}{\partial z}\left(\rho_y \frac{\partial \hat{H}_x}{\partial z}\right) = j\omega\mu\hat{H}_x \tag{47}$$

We can state that if we approach the theoretical far field zone over a 2D anisotropic conductivity structure in the TM mode, the effect of the non strike directional conductivity is dominant over that of the strike directional conductivity (i.e. the conductivities in dip and the vertical direction control the effect of anisotropy). In this zone the similarity between the controlled source and MT non strike directional electric field components is obvious.
In order to make comparison between them from (8)

$$E_y = \rho_y \frac{\partial H_x}{\partial z} \tag{48}$$

and from (9):

$$E_z = -\rho_z \frac{\partial H_x}{\partial y} \tag{49}$$

Because the second term of integrand is zero and $q_z = q_y = 1$ in equations (42) and (43), we received similar relationship for the non-strike directional electric field components of the TM mode for the two cases.

5. Summary

The effect of anisotropy cannot be abandoned in the course of EM exploration. In the paper the basic equations were derived for elongated anisotropic conductivity structures exited by plane wave and electric dipole sources (treated as point sources, with either in strike or dip direction). Based upon these equations only after the discretization of them it is possible to model the EM responses over some groups of frequency domain electromagnetic methods.

It was proven that in the 2D MT TE (E polarization) mode partial differential equation the strike directional field component is the unknown and the strike directional conductivity value controls the effect of anisotropy. Similarly, in the 2D MT TM (H polarization) mode equation the strike directional magnetic field component is the unknown and the conductivities in dip and the vertical direction control the effect of anisotropy. In the course of the 2.5D anisotropic FEM problem two partial differential equations in the strike

directional wave number domain were derived and the two polarizations can be distinguished by the inhomogeneous terms. The form of the coupled partial differential equations is more complex than for isotropic case because of the presence of the second order mixed partial derivatives. The unknowns of the differential equations are the Fourier transforms of the strike directional electric and magnetic field components and in contrast with anisotropic 2D MT they are simultaneously controlled by the three principal values of the conductivity tensor. In general case - including the transition zone- additional anisotropy effect (except the effect of the strike directional conductivity) is superimposed when the secondary EM field components are determined. Approaching the theoretical far field zone similarity can be observed between the EM field components obtained by the controlled and the plane wave source methods in the point of view of anisotropy effect.

6. Nomenclature

$\vec{B}$: magnetic flux density (Wb/m^2)
$d\vec{s}$: elementary dipole length (m)
$\vec{E}$: electric field vector (V/m)
F: EM component (V/m, or A/m)
$\hat{F}$: Fourier-transform of the F EM component (V/m, or A/m)
$\vec{H}$: magnetic field vector (A/m)
I: transmitter current (A)
$\vec{i}$: current density vector (A/m^2)
$\vec{i}_s$: applied current source (A/m^2)
j: $\sqrt{-1}$
x: strike direction
k: complex wave number (1/m)
k_x: wavenumber in the strike direction (1/m)
p: skin depth (m)
q_z: derived dimensionless parameters (subscript z refers to vertical)
q_y: derived dimensionless parameters (subscript y refers direction perpendicular to the structural strike)
r: transmitter-receiver separation, distance (m)
t: time (s)
$\delta(r)$: Dirac-delta function
ε: dielectric constant (F/m)
μ: magnetic permeability (H/m)
ρ: resistivity (ohmm)
σ: conductivity (mho/m or S/m)
ω: angular frequency of the EM field (Hz)

7. Acknowledgement:

The described work was carried out as part of the TÁMOP-4.2.2.A-11/1/KONV -2012-0005 project as a work of Center of Excellence of Sustainable

Resource Management, in the framework of the New Széchenyi Plan. The realization of this project is supported by the European Union, cofinanced by the European Social Fund.

8. References

[1] TAKÁCS, E.: *Geophysics, Geoelectrical exploration methods I.–II.* (in Hungarian), Budapest, Tankönyvkiadó, 1981.

[2] NABIGHIEN, M. N.: *Electromagnetic methods in applied geophysics*. Vol. 2, Application, Parts A and B, Tulsa, SEG, 1992.

[3] PETHŐ, G.: *FEM numerical modeling of 2D structures exited by electrical dipole source*. (in Hungarian, thesis for Candidate of Science degree), Miskolc, 1993.

[4] PETHŐ, G.: CSAMT Numerical Modelling for 2D Thermal EOR Monitoring. *EAPG-6th Conference and Technical Exhibition Extended Abstracts of Papers*, P547, Vienna, 1994.

[5] PETHŐ, G.–KAIKKONEN, P.–VANYAN, L. L.: Numerical modelling for the effect of a 2-D seafloor trench on sea-bottom EM measurements using horizontal electric dipole sources. *Geophysica*, Vol. 31, 1995, 1–21.

[6] PETHŐ, G.–KAIKKONEN, P.–VANYAN, L. L.: Frequency domain electromagnetic source polarization investigation in case of a 2-D seafloor trench. *Aarhus, 3rd European Environmental and Engineering Geophysics Conference, Section New Developments*, 1997, 323–326.

[7] PETHŐ, G.–FICSÓR, L.: Distortion effect of elongated surface conductivity-inhomogeneities on CSAMT measurements. *14th Workshop on EM induction in the Earth*, Book of Abstract, p. 100, Sinaia, 1998.

[8] PETHŐ, G., FICSÓR, L.: Source polarization effect in case of elongated surface inhomogeneities covering transition zone. *EAGE 63rd Conference & Technical exhibition, Abstract* II, P050, Amsterdam, 2001.

[9] PETHŐ, G.: FEM source effect investigation with 2.5D numerical modeling. *15th European Meeting of Environmental and Engineering Geophysics*, Near Surface Proceedings & Exhibitors'Cataloge, P59, Dublin, 2009.

[10] PETHŐ, G.: *Differential equations of FEM using electric dipole source for elongated structures with conductivity anisotropy*. Kutatás és Innováció a Magyar Geotermiában, konferencia kiadvány, pp.70–86. , Miskolc, 2012.

[11] PETHŐ, G.: Bases of FD modeling for EM underground transillumination with vertical electric dipoles in 2D anisotropic conductivity structures. Geosciences and Engineering. Vol. 2 (2013), No. 3, pp. 51–62.

[12] PETHŐ, G.–ORMOS, T.–TURAI, E.–SZABÓ, N.–BULLA, D.–NÉMETH, N.–ZERGI, I.–BENŐ, D.–KOCSIS, S.: Geophysical measurements in the vicinity of Bükkszentkereszt. (in Hungarian), Bányászati és Kohászati Lapok- Bányászat, Vol. 146 (2013) No. 5–6, pp. 39–47.

[13] KELLER, G. V.: Rock and Mineral Properties. in: Nabighien, M. N.: *Electromagnetic methods in applied geophysics*. Vol. 1, Theory, Tulsa, SEG, 1992.

[14] NEGI, J. G.–SARAF, P. D.: Anisotropy in geoelectromagnetism. *Methods in geochemistry and geophysics*, 28, Elsevier, 1989.

[15] STOYER, C. H.–GREENFIELD, R. J.: Numerical solutions of the response of a two-dimensional earth to an oscillating magnetic dipole source. *Geophysics*, 41, 1976, 519–530.

Geosciences and Engineering, Vol. 2, No. 4 (2013), pp 93–101.

DETERMINING THE FAILURE ENVELOPE OF THE INTACT GRANITIC ROCKS FROM BÁTAAPÁTI

BALÁZS VÁSÁRHELYI[1]–LÁSZLÓ KOVÁCS[2]–BOGLÁRKA KOVÁCS[2]

[1]: Department of Structural Engineering, University of Pécs, 7624 Pécs
vasarhelyib@gmail.com
[2]: Kőmérő (RockStudy) Ltd.; 7633 Pécs
kovacslaszlo@komero.hu; kovacsboglarka@komero.hu

1. Abstract

The failure envelope of the rock mass is one of the most important mechanical information for designing in or on rock. This mechanical parameter can be calculated from the quality of the rock mass (i.e. value of the rock mass classification) and from the failure envelope of the intact rock. The latter can be determined by laboratory tests which are usually very expensive and time consuming. The goal of this paper is to present the laboratory results of the failure envelope determination of the intact rock measured by using Multiplied Failure State (MFS) triaxial tests for different granitic rock samples from National Radioactive Waste Landfill (NRWR) at Bátaapáti. While designing the access tunnels and landfill chambers it is very important to know the exact failure of the different granitic rock types. The mechanical parameters of different granitic rock types are compared, as well, in this paper.

2. Traditional method for determining the failure envelope of intact rock

It is well known that the failure envelope of rock mass is highly sensitive to the rock mechanical parameters of intact rock. It means that the determination of the exact failure envelope of intact rocks is one of the most important among the other laboratory measurements. The first triaxial test for calculating the failure envelope of the intact rock was developed by KÁRMÁN [1] and his results were recently re-calculated [2, 3]. The basic concept of this method is that the failure of the rock was measured by using each time different confining pressure and the axial stresses were determined at the failure. This method was exactly defined by the early version of suggested methods by the International Society for Rock Mechanics [4]. It can be seen, that minimum 4 intact rock samples with the same quality are necessary for getting only one result. This method is also very time consuming and very expensive. Firstly this method was used to determine the mechanical parameters of the Mórágy rock formations for rock engineering design in Bátaapáti.

Unfortunately, there were not enough intact rock samples from the different rock types of the Mórágy Granite Formation: due to the influences of the micro-tectonics, several micro-ruptures are in the "relative" intact rocks. Using the traditional method, minimum 20 samples were necessary for calculating only one failure envelope of the Mórágy Granite. For the first time in the world Computer Tomography (CT) investigations were also carried out before any laboratory investigations. Using this method a lot of micro-cracks and different tectonic influences could be shown. Their variety was so high and their presence was sometimes random therefore basically it was not possible to collect specimens with properly the same quality (to compose a correct group) for an exact intact rock tests.

It means that the laboratory results had a not determinable error although the triaxial tests – as we mentioned – were very time consuming and expensive.

3. Using special triaxial test for determining the failure envelope of intact rock

Due to the above mentioned problems, Kovári and his colleagues developed a new method for determining the failure envelope of the intact rock, using only one sample. Firstly the Multiplied Failure State – MFS triaxial test was developed [5], later the Continuous Failure State – CFS [6] was published. Finally, these methods were suggested by the International Society for Rock Mechanics (ISRM) for determining the exact failure criteria of the rock [7], and they were published in Hungary, as well [8]. Recently these methods are used worldwide, and in the University of Miskolc, as well [9].

The basic concept of the Multiple Failure State (MFS) test is to put the cylindrical rock sample into biaxial cell, using $p_0 > 0$ constant confining pressure, while the axial stress (σ_1) and strain (ε_1) are continuously controlled under constant stress rate ($\dot{\sigma}_{(t)}$ = const). This process is carried out until the sample gets close to the failure limit. At this point the confining pressure is suddenly increased with a Δp value, i.e. the intact rock becomes not in critical state due to the new (increased) confining pressure. The axial stress is increasing continuously with the constant stress rate till the next point which is near to the failure (by the given confining pressure). These cycles are repeated at least 3 times to get exact points where the intact rock fails. Of course, better results can be obtained by increasing the number of the measured failure points – in our research we used at least 5 cycles for determining the failure envelope of the investigated rock material. In Figure 1 the experimental diagrams are shown according to the publication [7].

The Continuous Failure State (CFS) test is basically the same as the MFS tests. By the first step – similarly to the above presented method – the confining pressure is constant, $p_0 > 0$, and the axial stress (σ_1) and strain (ε_1) are continuously controlled under constant stress rate ($\dot{\sigma}_{(t)}$ = const). This process is again carried out until the sample gets close to the failure limit. From this point – still using constant stress rate – the confining pressure is also increased with constant rate ($\sigma_2 = \sigma_3 = p_i$). The applied confining pressure rate should be appropriate to keep the sample near to failure state. The results of this method according [7] are shown in Figure 2.

One can see in Figures 1 and 2 that by using both MFS and CFS triaxial tests not only the failure envelope of the intact rock can be determined. Besides the failure the residual strength can be measured as well, decreasing continuously the confining pressure, under continuous axial stress rate. This residual value was not determined previously, however, it can give important information about the behavior of the rock: showing a high value in case of relatively high confining pressure.

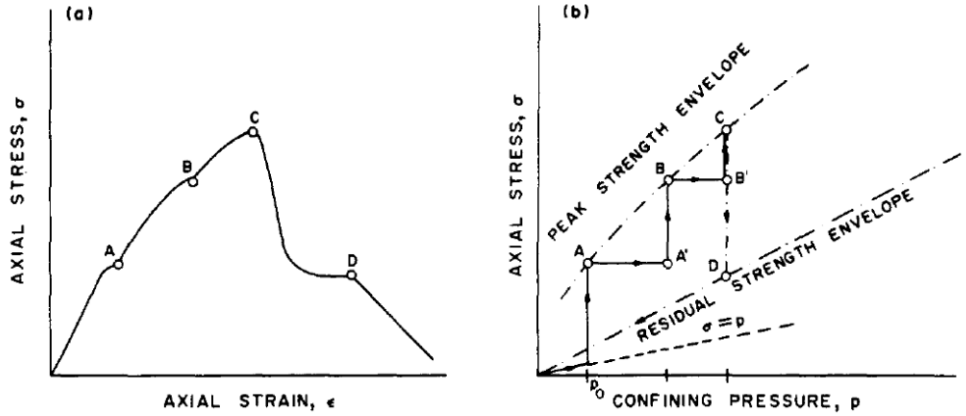

Figure 1. Multiplied failure state (MFS) triaxial test – the axial stress-axial strain curve (a), the axial stress-confining pressure curve (b)

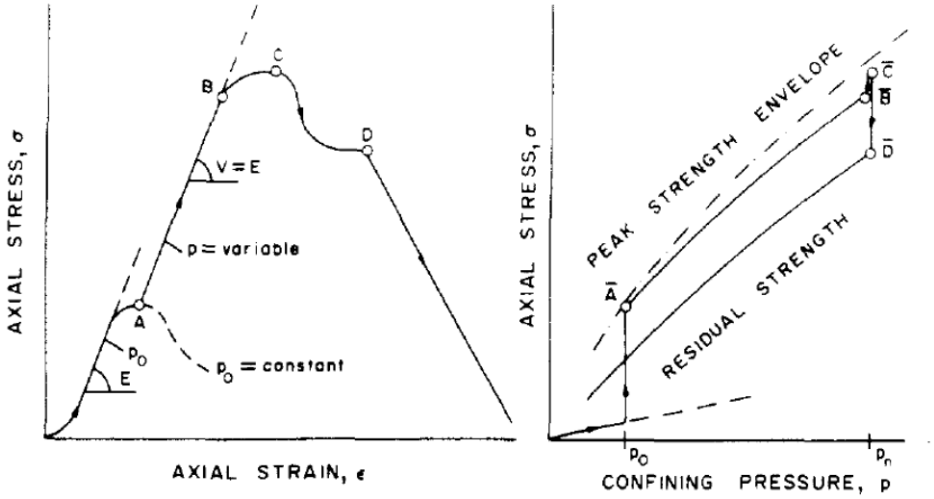

Figure 2. Continuous failure state (CFS) triaxial test – the axial stress-axial strain curve (a), the axial stress-confining pressure curve (b) [7]

The measured points were analyzed with classical Mohr–Coulomb failure envelope (both the failure and the residual results) and Hoek–Brown failure criteria (failure envelope of the intact rock). These two methods were sufficient enough for the Bátaapáti designs.

4. Development of measurement and application

Up to now, neither the MFS nor the CFS method were used in Hungary because of the lack of appropriate laboratory techniques. The RockStudy Ltd. started to develop the new laboratory test equipment at 2010. It is necessary to measure both the confining pressure and axial stress, and the axial deformation correctly.

During the development the following three main problems have to be solved: the possibility to suddenly increase the confining pressure with the necessary Δp values has to be ensured; measuring continuously both the axial and the vertical deformations is also essential for following the actual state of the rock and for determining the nearest point to the failure; for the proper intervention it is crucial to check the main parameters continuously by plotting the results in real-time.

The triaxial cell apparatus is shown in Figure 3. The applied Hoek-cell was perfectly good for carrying out the research. Knowing the brittle behavior of the granitic rock types from Mórágy, both lateral and vertical gauges were used for determining the whole deformation of the specimen. At the first time, it was not possible to determine the crack damage because of lack of these gauges: there was not any plastic behavior of the rock before the failure. Using the gauges, the failure points were exactly measured and the MFS method could be used. The measured lateral strain (ε_l), confining pressure ($\sigma_2 = \sigma_3 = p_i$) and the actual stress (σ_1) diagrams are presented in Figure 4.

In 2011 the RockStudy Ltd. carried out the complete measurement of 45 intact rock samples from different granitic rock types, such as monzogranite, monzonit, contaminated monzonit, contaminated monzogranite and aplit. Before the laboratory tests all the samples had already been analysed by CT, therefore their micro-structure was well-known.

The studied cylindrical rock samples had 1:2 diameter: height ratio, according to the suggestion of ISRM. Using MFS test method 6 cycles were applied for all the samples. At the last cycle the confining pressure was approximately 28–30 MPa ($\sigma_2 = \sigma_3$). This value is equal to the stress state at 1000–1400 m depth in the Mórágy Granit Formation, thus our results can be used for further calculations in this area. During our laboratory tests, according to Chapter 2, both the failure and the residual strength envelope were measured.

Figure 3. The triaxial test apparatus

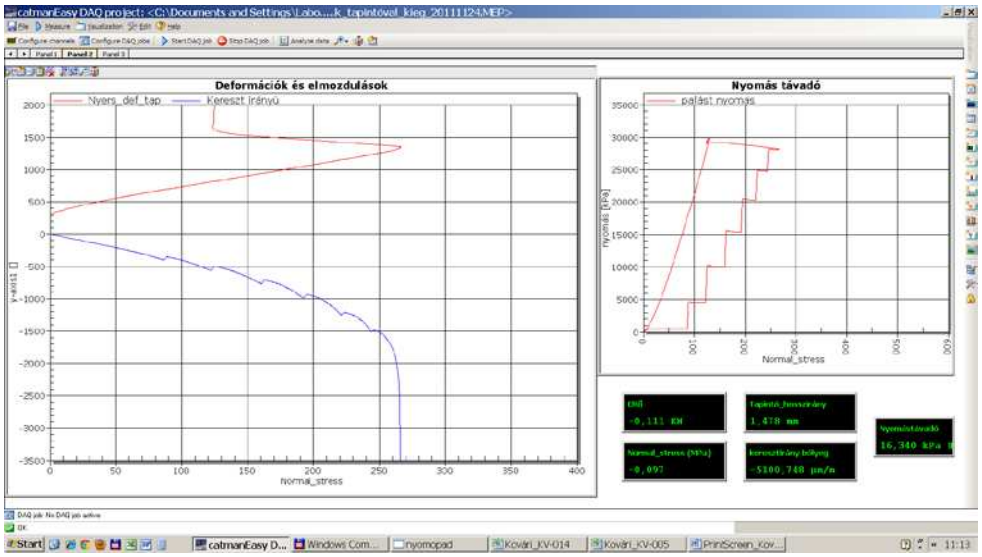

Figure 4. The plotted data during a MFS test

5. Results and discussion

For analyzing the results of the MFS tests the RocData v4.0 software (developed by Rockscinece Ltd.) was used. With this program both the Hoek–Brown and the Mohr–Coulomb failure envelope can be calculated, while in case of residual state the Mohr–Coulomb envelope was determined. On Figures. 5 and 6 the measured maximum (failure) and residual envelope are shown, respectively.

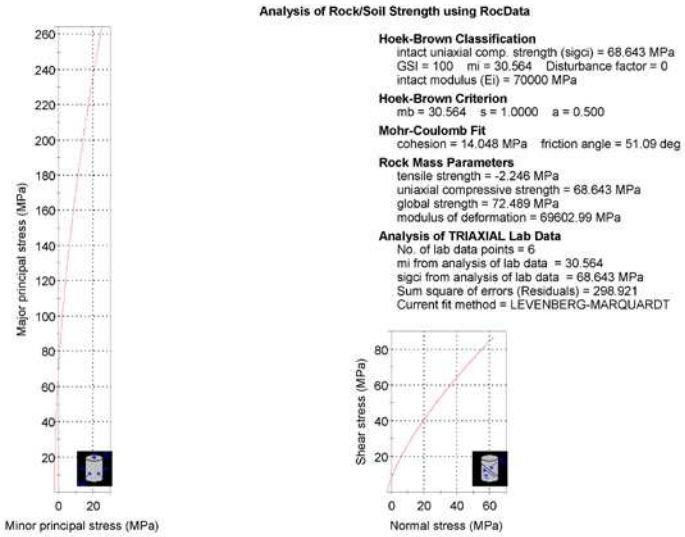

Figure 5. Determining the failure envelope of the intact rock specimen using RocData v.4.0

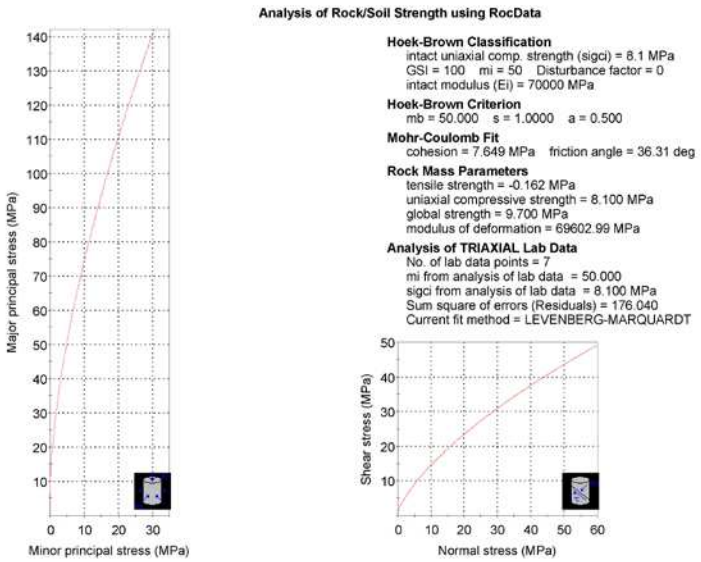

Figure 6. Determining the residual strength envelope of the intact rock specimen using RocData v.4.0

The measured data were summarized for aplite, contaminated monogranite, contaminated monzonite, monzogranite and monzinite in Tables 1–5., respectively. In these tables the minimum, maximum and the average values are presented with their variations, as well. In case of failure state the Hoek–Brown parameters, while in case of residual state the Mohr-Coulomb parameters were determined and used for further calculations. It is important to note that the results were supposed to have normal distribution.

Table 1

Measured values of the aplite

	Failure	**Residual**	
	Hoek-Brown constant (m_i)	**Cohesion (c) [MPa]**	**Internal friction angle (ϕ) [degree]**
Minimum	29.191	2.105	25.560
Maximum	29.122	6.320	51.390
Average	29.259	4.445	42.878
Variance	0.097	1.742	11.743

Table 2

Measured values of the contaminated monzogranite

	Failure	**Residual**	
	Hoek-Brown constant (m_i)	**Cohesion (c) [MPa]**	**Internal friction angle (ϕ) [degree]**
Minimum	10.767	6.066	31.410
Maximum	24.550	9.805	43.690
Average	16.754	7.304	36.350
Variance	6.860	1.692	5.400

Table 3

Measured values of the contaminated monzonite

	Failure	**Residual**	
	Hoek-Brown constant (m_i)	**Cohesion (c) [MPa]**	**Hoek-Brown constant (m_i)**
Minimum	12.947	4.606	33.340
Maximum	29.628	7.649	40.110
Average	19.661	6.645	35.606
Variance	5.540	0.853	2.406

Table 4

Measured values of the monzogranit

	Failure	**Residual**	
	Hoek-Brown constant (m_i)	**Cohesion (c) [MPa]**	**Hoek-Brown constant (m_i)**
Minimum	10.445	2.050	32.760
Maximum	24.854	8.216	47.520
Average	17.237	5.961	38.533
Variance	4.474	2.005	4.103

Table 5

Measured values of the monzonit

	Failure	**Residual**	
	Hoek-Brown constant (m_i)	**Cohesion (c) [MPa]**	**Hoek-Brown constant (m_i)**
Minimum	11.077	5.707	34.060
Maximum	27.724	7.466	37.040
Average	17.992	6.775	35.436
Variance	4.733	0.690	1.177

According to the results the failure envelope of aplit samples differed significantly from the other classes in Bátaapáti. By the other types of rocks from the Mórágy Granite Formation neither the failure envelope nor the residual strength envelope showed significant differences from each other, although these different rock types have different mineral size and mineral contents.

The average value of the m_i according to the all measurements taken was 18.089 (variance: 5.031). The suggested value for granitic rocks is 33±5 in the international practice, which is much more higher than this value. Probably the reason of the big difference is the micro-tectonic influences of the Mórágy Granite. These different tectonical impacts highly influence the mechanical behavior and parameters of the different types of rocks.

The measured parameters are very important for the safe and correct rock engineering design in Bátaapáti. In lack of these laboratory tests only the internationally suggested values could be used which are highly different from the real values. In this case it would result a big mistake at the expense of the safety. Using the MFS triaxial test method the tunnel and chamber designs in Bátaapáti became more optimal and safe.

The above presented results show that by using the MFS triaxial tests the influences of the tectonics, mineral size and contents, weathering degrees etc. can be exactly measured. By applying this method the failure envelope of the sample can be determined exactly, so it is less time and money consuming, whereas more information can be received than from the traditional methods. The Bátaapáti Radioactive Waste Landfill could be optimally designed by using these data.

6. Conclusion

1. The failure envelope of the rock mass is one of the most important mechanical information for designing in or on rock. This mechanical parameter can be calculated from the quality of the rock mass (i.e. value of the rock mass classification) and from the failure envelope of the intact rock.
2. The laboratory results of the failure envelope determination of the intact rock measured by using Multiplied Failure State (MFS) triaxial tests for different granitic rock samples from National Radioactive Waste Landfill (NRWR) at Bátaapáti provide basis for the optimal design of Radioactive Waste Landfill.

7. References

[1] KÁRMÁN, T.: Mitől függ az anyag igénybevétele? (What influences the strength of the material?), *Magyar Mérnök- és Építész-Egylet Közlönye* 10, 1910, 212–226. in Hungarian

[2] DEÁK, F.–VÁN, P.–VÁSÁRHELYI, B.: Hundred years after the first triaxial test. *Periodica Polytechnica – Ser. Civ. Engng.* 56/1 (2012) 115–122.

[3] VÁN, P.–VÁSÁRHELYI, B.: Centenary of the first triaxial test - recalculation of the results of Kármán, Eurock'2010 (Laussane), in: Rock Mechanics in Civil and Environmental Engineering (eds.: Zhao, J.–Labiouse, V.–Dudt, J. P.–Mathier, J. F.). Taylor & Francis, 2010, pp. 59–62.

[4] ISRM: Suggested Method for Determining the Strength of Rock Materials in Triaxial Compression. *Int. J. Rock Mech. Min. Sci. & Geomech. Abstr.* 1978, 15: 47–51.

[5] KOVÁRI, K.–TISA, A.: Multiple failure state and strain controlled triaxial tests. *Rock Mech. Rock Engng*. 1975, **7**(1): 17–33.
[6] KOVÁRI, K.–TISA, A.: Attinger R.O.: The concept of "continuous failure state" triaxial tests. *Rock Mech. Rock Engng*. 1983 16 (2): 117–131.
[7] KOVÁRI, K.–TISA, A.–EINSTEIN, H. H.–FRANKLIN, J. A.: Suggested methods for deter-mining the strength of rock materials in triaxial compression: revised version. *Int. J. Rock Mech. Min. Sci & Geomech. Abstr.* 1983. 20 (6): 283–290.
[8] GÁLOS, M.–VÁSÁRHELYI, B.: Kőzetmechanikai anyagtulajdonságok meghatározása CFS rendszerű triaxiális vizsgálattal (Determining the rock mechanical paramteres using CFS triaxial tests). In: *Geotechnika'97*, Ráckeve, 1997 okt. 28–29. CD-ROM (in Hungarian).
[9] CSUHANICS, B.–DEBRECZENI, Á.: Development of Automatic Control of Multi-stage Triaxial Tests at the University of Miskolc, *Geosciences and Engineering*, Vol. 2 (2013) No**.** 3, pp. 37–43.

Geosciences and Engineering, Vol. 2, No. 4 (2013), pp 102-115.

GENERATING HILBERT-TRANSFORM WITH THE USE OF INVERSION-BASED ROBUST FOURIER-TRANSFORM

HAJNALKA SZEGEDI

Department of Geophysics, University of Miskolc

1. Abstract

In this study a robust inversion method is presented for performing the Hilbert-transform, which shows robust behavior against outliers. The most frequent value method (MFV) was developed by professor Steiner at the Department of Geophysics of Miskolc University. The inversion-based Fourier-transform (IRLS-FT) has shown itself to be a useful tool for robust spectrum calculations. It has been proved in former publications. The prominent noise suppression ability and the resistance against outliers of ourrobust Fourier-transform algorithm give reason for applying it in the field of seismic data processing. Using IRLS-FT the robustified version of the Hilbert-transform is presented, and the absolute value of the analytic signal, which is calculated as a seismic attribute (instantaneous amplitude) is shown. This transform is performed in the framework of the iteratively reweighted least squares method (IRLS) with the use of Steiner weights. For the discretization of the time function series expansion were applied with the scaled Hermite functions as basis functions. The coefficients of the series expansion are handled as unknown inversion parameters. The new Hilbert-transform algorithm was tested on the Ricker wavelet data contaminated by noises following Gaussian or Cauchy distribution. The results show that the method appreciably reduces the noise sensitivity of the inversion procedure even in case of having outlier data.

2. Introduction

The attribute section plays an important role in seismic data processing and interpretation. By the help of them some kind of important information (regarding the physical or geometric parameters) can be emphasized. Since TANER et al. (1979) have published groundbreaking announcement the subject area has been expanded and have evolved substantially. Nowadays, we can talk about a wide collection of the attributes and candivide them into physical and geometrical attributes. The procedures can be classified according to whetherthey are used before or after stacking and one or more seismic tracks are interpreted etc. During the development and applying of the measurement and data processing methodsit is always very important task to handle the signal-to-noise ratio.The Fourier-transform playsa basic role in generating the attribute sections.In former paper [5] a robust, inversion based Fourier-transform algorithm (IRLS-FT) was proposed.It was shown that the method works effectively in suppression of outliers and it is able to improve the signal-to-noise ratio by an order of magnitude.In this paper we apply the method in the field of calculating the attribute sections. At first the Hilbert-transform will be demonstrated in the framework of the robust/resistant inversion which plays a key role in the definition of the analytic seismic channel.

3. Analytic signal

In calculation of the basic attribute sections the baseline is generating the analytic signal (analytic or complex channel). Its definition was introduced by DÉNES GÁBOR (Hungarian Nobel prize physicist) into data processing [1]. His aspiration was to apply the effective

mathematical tools of quantum mechanics (Hilbert space, square integrable complex functions etc.) in the field of signal processing. Therefore the (real) time domain signal

$$u(t) = a\cos(\omega t) + b\sin(\omega t) \tag{1}$$

was expanded to a complex one

$$s(t) = u(t) + j\,v(t), \tag{2}$$

where t denotes the time, ω is the angular frequency and j is the imaginary unit. The time function $v(t)$ was defined as

$$v(t) = a\sin(\omega t) - b\cos(\omega t), \tag{3}$$

where based on Eq.(1) changed the sin function to -cos and cos function to sin, thus obtained the quadrature of the function. Equation (2) is rewritten in the following form

$$s(t) = (a - jb)\ \exp(j\omega t), \tag{4}$$

which can be illustrated as a complex rotating vector. This exchange of sin and cos functions was generalized by Gábor and the transformation

$$v(t) = \frac{1}{\pi}\int_{-\infty}^{\infty} u(\tau)\frac{d\tau}{\tau - t}, \tag{5}$$

was introduced, which is the Hilbert transform of the time function *u(t)*

$$v(t) = u_H(t). \tag{6}$$

After Gábor's pioneering work, in data processing the analytic signal was defined as

$$s(t) = u(t) + ju_H(t) \tag{7}$$

In Figure 1 the role of complex analytic signal is shown.

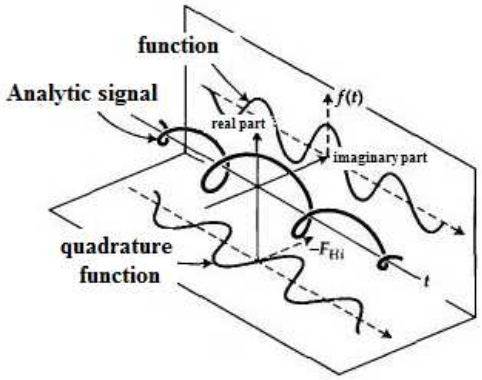

Figure 1
The role of complex analytic signal

According to Eq. (5) the Hilbert-transform is generated as a convolution of the time signal $u(t)$withfunction $-\frac{1}{\pi t}$. It is well-known, that in the frequency domain this connection can be written as

$$\mathcal{F}\{u_H(t)\} = \mathcal{F}\{u(t)\}\mathcal{F}\left\{-\frac{1}{\pi t}\right\}, \tag{8}$$

where $\mathcal{F}$ is the Fourier-transform.As $\mathcal{F}\left\{-\frac{1}{\pi t}\right\} = -j\,\mathrm{sgn}(\omega)$, introducing the notation $U(\omega) = \mathcal{F}\{u(t)\}$ one can write

$$\mathcal{F}\{u_H(t)\} = -j\,\mathrm{sgn}(\omega)U(\omega) = U_H(\omega). \tag{9}$$

It is clear that the spectra of the Hilbert-signal $U_H(\omega)$with this modification is Hermitic resulting that the $u_H(t)$Hilbert-transform is a real time function.

4. **Noise sensitivity of the instantaneous amplitude**

After Eq. (7) the analytic signal is known and the seismic attributes can be generated. Hereinafter as an example the instantaneous amplitude (envelope or reflection strength) is examined, which is defined as

$$A(t) = \sqrt{u(t)^2 + v(t)^2} \tag{10}$$

absolute value of the complex seismic channel. Noise sensitivity of this attribute is shown in Figure 2, which represents a data set of a Ricker wavelet (localized at 0.1 sec with the main frequency of 10 Hz). The signal was sampled in the [–1,1] interval with the 0.005 sec sampling rate. This data set was contaminated by Gaussian noise with zero center and standard deviation $\sigma = 0.0025$ (data set I.). Data set II. (outliers) is produced by using Cauchy distributed noise with $\varepsilon = 0.04$ scale parameter. The Figures 3a–c show the instantaneous amplitude calculated by the use of the traditional DFT in the determination of Hilbert transform (cases of the noiseless, Gaussian and Cauchy distributed noise are presented). It can be seen that the instantaneous amplitude based on data set II (outliers) is particularly noisy. In order to characterize the noise sensitivity of the first seismic attribute the distance defined in data space

$$d = \sqrt{\frac{1}{N}\sum_{k=1}^{N}\left(A^{(noisy)}(t_k) - A^{(noiseless)}(t_k)\right)^2} \tag{11}$$

has been introduced. It isin case of data set I. $d_{(I.)} = 0.0306$ and in case of data set II $d_{(II.)} = 0.0444$.

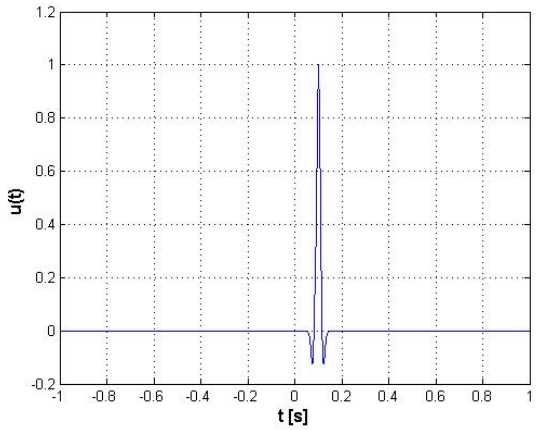

Figure 2

The noiseless Ricker wavelet in the time domain

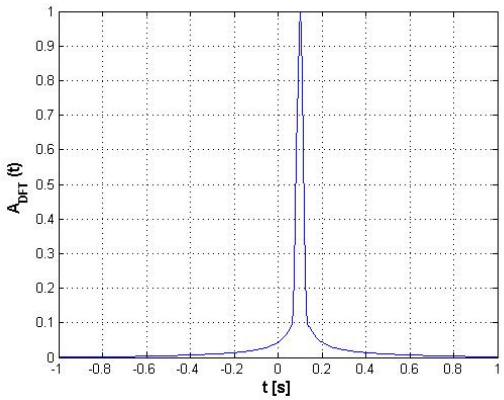

Figure 3a

The noiseless reflection strength in the time domain (traditional method)

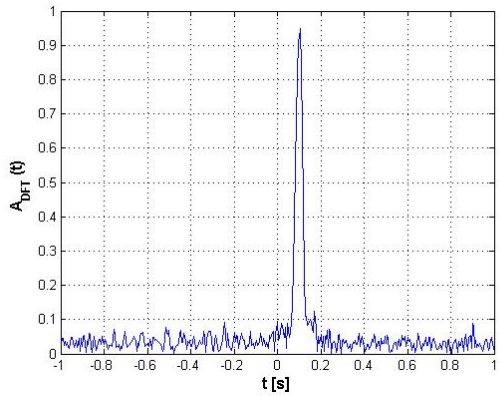

Figure 3b

The reflection strength in case of data set I (traditional method)

Looking at Figure 3c it seems quite reasonable to create a more robust Hilbert-transform method with reduced sensitivity against outliers. In the following we define the Hilbert-transform with the use of our IRLS-FT robust Fourier-transform method.

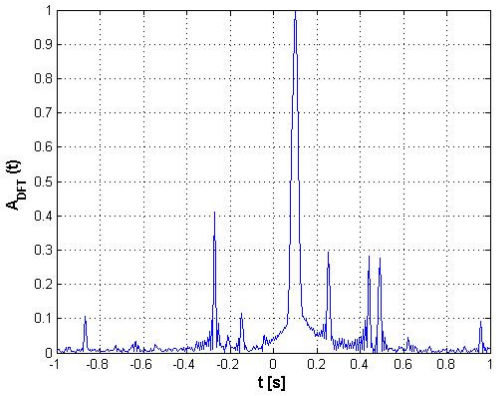

Figure 3c

The reflection strength in case of data set II (traditional method)

5. Theoretical background: the inversion-based Fourier-transform

For the one-dimensional case a continuous Fourier-transform is defined as

$$U(\omega)=\frac{1}{\sqrt{2\pi}}\int_{-\infty}^{\infty}u(t)e^{-j\omega t}dt. \tag{12}$$

The frequency spectrum $U(\omega)$ is the Fourier transform of a real valued time function *u(t)* and it is generally a complex valued continuous function. By means of the inverse Fourier-transform

$$\mathrm{u(t)}=\frac{1}{\sqrt{2\pi}}\int_{-\infty}^{\infty}\mathrm{U(\omega)e^{j\omega t}d\omega} \tag{13}$$

we can return back from the frequency domain to the time domain. In defining the Fourier-transform as an inverse problem, the frequency spectrum $\mathrm{U(\omega)}$ should be described by a discrete parametric model. In order to satisfy this expectation, let us assume that $\mathrm{U(\omega)}$ is approximated with sufficient accuracy by using a finite series expansion

$$\mathrm{U(\omega)}=\sum_{n=1}^{M}\mathrm{B_n\Psi_n(\omega)}, \tag{14}$$

where the parameter $\mathrm{B_n}$ is a complex valued expansion coefficient and Ψ_n is a member of an accordingly chosen set of real valued basis functions.Using the terminology of (discrete) inverse problem theory, the theoretical values of time domain data can be given by the inverse Fourier-transform

$$\mathrm{u^{theor}(t_k)=u_k^{theor}}=\frac{1}{\sqrt{2\pi}}\int_{-\infty}^{\infty}\mathrm{U(\omega)e^{j\omega t_k}d\omega}, \tag{15}$$

where t_k is the k-th sampling time. Inserting the expression given in Eq. (14) one finds that

$$u_k^{theor}\cong\int_{-\infty}^{\infty}\left(\sum_{n=1}^{M}B_n\Psi_n(\omega)\right)e^{j\omega t_k}d\omega=\sum_{n=1}^{M}B_n\int_{-\infty}^{\infty}\Psi_n(\omega)e^{j\omega t_k}d\omega. \tag{16}$$

Let us introduce the notation

$$\mathrm{G_{kn}}=\int_{-\infty}^{\infty}\mathrm{\Psi_n(\omega)e^{j\omega t_k}d\omega}, \tag{17}$$

where G_{kn} is an element of the$N\times M$ sized Jacobi's matrix (*N* is the number of time domain data and *M* is the number of unknown expansion coefficients). It can be noted, that the Jacobi'smatrix is the inverse Fourier-transform (in $t=t_k$) of the Ψ_n basis function.

After this step, the theoretical values can be written in a linear form

$$\mathrm{u_k^{theor}}=\sum_{n=1}^{M}\mathrm{B_n\,G_{kn}}. \tag{18}$$

The parametrization of a model is always an important step in constructing an inversion algorithm. As a frequency spectrum is defined over the interval $(-\infty,\infty)$ the choice of a set of basis functions defined over the same interval would be advantageous. In addition, the use of a set of orthonormal functions for the series expansion is generally prosperous to the parametrization of the model. In order to fulfil these requirements, we have chosen the set of scaled Hermite-functions, especially because they are square-integrable (which ensures the existence of their Fourier-transform).

Following the algebraic rulespresented in our previous work [5] let us consider the basic formula of the scaled Hermite-polynomials and Hermite-functions. The Rodriguez-formula for scaled Hermite-polynomials takes the form

$$h_n(\omega,\alpha) = (-1)^n e^{\alpha\omega^2}\left(\frac{d}{d\omega}\right)^n e^{-\alpha\omega^2} \tag{19}$$

and can be generated by therecursion formula

$$h_{n+1}(\omega,\alpha) = 2\omega\alpha\, h_n(\omega,\alpha) - 2n\alpha\, h_{n-1}(\omega,\alpha), \tag{20}$$

whereα is the scale factor and $h_0(\omega,\alpha)=1$, $h_1(\omega,\alpha)=2\alpha\omega$ [4]. The normalizing equation is

$$\int_{-\infty}^{\infty} e^{-\frac{\alpha\omega^2}{2}} h_n(\omega,\alpha)\, h_m(\omega,\alpha)\, d\omega = \sqrt{\frac{\pi}{\alpha}}(2\alpha)^n n!\delta_{nm},\ \delta_{nm} = \begin{cases} 0, n \neq m \\ 1, n = m \end{cases} \tag{21}$$

and the scaled Hermite-functions can be defined as

$$H_n(\omega,\alpha) = \frac{e^{-\frac{\alpha\omega^2}{2}} h_n(\omega,\alpha)}{\sqrt{\sqrt{\frac{\pi}{\alpha}}\, n!(2\alpha)^n}}. \tag{22}$$

The normalizing equation in case of the modified Hermite-function is

$$\int_{-\infty}^{\infty} H_n(\omega,\alpha)\, H_m(\omega,\alpha) d\omega = \delta_{nm},\ \delta_{nm} = \begin{cases} 0, n \neq m \\ 1, n = m \end{cases} \tag{23}$$

Expanding the spectrum by means of the modified Hermite functions, in accordance with Eq. (17) the elements of the Jacobi's matrix represent the inverse Fourier transforms of the $H_n(\omega,\alpha)$ basisfunctions

$$G_{kn} = \frac{1}{\sqrt{2\pi}} \int_{-\infty}^{\infty} H_n(\omega,\alpha)\, e^{j\omega t}\, d\omega. \tag{24}$$

It was proved earlier in [5] that

$$G_{kn} = \frac{1}{\sqrt[4]{\alpha}} (j)^n H_n^{(0)}(t') = \frac{1}{\sqrt[4]{\alpha}} (j)^n H_n^{(0)}\left(\frac{t}{\sqrt{\alpha}}\right). \tag{25}$$

This is a very important result in further developing the inversion-based Fourier transform method because the Jacobi's matrix can be produced quickly, as the procedure do not require any integration.

In accordance with Eq. (18) the theoretical data can be calculated as a linear expression of the expansion coefficients using the easily calculated elements of the Jacobi's matrix. The general element of the deviation vector can be given in the following form

$$e_k = u_k^{\text{measured}} - u_k^{\text{theor}}. \tag{26}$$

If the measured data set contains Gaussian noise, the minimization of the L_2 norm of the deviation vector is applied. This is the case of the Least Squares method (LSQ) when

$$E_2 = \sum_{k=1}^{N} e_k^2 \tag{27}$$

is minimized resulting in the well-known set of normal equations

$$G^T G \vec{B} = G^T \vec{u}^{\,\text{measured}}. \tag{28}$$

By solving these normal equations we can give an estimate for the complex expansion coefficients, and both the real and imaginary parts of the LSQ estimatedFourier transform (LSQ-FT) can be calculated at any frequency by using

$$U^{\text{estimated}}(\omega) = \sum_{n=1}^{M} B_n^{\text{estimated}} \Psi_n(\omega). \tag{29}$$

It is well-known that the least squares method (LSQ) gives optimal results only in the case when the noise contaminating the data follows Gaussian distribution. In more general cases other norms of the deviation vector can be used. In order to define a robust inversion algorithm, the minimization of the weighted norm

$$E_w = \sum_{k=1}^{N} w_k e_k^2 \tag{30}$$

with the so-called Cauchy-weights

$$w_k = \frac{\sigma^2}{\sigma^2 + e_k^2} \tag{31}$$

is suggested (here σ^2 is an accordingly chosen positive number). Using this norm for the solution of inverse problems provides reliable results even if the input data sets contain outliers [5].

There is a problem with inversion procedures involving Cauchy weights: the scale parameter should be apriori given. This difficulty can easily be solved by using the Steiner-weights [3]. In the framework of Steiner's method (previously called the method of Most Frequent Values or abbreviated as MFV) the scale parameter σ^2 can be determined in an internal iteration loop. In the *(j+1)*-th step of this procedure the ε_{j+1}^2 (Steiner's scale factor called dihesion) can be calculated in the knowledge of ε_j^2 as

$$\varepsilon_{j+1}^2 = 3\frac{\sum_{k=1}^{N}\frac{e_k^2}{\left(\varepsilon_j^2+e_k^2\right)^2}}{\sum_{k=1}^{N}\left(\frac{1}{\varepsilon_j^2+e_k^2}\right)^2}, \tag{32}$$

where in the *0*-th step the ε_0 starting value is given as

$$\varepsilon_0 \le \frac{\sqrt{3}}{2}\left(e_{max}-e_{min}\right). \tag{33}$$

It can be seen that the above procedure derives the scale parameter from the data set (deviation between measured and calculated data). The stop criterion can easily be defined by experience (for example, a fixed number of iterations). After this, the Steiner-weights are calculated by using the (Steiner's) scale parameter given in the last step of the internal iterations having the form

$$w_k = \frac{\varepsilon^2}{\varepsilon^2+e_k^2} \tag{34}$$

In the case of Steiner-weights the misfit function given in Eq. (30) is non-quadratic (because e_k contains the unknown expansion coefficients), thus the inverse problem is nonlinear which can be solved again by applying the method of the Iteratively Reweighted Least Squares[8]. In the framework of this algorithm a *0*-th order solution $\vec{B}^{(0)}$ is derived by using the (non-weighted) LSQ method and the weights are calculated as

$$w_k^{(0)} = \frac{\varepsilon^2}{\varepsilon^2+(e_k^{(0)})^2} \tag{35}$$

with

$$e_k^{(0)} = u_k^{measured} - u_k^{(0)}, \tag{36}$$

where

$$u_k^{(0)} = \sum_{n=1}^{M} B_n^{(0)} G_{kn}. \tag{37}$$

In the first iteration the misfit function

$$E_w^{(1)} = \sum_{k=1}^{N} w_k^{(0)} (e_k^{(1)})^2 \tag{38}$$

is minimized resulting in the linear set of normal equations

$$G^T W^{(0)} G \vec{B}^{(1)} = G^T W^{(0)} \vec{u}^{measured} \tag{39}$$

of the weighted Least Squares method where the $W^{(0)}$ weighting matrix is diagonal

$$W_{kk}^{(0)} = w_k^{(0)} . \tag{40}$$

This procedure in the typical *j*-th iteration step is

$$G^T W^{(j-1)} G \vec{B}^{(j)} = G^T W^{(j-1)} \vec{u}^{\,measured} \tag{41}$$

with the $W^{(j-1)}$ weighting matrix

$$W_{kk}^{(j-1)} = w_k^{(j-1)} . \tag{42}$$

(In these steps the normal equation is linear, because the weights are always calculated in a previous step. Here we note that each step of these iterations contain an internal loop for the determination of the Steiner's scale parameter.) This iteration is repeated until a proper stop criterion is met. Using the expansion coefficients given by this procedure the required function of the spectrum can be calculated by means of Eq. (14) at any frequency.

6. **The robust Hilbert transformation**

According to Eq. (3) the Hilbert-transform is generated as a convolution of the time signal *u(t)*with function $-\frac{1}{\pi t}$ in frequency domain

$$\mathcal{F}\{u_H(t)\} = \mathcal{F}_{IRLS}\{u(t)\}\mathcal{F}\left\{-\frac{1}{\pi t}\right\}, \tag{43}$$

where $\mathcal{F}_{IRLS}$ denotes ourrobust Fourier-transform procedure summarized above. As $\mathcal{F}\left\{-\frac{1}{\pi t}\right\} = -j\,\mathrm{sgn}(\omega)$, introducing the notation $U(\omega) = \mathcal{F}_{IRLS}\{u(t)\}$ one can write

$$\mathcal{F}\{u_H(t)\} = -j\,sgn(\omega)U(\omega) = U_H(\omega). \tag{44}$$

From this point we have two possibilities. On one hand, we can define the inverse Fourier-transformation similarly to the above IRLS-FT and define the algorithm of IRLS-IFT,on the other hand we can simply apply the traditional Inverse Discrete Fourier Transform (IDFT) in order to go back to the time domain. Both ways result in a robust Hilbert-transform. In what follows, choosing the second way we use IDFT for calculating $u_H(t)$ and show some numerical examples.

7. **Numerical results**

In Figures 3a–c the instantaneous amplitude calculated on the traditional way was presented in case of noiseless, and noise data set (following Gauss- and Cauchy-distribution). In Figures. 4a–c we show the instantaneous amplitude calculatedby means our robust Hilbert-transform method. Of course, our method provides the same result for noiseless signal. In case of data set I (Gaussian-noise) the robust inversion based Hilbert-transform (see Figure 4b) seems to be less noisy (compared the traditional result in Figure 3b). The moderate improvement is characterized by the distance in data space ($d_{(L)}$ = 0.0183).However,

substantial further improvement reflects the robust inversion method with the use of Steiner-weights in case of data set II (Cauchy-noise).

According to Fig. 4c.,one can see an almost complete suppression of the effect of outliers, which is justified alsoby the data distance ($d_{(II.)}$ = 0.0064). Compared to the traditional Hilbert-transform, our results reflects an improvement ofthe data distance byan order of magnitude.

These results certify abetterthe signal-to-noise ratio if the Hilbert-transform is calculated by an inversion based robust FT method.

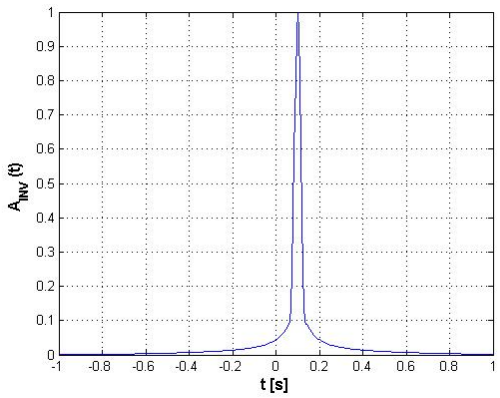

Figure 4a

The noiseless reflection strength in the time domain (new inversion method)

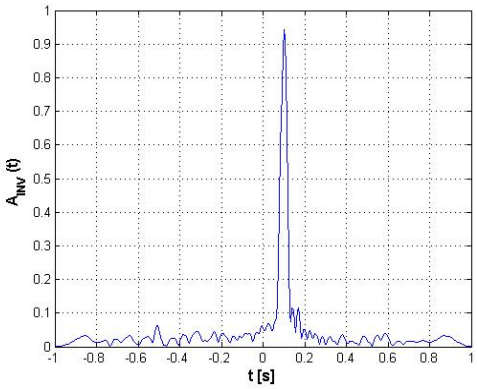

Figure 4b

The reflection strength in the time domain in case of data set I. (new inversion method)

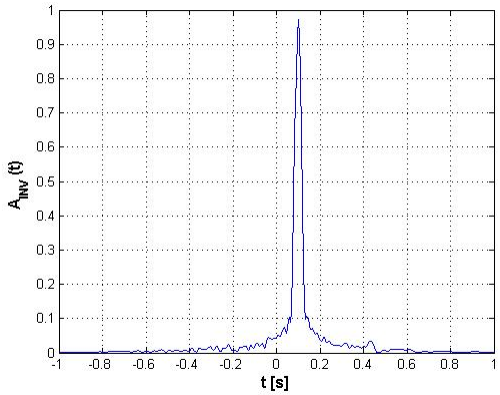

Figure 4c

The reflection strength in the time domain in case of data set II (new inversion method)

8. Conclusions

In a previous paper [5] based on the Most Frequent method (MFV) by Ferenc Steiner a new inversionbased FT algorithm was proposed. Our IRLS-FT method has sufficient noise rejection capability and considerable resistance against outliers. In this study this algorithm was applied for generating the Hilbert-transform. The new algorithm is based on double-inversion procedure: firstly the Fourier-spectra of the time function (showing a seismic trace) are defined by IRLS inversion, and secondly we can transform the obtained spectra by robust inversion in the time domain.

Although the double inversion compared to the conventional DFT/IDFT transformation requires significant computational time surplus, according to the demonstrated figures large improvement in signal-to noise ratio can be achieved by using the new inversion based Hilbert-transform method. Taking into account the capacity and speed of contemporary computers the extra computational time is probably tolerable in many practical cases.

9. Acknowledgments

This research was supported by the European Union and the State of Hungary, co-financed by the European Social Fund in the framework of TÁMOP 4.2.4. A/2-11-1-2012-0001 "National Excellence Program".

10. List of Symbols

A(t)	absolute amplitude of the complex channel
B_n	unknowncomplex expansion coefficients
Ψ_n	n-th knownbasis function
E_2	objective function
E_w	weighted norm
G	Jacobi's matrix

G_{kn}	one element of Jacobi's matrix
G^T	transposed matrix of the Jacobi's matrix
$(G^TG)^{-1}$	inverse of matrix G^TG
$H_n(\omega,\alpha)$	scaled Hermite-function
$h_n(\omega,\alpha)$	scaledHermite-polynomial
M	number of unknown series expansion coefficients
N	number of measured data
$U(\omega)$	complex frequency spectrum
$U_H(\omega)$	complex Hilbert-spectrum
W	weighting matrix
$W^{(j-1)}$	weighting matrix used in the j-th iteration step
a, b	variables
d	data distance in time domain
j	imaginary unit
t	time
t_k	k-th sampled time
u(t), v(t)	time dependent functions
s(t)	complex signal
$u_H(t)$	Hilbert-transform in time domain
u_k^{theor}	calculated data
$u_k^{measured}$	measured data
e_k	k-th element of the deviation vector
w_k	k-th diagonal element of weighting matrix
$\mathcal{F}$	operator of Fourier transform
ε_{j+1}^2	Steiner's scale factor called dihesion
α	scaling factor
δ_{nm}	Kronecker-delta symbol
τ	integration parameter
ε	scale parameter
ω	angular frequency
σ	standard deviation

11. References

[1] GÁBOR, D.: Theory of communication. Part I. *J. Inst. Elect. Eng*., 93, 1946, 429–441.

[2] STEINER, F.: *Optimum methods in statistics*. Akadémiai Kiadó, Budapest, 1997.

[3] STEINER, F.: Most frequent value procedures. (A short monograph.) *Geophysical Transactions*, 34, 1988, 139–260.

[4] GRÖBNER, I. W.–HOFFREITER, N.: *Integraltafel*. Zweiter Teil. Bestimmte Integrale. Springer-Verlag, Wien und Innsbruck. 1958.

[5] DOBRÓKA, M.–SZEGEDI, H.: Robusztus Fourier-transzformáció Steiner-súlyok alkalma-zásával. *Magyar Geofizika*, 53 (1), 2012, 1–8.

[6] TANER, M. T.–KOEHLER, F.–SHERIFF, R. E.: Complex seismic trace analysis. *Geophysics*, 44 (6), 1979, 1041–1063.

[7] VAIDYANATHAN, V. V.**:** Eigenfunctions of the Fourier Transform. *IETE Journal of Education*, 49 (2), 2008, 51–58.

[8] SCALES, J. A.–GERSZTENKORN, A.–TREITEL, S.: Fast Lp solution of large, sparse, linear systems: Application to seismic travel time tomography. *Journal of Comp. Phys*. 75, 1988, 314–333.